(2)

PENNSTATE

DEPARTMENT OF METEOROLOGY

Final Technical Report

The Measurement of Air-Sea Fluxes

Contract Number: N00014-85-K-0250/P00003

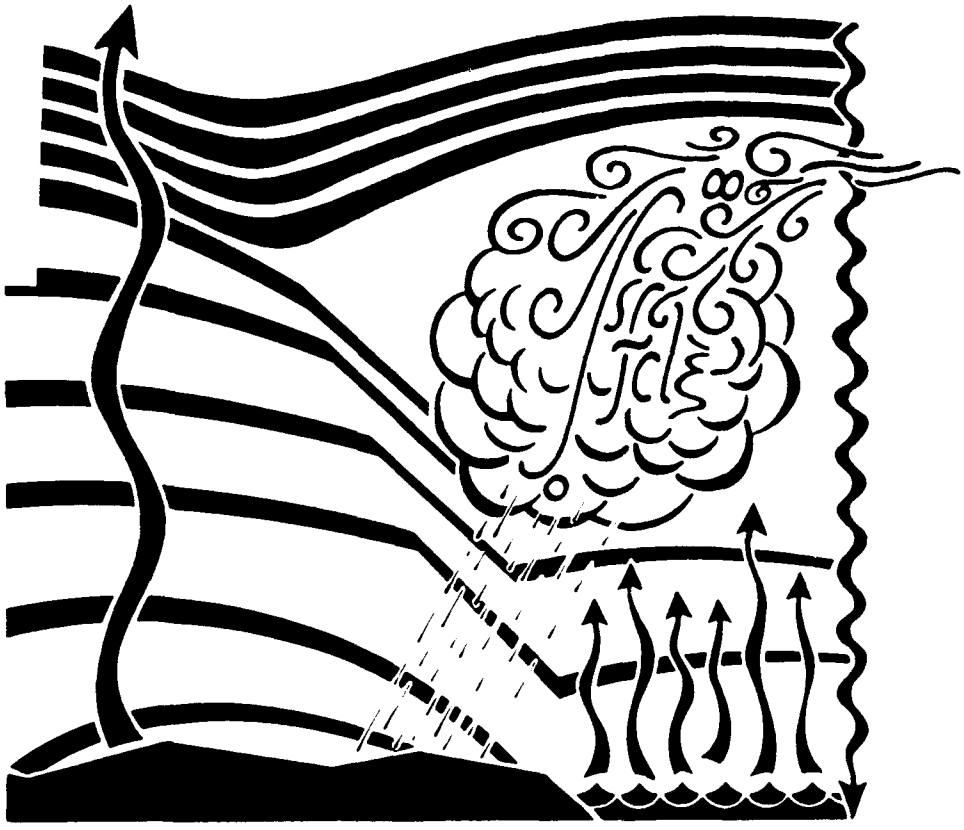

C.W. Fairall
Code R/E/WP7
NOAA/ERL/WPL
325 Broadway
Boulder, CO 80307

George S. Young
Dept. of Meteo.
503 Walker Bldg.
University Park PA
16802

Submitted to: Office of Naval Research
Ocean Sciences, Code 1122 MM
800 N. Quincy Street
Arlington, VA 22217

10 October 1990

90

FINAL TECHNICAL REPORT

The Measurement of Air-Sea Fluxes

ONR Contract N00014-85-K-0250

For the Period from 1 January 1985 to 31 March 1990

C.W. Fairall*, Associate Professor

G. Young, Assistant Professor

Department of Meteorology

The Pennsylvania State University

University Park, PA 16802

* Present address: Code R/E/WP7, NOAA/ERL/WPL, 325 Broadway, Boulder, CO, 80307-3000

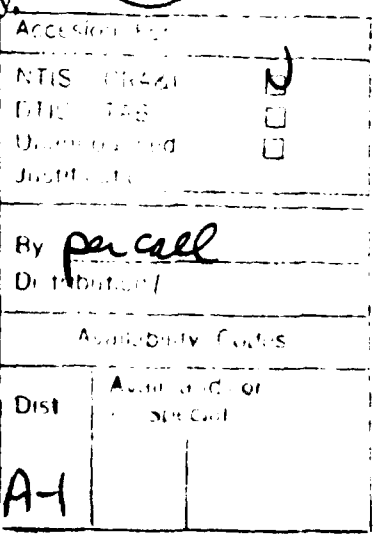

9 October 1990

TABLE OF CONTENTS

PUBLICATIONS

REFEREED JOURNALS

1. Fairall, C.W. and S.E. Larsen, 1985: Inertial-dissipation methods and turbulent fluxes at the air-ocean interface. *Boundary-Layer Meteorology*, **34**, 287-301.

2. Larsen, S.E., J. Hojstrup, and C.W. Fairall, 1985: Mixed and dynamic response of hot wires and cold wires and measurements of turbulence statistics. *J. Atmos. and Oceanic Tech.*, **3**, 236-246.

3. Fairall, C.W., 1987: A top-down and bottom-up diffusion model of CT_2 and CO^2 in the entraining convective boundary layer. *J. Atmos. Sci.*, **44**, 1009-1017.

4. Larsen, S.E., C.W. Fairall, P.G. Mestayer, and J.B. Edson, 1989: Velocity contamination of temperature variance spectra from sonic anemometers. *J. Atmos. and Oceanic Tech.*, submitted.

5. Fairall, C.W., J.B. Edson, S.E. Larsen, and P.G. Mestayer, 1989: Inertial-dissipation air-sea flux measurements: a prototype system using realtime spectral computations. *J. Atmos. and Oceanic Tech.*, to appear.

6. Edson, J.B., C.W. Fairall, S.E. Larsen, and P.G. Mestayer, 1989: A study of the inertial-dissipation method of obtaining air-sea fluxes. *J. Geophys. Res.*, submitted.

7. Mestayer, P.G., S.E. Larsen, C.W. Fairall, and J.B. Edson, 1989: Turbulence sensor dynamic calibration using realtime spectral computations. *J. Ocean. Atmos. Technology*, submitted.

CONFERENCE PROCEEDINGS

1. Fairall, C.W., S.E. Larsen, P.G. Mestayer, and D.E. Spiel, 1986: Measurements of spray droplet transport and evaporation during HEXIST. *Proc. 6th Conference on Ocean-Atm. Interaction*, AMS, Boston, MA.

2. Mestayer, P.G., C.W. Fairall, and S.E. Larsen, 1987: Turbulent Transport and evaporation of droplets generated at an air-water interface. *Turbulent Shear Flows*, **6**, J.C. Andre, J. Cousteix, F. Durst, B.E. Launder, F.W. Schmidt and J.B. Whitelaw, Editors, Springer-Verlag, pp. 129-147.

3. Fairall, C.W., J.B. Edson, S.E. Larsen, and P.G. Mestayer, 1988: A comparison of inertial-dissipation and eddy covariance surface flux measurements during the HEXMAX experiment. *Proc. 7th Conference on Ocean-Atm. Interaction*, AMS, Boston, MA.

4. Edson, J.B., C.W. Fairall, S.E. Larsen, and P.G. Mestayer, 1988: A random walk simulation of the turbulent transport of evaporating jet drops in the air-sea simulation tunnel during HEXIST. *Proc. 7th Conference on Ocean-Atm. Interaction*, AMS, Boston, MA.

5. Miller, M.A. and C.W. Fairall, 1988: A new parameterization of spray droplet production by oceanic whitecaps. *Proc. 7th Conference on Ocean-Atm. Interaction*, Boston, MA.

6. Larsen, S.E., C.W. Fairall, J.B. Edson, and P.G. Mestayer, 1988: Sonic temperature measurements during HEXMAX. *Proc. NATO Advanced Workshop on Humidity Exchange Over the Sea Main Experiment (HEXMAX)*, Dellenhove, Epe, The Netherlands, pp 58-69.

7. Edson, J.B., C.W. Fairall, S.E. Larsen, and P.G. Mestayer, 1988: Progress report from the inertial-dissipation group. *Proc. NATO Advanced Workshop on Humidity Exchange Over the Sea Main Experiment (HEXMAX)*, Dellenhove, Epe, The Netherlands, pp 44-57.

8. Mestayer, P.G., and 13 additional authors, 1988: HEXIST. *Proc. NATO Advanced Workshop on Humidity Exchange Over the Sea Main Experiment (HEXMAX)*, Dellenhove, Epe, The Netherlands, pp 154-163.

9. Edson, J.B., C.W. Fairall, S.E. Larsen, and P.G. Mestayer, 1988: The HEXIST Lagrangian simulation of the transport of evaporating jet drops. *Proc. NATO Advanced Workshop on Humidity Exchange Over the Sea Main Experiment (HEXMAX)*, Dellenhove, Epe, The Netherlands, pp 164-177.

CHAPTERS IN BOOKS

1. Fairall, C.W., 1987: Similarity theories and microturbulence in the atmospheric mixed layer. In *Dynamics of the Oceanic Surface Mixed Layer*, P. Muller and D. Henderson, Ed., HIG Special Publication, Honolulu, HI.

2. Fairall, C.W., J.B. Edson and M.A. Miller, 1989: Heat fluxes, whitecaps, and seaspray, Chapter 10 in *Surface Waves and Fluxes: Current Theory and Remote Sensing*, G. Geernaert and W. Plant, Ed., Reidel, Holland.

3. Fairall, C.W. and J.B. Edson, 1990: Modeling the droplet contribution to the sea-to-air moisture flux. In *Proc. Symposium on Climate and Health Implications of Bubble-medicated Sea-air Exchange*, U. Connecticut, E. Monahan, Ed., Reidel, Holland.

GRADUATE THESES

Miller, M.A., 1987: An investigation of aerosol generation in the marine planetary boundary layer. MS Thesis, Pennsylvania State University, pp 143.

Edson, J.B., 1989: Lagrangian simulation of the turbulent transport and evaporation of jet droplets. Ph.D. Thesis, Pennsylvania State University, pp 142.

TECHNICAL REPORTS

Fairall, C.W., J.B. Edson, M. Miller: Heat fluxes, whitecaps, and seaspray. Technical Report to the Office of Naval Research, Arlington, VA, 1989.

Fairall, C.W., J.B. Edson, S.E. Larsen and P.G. Mestayer: Intertial-dissipation air-sea flux measurements I: evaluation of a prototype system. Technical Report to the Office of Naval Research, Arlington, VA, 1989

BACKGROUND

This project involves the investigation of an indirect method of inferring surface fluxes of momentum, sensible heat and latent heat over the ocean. The work includes participation in the Humidity Exchange Over the Sea (HEXOS) program, a multinational project involving a series of field measurements and theoretical development. The PI is working closely with two independently funded European scientists: Dr. S.E. Larsen of RISO National Laboratory (Denmark) and Dr. P.G. Mestayer of IMST and LMTTD (France). Dr. Jim Edson just completed his Ph.D. at Penn State after working on this project for four years. He is now on an NSF Postdoctoral Fellowship with P. Mestayer at LMTTD, where he is continuing this study.

The air-sea fluxes are important physical processes which must be parameterized in climate, synoptic, mesoscale, and boundary layer and oceanic numerical models. Because of the increasing contribution of sea spray and whitecap-produced water droplets, it has been suggested that the humidity and heat exchange is strongly nonlinear in wind speed. Thus, it is believed that high wind speed conditions, though brief in duration, may contribute a disproportionate amount to the air-sea budgets. This has a profound influence on local boundary layer structure and intensification of storms by baroclinic instability. It is important to realize that we have almost no hard data on air-sea fluxes over the open ocean (perhaps 20 numerical modelers for each real data point) and that estimates of the fluxes based on mean meteorological data and drag coefficients are totally unverified for winds

greater than 12 m/s. We also have some very preliminary evidence that fluxes derived from the drag coefficient method can be in error by more than a factor of two under changing sea-state and wind conditions.

SCIENTIFIC ACCOMPLISHMENT # 1

IMPROVEMENTS IN AIR-SEA FLUX MEASUREMENTS

The surface fluxes are as difficult to measure as they are important. The instrumentation, technology and data processing techniques required for direct (so-called 'eddy covariance') flux measurements overland are sufficiently complex that it is a job for specialists operating in a hands on, research mode. Over the ocean, the measurements problems are much worse. For example, direct measurements have never been made from ships because of flow distortion and ship motions. The effects of ship motion can only be removed by employing an inertial navigation system that costs at least as much as the basic flux sensors. The effects of flow distortion have not been examined, except theoretically. As a result, very few measurements have ever been made over the open ocean (the majority of published data have been obtained in coastal areas or from research aircraft). However, the fluxes, which are relatively low frequency (e.g., 0.1 Hz) cross correlation phenomena, are closely coupled to the high frequency (e.g., 50 Hz) microturbulence. The use of high frequency turbulence data to infer the air-sea fluxes is called the inertial-dissipation method. In this project we are studying the relationship of the fluxes to the microturbulence and the factors that influence the application of both methods in the marine environment.

In November, 1986 we participated in the HEXMAX experiment in the North Sea off the Coast of Holland where we obtained simultaneous measurements of surface fluxes using both flux methods. The experiment was conducted on the Dutch research platform MPN

about 15 miles off the coast. Two complete suites of instruments were used, one set mounted on a boom extended 18 m horizontally away from the platform at a height of 7 m over the ocean surface. A second set was mounted on a mast 8 m above the helicopter deck at a height of 25 m over the ocean surface. The boom sensors were in a location relatively undisturbed by the platform while the mast sensors were in a location with considerable flow distortion (chosen to simulate the flow distortion typical for sensors placed on ships).

Examination of the HEXMAX data, various theoretical developments, and subsequent investigation of instruments has allowed us to define several steps in the improvement of air-sea flux measurements. The sonic anemometer and infrared hygrometer (commercially available) are the best choice for oceanic work. Many months of measurements were performed to demonstrate the utility and accuracy of this combination for flux measurements over land. A complicated theoretical analysis was done that allows us to use sonic temperature in the inertial-dissipation determination of sensible heat flux. The Wyngaard theory of flow distortion effects by cylindrical objects was simplified and cast in terms of measured variables. A simple equation was developed that expresses the correction to the measured surface stress in terms of the measured tilt angle of the flow at the anemometer. This represented a 20% correction to the stress measurements on the boom from the HEXMAX experiment. Finally, a 'dynamic calibration' method was developed that permits fast response sensors to be used for much more accurate flux measurements by coupling their calibration to slower, but more reliable, standard sensors. This eliminates the need for tedious laboratory calibrations of these sensors and mitigates the drift deterioration

of that calibration. Examples of sensible and latent heat flux measurements are given in Fig. 1. All of these improvements will contribute to substantially more accurate ship-based measurements in the future. More details of this work are provided in Appendix A.

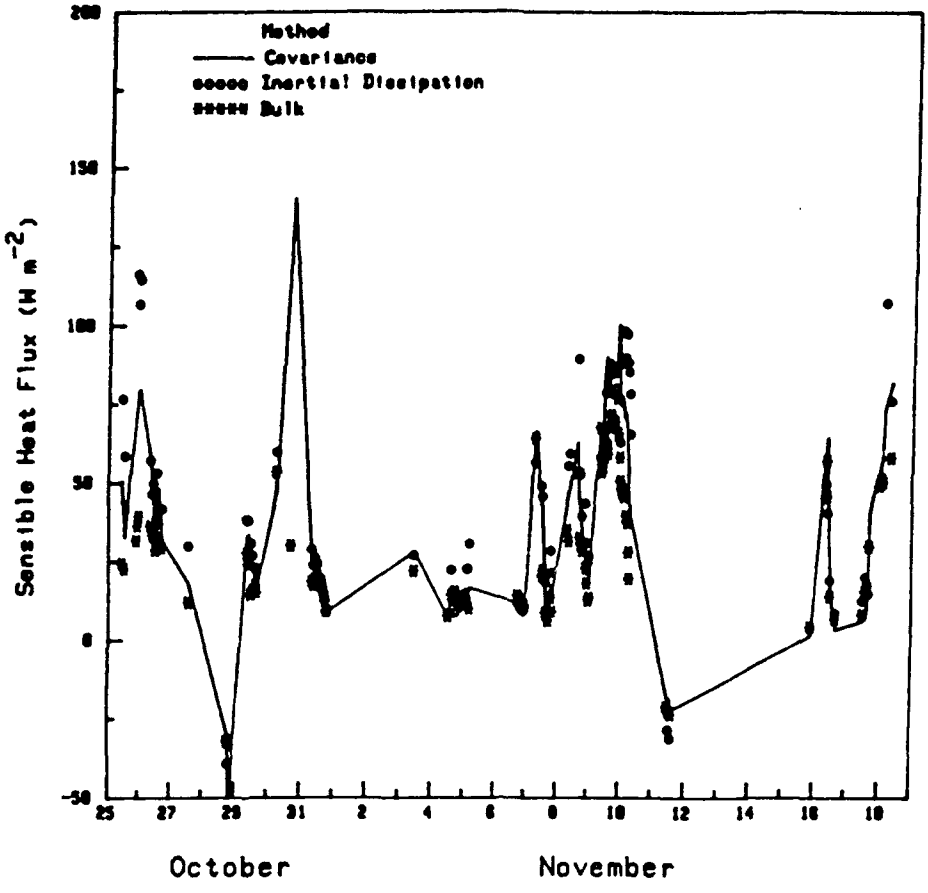

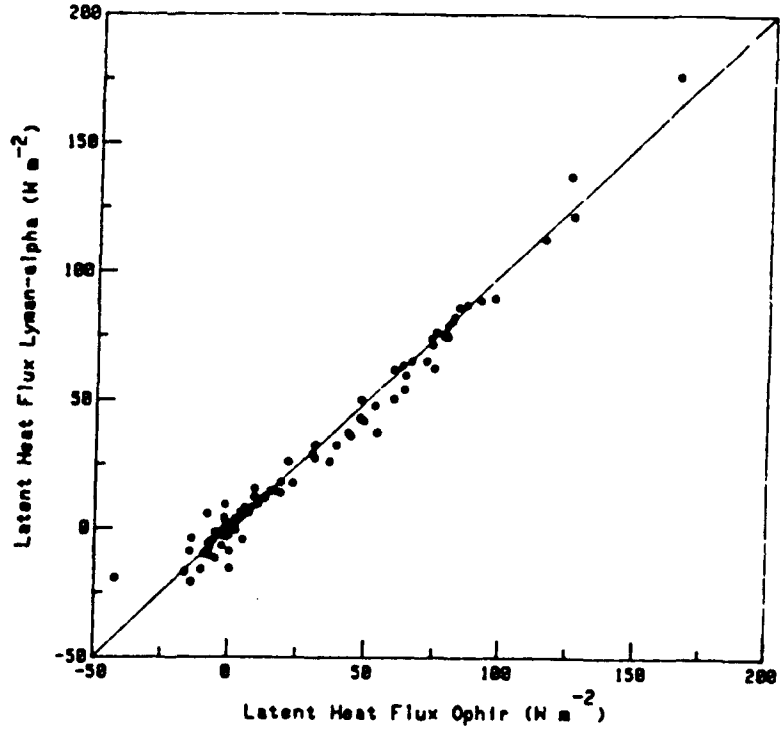

Figure 1. Upper panel: Time series of sensible heat flux measurements from the HEXMAX experiment. The solid line indicates direct measurements with a sonic anemometer, the open circles inertial-dissipation values with the sonic anemometer. The * indicates bulk formula calculations. Lower panel: comparison of latent heat flux measurements with an ultraviolet absorption hygrometer (Lyman-alpha) with a commercially produced infrared absorption hygrometer (OPHIR). Both are used in conjunction with a sonic anemometer.

SCIENTIFIC ACCOMPLISHMENT # 2

WHITECAP/SEA-SPRAY DROPLET MODEL

A model has been developed that is capable of simulating the contribution of sea-spray droplets to the evaporation of the ocean. The model includes a function for the sea surface droplet source strength based on the spectrum of bubbles in the water (due to whitecaps over the ocean). Droplet transport, evaporation, and deposition are also included. The model has a two-dimensional Langevin formulation that makes it easy to tailor to specific situations. Unlike previous Langevin approaches, this model takes into account the fall velocity and turbulent response time of the large spray droplets. The droplets are created by ejection from the surface, moved horizontally by a mean wind profile consistent with the Monin-Obukhov theory, and are subject to turbulent velocity fluctuations in both horizontal and vertical directions. The individual droplet evaporation is controlled by its size, temperature and the local profiles of temperature and relative humidity. At the moment, the droplet evaporation process does not feedback onto these profiles.

The model has been successfully tested in a variety of ways on to independent data sets obtained in a wind/water tunnel at IMST in France. Droplets were produced in the tunnel by breaking waves and by arrays of bubblers made of aquarium frits. Droplet concentration profiles were measured at various fetches downwind of the bubblers under a variety of wind and humidity conditions. Model simulations were found to agree very well with these simulations. For example, one key parameter for this process is the amount of liquid water

contained in the suspended droplets. Fig. 2 shows model and measured liquid water contents at two different ambient humidities. The next step in this process is to adapt the model for the oceanic condition. This requires that we account for sea salt effects, obtain the proper source function for the ocean, include wave-induced transport effects, and accommodate much longer fetches. More details of this work are provided in Appendix B.

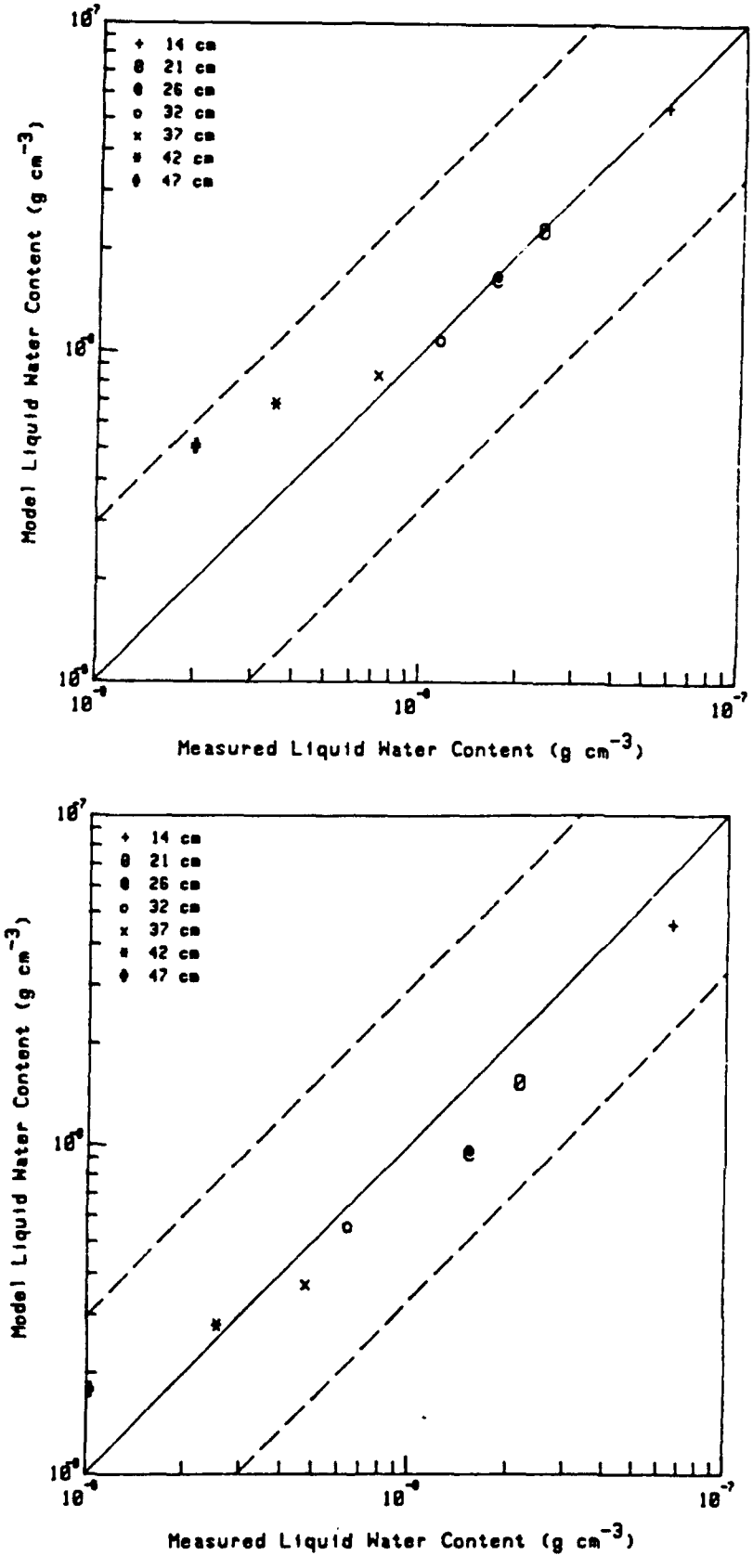

Figure 2. A comparison of model simulations and measurements of total liquid water concentration from sea spray droplets at various heights above the water. The upper panel is for a relative of humidity of 95% (basically non-evaporating conditions). The lower panel is for a relative humidity of 55%.

FUTURE NEEDS

Surface fluxes play an important role in a wide variety of air-sea interaction scientific problems from atmospheric boundary layer and ocean mixed layer dynamics, to cyclogenesis, and even climate. It is now imperative that measurement systems be developed and deployed on ships for measurements of fluxes over the open ocean. This is necessary because virtually all measurements used to compute bulk transfer coefficients in use today were obtained in coastal regions. Furthermore, the transfer coefficient approach is only correct on long term average, and is not sufficiently accurate for use in conjunction with research grade field programs (either meteorological or oceanographic), which are often concerned with events of short time scale.

In order to keep costs down, such a flux measuring package must exploit commercially available sensor and computer/data acquisition technology as much as possible. The system must feature realtime computation, storage and display of fluxes and be sufficiently robust that it can operate at sea for several months with only occasional cleaning of the sensors and changing of discs by an untrained and uninterested technician. This system should employ both the inertial-dissipation and direct flux methods. A considerable amount of research must be done to apply the inertial-dissipation method (developed and verified with research grade instruments) to environmentally robust sensors without sacrificing accuracy and to integrate ship motion sensing systems for direct measurements.

In the realm of scientific directions, two areas need immediate attention. The spray droplet model developed for this project should be modified to make it applicable to the open ocean so that it can be verified with oceanic droplet measurements and so that it can be used for its basic purpose - to evaluate the droplet contribution to air-sea fluxes. The second area is an examination of flux parameterizations in convective regions, or other regions with substantial mesoscale variability. Here the issue is to improve the flux computations for horizontal scales compatible with global numerical forecast models.

APPENDIX A

HEAT FLUXES, WHITECAPS, AND SEA SPRAY

C.W. Fairall, J.B. Edson, and M.A. Miller
Department of Meteorology
Pennsylvania State University
University Park, PA 16802

ABSTRACT

This report describes one aspect of a research project in air sea interaction conducted for the Office of Naval Research (contact N00014-85-K-0250). The project is concerned with the influence of sea spray on heat fluxes and the investigation of flux measuring techniques over the ocean. The results of the first two years of work on the sea spray problem will be summarized in this report. The problem is broken down into the natural physical processes: droplet production, transport, evaporation, and fluxes. The production is shown to be closely related to (but not linearly) to the fraction of whitecap coverage of the ocean. Estimates are given for the number of droplets produced as a function of droplet size and wind speed. The theory for the transport and evaporation of the droplets is developed in terms of size spectral densities for both droplet salt content (conservative) and droplet mass (non-conservative). The budget equations for the various thermodynamic variables are developed including the effects of the evaporating droplets to establish the theoretical basis for modeling the effects on the fluxes. The near surface production and transport effects on the droplet concentration profiles are discussed and the relationship between volume and areal source strengt' s is established. Finally, the present state of knowledge concerning the impact of sea spray on the scalar fluxes over the ocean is discussed.

CONTENTS

1. INTRODUCTION

1.1 Statement of the problem

The exchange of moisture and sensible heat between the atmosphere and the earth's surface is important in driving weather, climate, and a variety of factors of relevance to human activities (e.g., clouds, atmospheric optical properties, ocean mixed-layer dynamics) addressed by oceanography and meteorology. This exchange is often dominated by molecular and turbulent diffusive processes in the atmospheric surface layer (a region in contact with the surface on the order of 10 m thick where the height dependence of the fluxes is negligible). The exchange is quite dependent on the nature of the surface. Over land the roughness of the surface, the subsurface moisture and the transfer properties of the plant canopy complicate this exchange process. Ice and snow also have physical properties that require special treatment. Historically, the transfer processes over the ocean and over more solid surfaces have been interpreted and parameterized in terms of Monin-Obukhov similarity theory. The ocean has two unique properties that have greatly simplified this approach: the surface humidity is assumed to be in equilibrium with the saturation vapor pressure at the ocean surface temperature and the roughness is considered to be determined by the mean wind speed or friction velocity. This second assumption is now being recast in terms of the surface wave spectrum. However, the formation of whitecaps over the ocean strongly modifies the exchange process (see Slinn et al., 1978; Hasse, 1980; Coantic, 1980) for virtually all constituents (i.e., heat, moisture, trace gases, and particles). This modification is due to the release of gases and particles by the bursting of whitecap bubbles and, in the case of sensible and latent heat fluxes, the evaporation of the seawater spray droplets produced by the bursting bubbles.

The importance of droplets at high wind speeds has long been recognized (Montgomery, 1940). For example, Wu (1974) estimated that at a 10 m wind speed of 15 m/s as much water is lost from the oceans by evaporation of droplets as is lost by direct evaporation of the interface. The evaporating droplets distort the normal sensible/latent heat flux balance. In the absence of droplets, all of the surface moisture flux appears as a latent heat loss by the ocean and increases the salinity at the surface. Both effects destabilize the ocean mixed-layer. Sensible heat entrained at the top of the marine boundary layer is available to directly heat the ocean. In the presence of whitecaps, the droplet component of the moisture flux neither directly cools the ocean nor does it change the salinity but, instead, consumes a fraction of the entrained sensible heat. Thus, the dynamics of the oceanic and atmospheric boundary layers are changed. Furthermore, the droplets cause height dependent interactions between the sensible and latent heat fluxes near the surface and may lead to significant violations of the constant flux hypothesis that is central to the Monin-Obukhov similarity theory. This is significant to remote sensing of the ocean (particularly under strong wind conditions) in two obvious ways: (1) the algorithm used to extract meteorological information from the remote signal (e.g., radiance) may depend on similarity theory and/or (2) the application of the data (e.g., through atmospheric or oceanic models) may depend on similarity theory, the constant flux assumption or assumptions about the partition of latent and sensible heat and their effects on the ocean and atmosphere.

1.2 Scaling perspective

By correlating simultaneous measurements of vertical velocity and temperature fluctuations, the sensible heat flux (for example) can be determined near the surface

$$H_s = \rho c_p \overline{w'T'} \tag{1}$$

where ρ is the density and c_p the specific heat of air. While (1) is a mathematically precise definition of the heat flux, it does not transparently reveal the physical processes. Furthermore, the measurements required to use (1) are technologically and economically restricted to very local and intermittent operation. It is quite conceivable that a simple model could be written on a two thousand dollar PC that would require 10 billion dollars worth of measurements every day.

Through similarity theory the surface flux, H_{so}, can be expressed in terms of bulk atmospheric properties

$$H_{so} = \rho c_p \kappa\, u_*[T_s - \bar{\theta}(z)]/[\ln(z/z_{ot}) - \Psi_h(z/L)] \tag{2}$$

where θ is the potential temperature at height z, T_s the surface temperature, z_{ot} the roughness length for heat exchange, Ψ a function that expresses the effects of buoyancy, and L the surface layer buoyancy length scale. The friction velocity, u_*, is similarly proportional to the mean wind speed

$$u_* = \kappa\, \bar{u}(z)/[\ln(z/z_o) - \Psi_m(z/L)] \tag{3}$$

This provides some physical insight by suggesting that the heat flux is crudely proportional to the wind speed and the air-surface temperature difference with an additional, but weaker, dependence on the roughness of the surface. Following this approach, the latent heat flux is

$$H_{lo} = \rho L_e \kappa\, u_*[q_s - \bar{q}(z)]/[\ln(z/z_{oq}) - \Psi_q(z/L)] \tag{4}$$

where q_s is the specific humidity in the air immediately in contact with the surface and L_e is the latent heat of vaporization for water.

The micrometeorological community often expresses these relations in resistance law terms (Garratt and Hicks, 1973; Hicks et al., 1985)

$$H_{so} = \rho c_p [T_s - \bar{\theta}(z)]/(R_a + R_b) \tag{5a}$$

$$H_{lo} = \rho L_e [q_{sat}(T_s) - \bar{q}(z)]/(R_a + R_b + R_c) \tag{5b}$$

The turbulent transport resistance (or inverse of the conductance), R_a, is

$$\kappa u_* R_a = \ln(z/z_o) - \Psi_h(z/L) \tag{6}$$

The molecular sublayer transport resistance, R_b, is given by

$$\kappa u_* R_b = \ln(z_o/z_{ot}) \tag{7}$$

Observations and theory suggest that over land (Garratt and Hicks, 1973), over ice (Joffre, 1982) and over water (Liu et al., 1979) the sensible and latent heat roughness lengths decrease with increasing wind speed in aerodynamically

rough flow because of sheltering by the roughness elements. R_c expresses the interfacial resistance between the air and the bulk properties below the surface. Over the ocean this could represent the inhibition of evaporation by an organic surface film which is virtually always neglected. The enhanced release of water vapor by bursting bubbles could then be introduced by using a negative value for R_c.

The resistance interpretation of R_a is made clear by noting that in the constant flux region we can write

$$R_a = \int dz/K_h = \int \Phi_h/(\kappa u_* z)dz \qquad (8)$$

where K_h is the turbulent diffusion (or conduction) coefficient.

1.3 Scope of this Report

This report will focus on the role of sea spray and its effects on the scalar heat fluxes near the sea surface. It is believed that for realistic wind speeds, the droplets have little effect on the stress. However, to the extent that the heat fluxes are affected, there may be some influence on stress estimated by indirect methods that rely on similarity theory. We will not discuss effects (such as the wind speed dependence of the heat transfer roughness length) that fall within the conventional similarity treatment. Section 1.2 gives the conventional scaling approach to the scalar heat fluxes in the absence of droplets and provides a framework for breaking down the droplet problem in terms of interfacial processes (droplet production) and transport processes. In section 2 we will discuss the sea state, whitecaps, and the droplet source strength of the ocean. In section 3 we will discuss droplet microphysics including evaporation/condensation and the size spectral representation of droplet concentration. In section 4 we will present the conservation equation for droplets including evaporation and transport effects. This equation will be integrated with the conservation equations for temperature and moisture in the standard one-dimensional meteorological treatment. This will provide the formalism for describing, at least in principle, the effects of droplets on the scalar fluxes. Following a discussion of the relation of the droplet profiles and the surface source (Section 5), Section 6 will be a discussion of the various approaches that have been taken to study the problem, where they have taken us and what new work is on the immediate horizon.

2. BACKGROUND ON DROPLET PRODUCTION

2.1 Whitecaps and sea state

The term 'sea state' refers to the classification of the wave and whitecap condition of the ocean, usually through mean wind estimates or eyeballing the surface appearance. For our purposes, the whitecap coverage is most closely related to the droplet production and, indirectly, vertical transport of droplets. When an ocean wave breaks, it entrains a volume of air which evolves into a spectrum of rising bubbles which give the characteristic appearance of a white patch. Typically, about 1 percent of the ocean surface is covered by whitecaps (Blanchard, 1971). Monahan et al. (1982) used photographic techniques to develop an empirical formula for the fraction of whitecap coverage, W_f, as a function of wind speed

$$W_f = 3.84 \times 10^{-6} u^{3.4} \qquad (9)$$

For more detail we suggest the monograph "Oceanic Whitecaps" by Monahan and Mac Niocaill,(1986)

2.2 Bubbles and droplets

When a whitecap bubble bursts at the surface, it produces two types of droplets: film drops from the ejection of the thin bubble film and jet drops which are formed from the destabilization of the vertically rising jet of water from the collapsing bubble cavity (Kientzler et al., 1954; Blanchard, 1975; Resch, 1986). Cipriano and Blanchard (1981) and Cipriano et al. (1983) find that most of the droplets smaller than 10 μm originate as film droplets. Jet drops are typically 1/10th the size of the parent bubble (bubble sizes are usually in the 0.1 to 2.0 mm diameter range). One to five jet drops are produced per bubble. The rate of production of jet drops on a microphysical scale is much better known than that for film drops, which is still the subject of heated debate (e.g., Cipriano et al., 1987). It is now known that the larger size droplets (greater than 10 μm radius) dominate the liquid water production by sea spray (Stramska, 1987; Miller, 1987; Edson, 1987), so our poor understanding of film droplets will not handicap the analysis of the effects on the heat fluxes (the same is not true if one's interest is in Aitken nuclei, optically relevant aerosols, or cloud condensation nuclei). While it is believed that there is a direct connection between the oceanic whitecap bubble spectrum, the incredible variety of bubble spectra in the literature suggests much more variability than is observed in the sea spray spectra. This issue is considerable clouded by the effects of temperature, organic contaminates, and even bacteria.

There is also considerable evidence that bubbles are not the only source of droplets. At wind speeds in excess of 13 m/s there is a rapid increase in the observed sea salt aerosol concentrations at large sizes (Monahan et al., 1983; Fairall et al., 1983). It has been postulated that this increase is due to the additional production of droplets by the so-called 'spume' mechanism where the strong turbulence simply blows the foam patch right off the top of a breaker. This phenomenon can be easily observed at high winds and its appearance threshhold constitutes a criteria for sea state 7.

2.3 Oceanic droplet source strength

The droplet surface source strength is crudely defined as the number of drops of a given size interval produced by each square centimeter of the ocean each second. Clearly, this strength is a function of sea state as characterized by whitecap fraction and/or wind speed. Additional information is required to define the source function because at each size the particles are ejected with a distribution of initial vertical velocities (Blanchard and Woodcock, 1957). The usual approach is to assume that the droplets magically appear at the top of their most probable trajectory (Edson, 1987). In other words, the droplets are treated as being created by a distribution of elevated sources. The typical ejection height is on the order of 5 cm. This approach is justifiable because the time scale for this process is quite small compared to the turbulent transport time scales. Ling and Kao (1976) even broke down the source function by location on the wave (e.g., crest, trough, etc.), but for fluxes (which are usually averaged over hundreds or thousands of waves) this may be an unnecessary detail. The effect of the large ocean waves on the source function and the subsequent transport of the droplets is usually ignored. More than one study of large droplet concentrations near the ocean surface (Preobrazhenskii, 1972; de Leeuw, 1986) has shown the droplets to be rather uniformly distributed in the vertical below the typical wave height. He attributes this to strong mixing by the 'rotor' flow induced by the motion of the wave (in a wave following coordinate system the rotor appears as an eddy in the wave trough). Strictly speaking, this is a transport issue and is not related to the source function but it may be of relevance in inferring the source function from indirect measurements.

Three approaches have been taken to establish the source strength: convolution of the bubble spectra with ejection height, laboratory simulations of whitecaps, and budget computations from marine measurements of particles. Edson (1987) used the first approach as the source function for input to a Lagrangian model of a droplet plume from a laboratory whitecap produced in the wind tunnel at IMST, Marseille, France. In this approach, the number/cc/sec of bubbles of a given size interval reaching the surface is simply the product of the bubble concentration spectrum, n_b, and the bubble rise speed, w_b. Thus, the number source strength spectrum, S_{ni}, is

$$S_{ni}(r) = n_b(a)\, w_b(a)\, N_e(a) \qquad (10)$$

where N_e is the average number of droplets ejected well out of the diffusion sublayer by a bubble of radius a and r is the average radius of the droplet ejected by a bubble of radius a (i.e., r=a/10). The subscript n implies that this is a number density spectrum and the subscript i designates the this is a source that is realized as a distribution within a few centimeters of the interface. Assuming a power law for the bubble size spectrum (Monahan and Zietlow, 1969), the observed droplet concentrations were obtained by adjusting the bubble spectrum (Fig. 1). Of course, this only yielded the source function for a foam patch produced in a tank in a wind tunnel, but the basic approach holds promise for the future as measurements of oceanic bubble spectra become more reliable and reproducible.

Monahan et al. (1982, 1986) used a second method to estimate to source function. He hypothesized that the number of sea spray droplets produced per unit area of sea surface per unit time is simply equal to the fraction of the sea surface over which whitecaps decay per unit time multiplied by the number of spray droplets, n_w, produced during the total lifetime of a whitecap of unit area. Thus,

$$S_{ni} = W_f(u)\, n_w(r)/\tau_w \qquad (11)$$

where W_f is obtained from (9) and τ_w is the decay time (about 7 sec) of a typical whitecap. The key number concentration spectrum, n_w, is obtained by measuring the increase in the number of particles in an enclosed volume produced by the creation and decay of a single whitecap of known area. This was done by measuring the aerosol number concentration with conventional optical particle counters. The interpretation is clouded by the fact that the measurements are done either in the absence of turbulence or with the turbulence produced by the measuring device. Thus, some unknown fraction of the particles produced may be lost to deposition before they are counted. A variation on this approach has been used by Ling et al., (1978), who used a laboratory hydraulic jump to 'freeze' a breaker to permit droplet measurements with a realistic mean air flow. This approach also holds promise for the future when improvements in technology will permit faster and more accurate measurements of droplet concentration very near the surface.

The source strength can, in principle, be measured directly over the ocean. It is clearly defined in terms of the particle flux very near, but immediately above, the droplet effective source region (see Section 3 for an explanation of the terminology)

$$S_{ni} = (\overline{w'n'(r)})_\delta \qquad (12)$$

where the overbar denotes the ensemble average, the primes denote turbulent fluctuations about the mean, and the subscript δ implies the measurement is taken just above the droplet source region. The covariance term is the droplet flux due to turbulence. The velocity-particle covariance has presented such severe measurement technology problems (Fairall, 1984) that, to date, it has only been inferred as a residual from the particle budget equations (Fairall et al., 1983; Miller,1987). Thus, it is common to see this approach referred to as the budget method. If the time derivative term in the budget is neglected, then this is referred to as the equilibrium method. The budget methods are based on measurements of particle concentration to infer the flux and the source strength.

The various methods have been analyzed and compared in the recent review by Miller (1987) who produced a consensus source function (Fig. 2). The deviation of a particular source spectrum from the consensus value is typically a factor of three. Some of this uncertainty is due to confusion about the exact nature of the source function. Miller used an interpretation from Fairall and Larsen (1984) that can be traced to gas transfer theory (Slinn et al., 1978), while (12) is based on the vertical integral of the continuity equation in the source region (see Section 3). Further uncertainty is introduced by the extrapolation of elevated measurements to the surface and corrections for the effects of evaporation (e.g., Fairall et al., 1983). If the goal is to use the continuity equation to predict evolutions of sea spray concentrations (i.e., aerosols) at some reference height, then the budget method has the advantage that it is, to some extent, automatically 'tuned' to fit the data--including the effects of spume production at high wind speeds. This may not be adequate in investigating the impact of spray on the heat fluxes, where the details in the height region of maximum evaporation are quite important. Furthermore, the source function in Fig. 2 is not adequate for our purposes because it does not extend into the primary evaporation production size region (20 μm $<r<$ 70 μm). Thus, the droplet source remains a major unsolved problem.

3. DROPLET MICROPHYSICS

3.1 Basic transport

Consider an atmospheric concentration, χ, which is a standard quasi-conservative meteorological variable such as the concentration of water vapor, aerosol dry mass or carbon dioxide. The basic conservation equation for this variable (Businger, 1982) can be written

$$D\chi/Dt = D_\chi \nabla^2(\chi) + s_\chi \tag{13}$$

where D_χ is the molecular diffusivity, s represents the net source and D/Dt denotes the Lagrangian time derivative

$$D\chi/Dt = \partial\chi/\partial t + \partial(u_i\chi)/\partial x_i \tag{14}$$

and u_i are the velocity components for the coordinates x_i for i=1,2,and 3 and the Einstein convention of summing repeated indices is used (see the discussion in Businger, 1982). In the case of particles, we must allow for the possibility of a velocity difference (called the slip velocity, u_s) between the particle and the air. Also, we recall that the particle diffusivity is a function of particle size. Thus, (13) is written with u_i explicitly as the fluid motion

$$\partial\chi/\partial t = -\partial[(u_i+u_{si})\chi - D_p\partial\chi/\partial x_i]/\partial x_i + s_\chi \tag{15}$$

We now expand the variables of (15) in terms of a mean and fluctuating component (see Businger, 1982, for details)

$$\chi = \bar{\chi} + \chi' \tag{16a}$$

$$u_i = \bar{u}_i + u_i' \tag{16b}$$

$$u_{si} = \bar{u}_{si} + u_{si}' \tag{16c}$$

The budget equation for the mean component is

$$D\bar{\chi}/Dt = -\partial[\overline{\chi' u_i'} + \overline{\chi' u_{si}'} + \bar{\chi}\,\bar{u}_{si} - D_p\partial\bar{\chi}/\partial x_i]/\partial x_i + \bar{s}_\chi \tag{17}$$

The quantity inside the square brackets is interpreted as a particle flux due to transport by turbulent velocity fluctuations, slip velocity fluctuations, mean slip velocity and Brownian diffusion. For droplets, it is normally assumed that the only nonzero mean slip velocity is that due to gravity,

$$(\bar{u}_{s1}, \bar{u}_{s2}, \bar{u}_{s3}) = (0, 0, -w_s) \tag{18}$$

For particles smaller than about 50 μm radius, this is well approximated by the Stokes formula (Pruppacher and Klett, 1978),

$$w_s = 2\,(\rho_p/\rho)gr^2/(9\nu) \tag{19}$$

where ρ_p is the ambient particle density, g the acceleration of gravity and ν the kinematic viscosity of air. The concentration-slip covariance term is believed (perhaps 'hoped' is the better word) to be negligible except very near the interface where it is responsible for the inertial impaction

deposition mechanism (Slinn et al.,1978).

Following the formalism developed in Businger (1982) for scalar fluctuations (e.g., temperature and humidity), we can obtain budget equations for particle concentration variance or particle-velocity covariances. Because of the additional complication of the slip velocity, this becomes even more complex than the standard scalar fluctuations. Those with such masochistic tendencies are invited to study the treatment by Lewellen et al. (1977).

3.2 Evaporation

Consider a single droplet of mass, m_p, given by

$$m_p = 4\pi\rho_p r^3/3 \tag{20}$$

We assume that the particle is a saltwater solution so that

$$\rho_p = \rho_w + (\rho_o-\rho_w)r_o^3/r^3 \tag{21}$$

where ρ_w is the density of water, ρ_o the density of the particle with all water removed to produce a dry radius, r_o.

If the water vapor pressure exerted by the droplet, e_p, is greater than its surroundings, e, then the droplet will evaporate at a rate given by (Fuchs,1959; Pruppacher and Klett, 1978)

$$\partial m_p/\partial t = 4\pi f_p D_v r[e_p(r,r_o,T_p)-e]/(R_v T) \tag{22}$$

where f_p is a ventilation factor given approximately by

$$f_p = [1+0.25(2w_s r/\upsilon)^{.5}] \tag{23}$$

The droplet vapor pressure can be converted to an effective saturation vapor density or specific humidity, q_p, at the surface of the droplet to yield

$$\partial m_p/\partial t = -4\pi f_p D_v r\rho(q_p-q) \tag{24}$$

From Fitzgerald (1975) we estimate q_p by

$$q_p = q_{sat}(T_p)[1-Tr_o^3/(r^3- r_o^3)] \tag{25}$$

where q_{sat} is the saturation value for pure water with no surface curvature at the droplet temperature, T_p, and T a parameter that depends on the chemistry of the dry component (T=1 for sea salt).

A spray droplet released from the ocean will loose water mass by evaporation until it approaches a state of equilibrium. A pure water droplet will completely evaporate but a salt water droplet will usually retain a considerable amount of water in equilibrium. The equilibrium condition is defined by setting $\partial m_p/\partial t=0$. From (24) and (25) this defines an equilibrium particle size, r_e,

$$r_e/r_o = G(S) = [1 + T/(1-S)]^{1/3} \tag{26}$$

where we have assumed that $T_p=T$ in equilibrium and S is the ambient water vapor saturation ratio. Surface seawater is typically 3.5% salt by mass and

(what?)

has a specific density ρ_p/ρ_w=1.028. If we assume a density of 2.2 for crystalline salt, then a seawater droplet has r/r_o=3.6. A typical marine atmospheric relative humidity of 80% (S=0.8) at a height of 10 m over the ocean used in (26) gives r_e/r_o=1.8. A droplet in equilibrium at these conditions will have shrunk to one half its radius since leaving the ocean and lost about 90% of its water to evaporation. One word of caution, (26) only describes the particle in the deliquescent state; if the relative humidity falls below about 60%, the particle will undergo a first order transition to a dry, crystalline state characterized by the radius r_o (Pruppacher and Klett, 1978).

The rate of change of size of an evaporating droplet is obtained by taking the derivative of (22) using (21)

$$\dot{r}_p = \partial m_p/\partial t/(4\pi r^2 \rho_w) \tag{27}$$

Combining with (25), this can be written

$$\dot{r}_p = -A\, q_{sat}(T)\, r^{-1}((1-\alpha)(1-T/[(r/r_o)^3-1])-S) \tag{28}$$

where

$$A = f_p D_v \rho/\rho_w \tag{29}$$

The factor α is necessary because the evaporating droplet is assumed to be at the 'wet bulb' temperature (Pruppacher and Klett, 1978), T_w,

$$\alpha = L_e/(R_v T^2)(T-T_w) \tag{30}$$

Edson (1987) has shown that the time for even 100 μm droplets to reach the wet bulb temperature is small compared to the turbulence integral time scale at the particle ejection height. If we neglect the α factor, then (28) can be written

$$\dot{r}_p = -A\, q_{sat}(T)\, r^{-1}(1-S)[(r/r_e)^3-1](1/T+1) \tag{31}$$

This expression illustrates several characteristics of droplet evaporation. The cubic term implies a strong tendency to stay near equilibrium. The 1/r term implies small particles lose size more rapidly (but not mass). The (1-S) term implies that equilibrium is approached more quickly under drier conditions.

3.3 The particle size spectral density

In Section 3.1 we discussed the transport of particles or droplets in terms of the concentration variable, χ, which we were careful not to define explicitly. A variety of concentration variables are used in the literature, the simplest is the total number concentration, N(r), which is the total number of particles per unit volume of air with radius smaller than r. The size spectral density, n(r), is the number per unit volume with radius greater than r-dr/2 but less than r+dr/2 and is directly related to N(r)

$$N(r) = \int_o^r n(r')\, dr' \tag{32}$$

We can also define the volume spectral density, v(r),

$$v(r) = (4\pi/3)r^3 n(r) \tag{33}$$

These distributions describe the salt water solution droplets as they appear under ambient conditions. We can define a quasi-conservative variable (more in keeping with the philosophy of χ) in terms of the mass of salt in the particles or, equivalently, the dry radius of the particles. For example, we can define the size spectral density that would result if the particles were dried out completely as $n_o(r_o)$. The total number of droplets per unit volume with dry radius less than r_o is $N_o(r_o)$ so that

$$N_o(r_o) = \int_o^{r_o} n_o(r_o')\, dr_o' \tag{34}$$

Under equilibrium conditions, the number concentrations are related by

$$N_o(r_o) = N(r_o G_e(S)) \tag{35}$$

which implies the spectral densities are related by

$$n_o(r_o) = \partial N_o/\partial r_o = \partial N/\partial r\ \partial r/\partial r_o = n(r)G_e(S) \tag{36}$$

While n_o is a quasi-conservative variable, n(r) is not because the droplets change their size while evaporating. If we think of the rate of change of radius as a 'velocity' in radius space, it is easy to see (Clark, 1973) that the time derivative of n(r) must modified as in (14)

$$Dn_o/Dt = \text{Transport} + \text{Source} \tag{37a}$$

$$Dn/Dt + \partial(r_p n)/\partial r = \text{Transport} + \text{Source} \tag{37b}$$

Thus, (37a) is simply (15) expressed for $\chi = n_o$ but the analogous equation for the non-conservative variable, n(r), requires the additional term on the left hand side. The budget equations for the ensemble averaged particle concentrations become (Clark, 1974; Clark and Hall, 1979)

$$D\bar{n}_o/Dt = -\partial[\overline{n_o'u_i'} + \overline{n_o'u_{si}'} + \bar{n}_o\bar{u}_{si} - D_p\partial\bar{n}_o/\partial x_i]/\partial x_i + \bar{s}_{no} \tag{38a}$$

$$D\bar{n}/Dt + \partial[\bar{n}\,\bar{r}_p + \overline{n'r_p'}]/\partial r = -\partial[\overline{n'u_i'} + \overline{n'u_{si}'} + \bar{n}\,\bar{u}_{si} - D_p\partial\bar{n}/\partial x_i]/\partial x_i + \bar{s}_n \tag{38b}$$

Two budget equations are required, one to keep track of the salt (38a) and one to keep track of the salt plus water (38b). Notice that in order to use (27), we must be able to specify the value of r_o that is appropriate for each value of r. This is done by finding the value of r such that

$$N(r) = N_o(r_o) \tag{39}$$

Recall in Section 3.1 those with a masochistic interest in quasi-conservative particle concentration fluctuation statistics were referred to Lewellen et al. (1977). Such relations are generated from the budget equations for the fluctuating quantities such as $\partial u_i'/\partial t$. In the interest of establishing historic precedent, we will give the budget equation for the fluctuating ambient particle concentration:

$$\partial n'/\partial t = -\partial[n'\bar{\dot{r}}_p+\bar{n}\,\dot{r}_p'+n'\dot{r}_p'-\overline{n'\dot{r}_p'}]/\partial r-\partial[u_i'\bar{n}+\bar{u}_i n'+u_i'n'-\overline{u_i'n'}-D_p\partial n'/\partial x_i]/\partial x_i+s_n' \quad (40)$$

The ambient particle concentration variance budget equation is obtained by multiplying (40) by n' and taking the ensemble average. The flux budget is obtained by combining (40) with the $\partial u_i'/\partial t$ budget.

4. COUPLING OF DROPLETS, WATER VAPOR AND TEMPERATURE

4.1 Basic budget equations

The standard meteorological budget equations in 1-dimensional form are written

$$D\bar{\theta}/Dt = -\partial(\overline{w'\theta'})/\partial z - (L_e/c_p)\bar{E} \qquad (41a)$$

$$D\bar{q}_v/Dt = -\partial(\overline{w'q_v'})/\partial z + \bar{E} \qquad (41b)$$

$$D\bar{q}_l/Dt = -\partial(\overline{\cdots q_l'} - \langle\bar{w}_s\rangle\bar{q}_l)/\partial z - \bar{E} \qquad (41c)$$

where θ is the potential temperature, q_v is the specific humidity (vapor), q_l the specific humidity (liquid), $\langle w_s\rangle$ the volume averaged fall velocity, and E the total evaporation rate

$$\bar{E} = -(4\pi\rho_w/\rho)\int_o^\infty r^2\,[\bar{r}_p\bar{n}(r)+\overline{r_p'n'}(r)]\,dr \qquad (42)$$

Note that the molecular diffusion terms have been dropped because they are only relevant in the diffusion sublayer (within a mm of the interface). The liquid water content is the integral over the droplet distribution

$$\bar{q}_l = (4\pi\rho_w/3)\int(r^3-r_o^3)\bar{n}(r)\,dr \approx (4\pi\rho_w/3)\int r^3\,\bar{n}(r)\,dr \qquad (43)$$

In the same simplified 1-dimensional form, the particle budget equations become

$$D\bar{n}_o/Dt = -\partial[\overline{w'n_o'} - \bar{w}_s\bar{n}_o]/\partial z + \bar{s}_{no} \qquad (44a)$$

$$D\bar{n}/Dt = -\partial(\bar{r}_p\bar{n}+\overline{r_p'n'})/\partial r - \partial[\overline{w'n'} - \bar{w}_s\bar{n}]/\partial z + \bar{s}_n \qquad (44b)$$

Again, note that the terms believed to be negligible above the molecular sublayer have been dropped from these expressions. Also note that the basic liquid water conservation equation (41c) can be obtained from (44b) by converting number density to mass density and integrating over all radii.

4.2 The fluxes

The effects of the evaporating droplets on the sensible and latent heat fluxes can be viewed in several ways. A straightforward turbulence interpretation is obtained by creating the second-order budget equations analogous to (41). As we discussed in Section 3.3, there are two types of second-order budget equations: variance and covariances (see Businger, 1982). The covariances are the fluxes but the variances may be of interest for the inertial-dissipation flux methods (Fairall and Larsen, 1986). For example, the standard humidity variance equation becomes

$$\partial(\overline{q_v'q_v'})/\partial t + 2\overline{q_v'w'}\partial\bar{q}_v/\partial z + \partial(\overline{q_v'q_v'w'})/\partial z + X_q = 2\overline{q_v'E'} \qquad (45)$$

where X_q is the rate of dissipation of the vapor variance. Besides the

direct and obvious influence of the term on the right hand side of (45), the droplets also influence the other terms indirectly by changing the mean and flux profiles. In the inertial-dissipation flux method, the flux is estimated from measurements of the dissipation by using an empirical balance of (45) in Monin-Obukhov form

$$H_{lo} = \rho L_e [0.5\ u_* \kappa z X_q / \Phi_h(z/L)]^{1/2} \tag{46}$$

However, even if the balance of the normal terms is not disrupted by the droplets, we must now include the evaporation source term

$$H_{lo} = \rho L_e [0.5\ u_* \kappa z (X_q - 2\overline{q_v' E'}) / \Phi_h(z/L)]^{1/2} \tag{47}$$

The covariance budget equations provide a formalism for evaluating the effects of droplets but the complexity of second-order closure models has discouraged their application in this way so far. A simpler approach is to use the conventional eddy-diffusion coefficient (or, first-order closure) model. This method is also often referred to a K-theory. Following the analogy of the molecular diffusion flux expression, the turbulent flux is written

$$\overline{w' q_v'} = -K_h \partial \bar{q}_v / \partial z \tag{48}$$

where K_h is the scalar gradient diffusion coefficient. Within the realm of Monin-Obukhov similarity theory, we can write

$$K_h = \kappa z u_* / \Phi_h(z/L) \tag{49}$$

Normally, the humidity gradient takes a form so that the turbulent flux is constant in the surface layer

$$\partial \bar{q}_v / \partial z = -\overline{w' q_{vo}'} / (\kappa z u_*) \Phi_h(z/L) \tag{50}$$

Clearly, evaporating droplets are capable of modifying the moisture profile so that it deviates from (49) and, even if the K coefficient is unchanged, that will produce a change in the flux profile. Since the droplet effects on the heat fluxes will only be important under rather strong wind conditions, we can be confident in the using the neutral approximation to (49)

$$K_h = \kappa z u_* \tag{51}$$

The K-theory approach is considered to be particularly appropriate for the droplet transport problem because K-theory is at its best in the surface layer.

5. RELATING PROFILES, FLUXES AND THE SOURCE FUNCTION

5.1 Defining the droplet source

The source functions discussed in Section 2.3 were defined in terms of a particle flux (#/area/sec.) at the interface. The source that appears in the budget equations is a volume source (#/volume/sec.). The volume source is clearly defined and requires no interpretation. The area source as defined by (10) is also unambiguous, but it is not clear how it is related to the volume source. This is a particular difficulty when one attempts to deduce the area source term from measurements at 10 m (e.g., the budget method). If we assume that the source can be defined by ignoring the initial upward trajectory of the droplets, then we can write

$$\partial \bar{n}_o/\partial t = -\partial[\overline{w'n_o'} - \bar{w}_s\bar{n}_o]/\partial z + \bar{s}_{no} = -\partial[\overline{w'n_o'} - \bar{w}_s\bar{n}_o + \bar{S}_{no}]/\partial z \qquad (52)$$

where we have defined the area source by

$$\bar{S}_{no}(z) = \int_z^\infty \bar{s}_{no}(z')\, dz' \qquad (53)$$

We are still assuming that the source appears well above the molecular sublayer so we can neglect the slip-covariance and Brownian diffusion terms. Defined in this manner, S(0) is the total area source while S(z)=0 for $z>\delta$ where δ is the maximum ejection height for each radius. Notice that if we make the simplification that each size particle is created at its average ejection height, then s(z) takes the form of a delta function and S(z) is a step function.

5.2 Profiles and the source function

We can now define a total flux variable, F_{no}, by

$$\bar{F}_{no} = \overline{w'n_o'} - \bar{w}_s\bar{n}_o + \bar{S}_{no} = -K_h\partial\bar{n}_o/\partial z - \bar{w}_s\bar{n}_o + \bar{S}_{no} \qquad (54)$$

We now postulate that F is the flux variable that is constant in the 'constant flux' surface layer. Let us consider a trivial condition where there is no turbulence and a balance exists between the source and gravitational removal. In other words, particles are being created at the height δ and falling into the ocean. In equilibrium, this balance is expressed by F=0, which leads to a mean concentration profile given by

$$\bar{n}_o = \bar{S}_{no}/\bar{w}_s \qquad ;z<\delta \qquad (55a)$$

$$\bar{n}_o = 0 \qquad ;z>\delta \qquad (55b)$$

If we use the neutral limit for the eddy diffusion coefficient and assume that evaporation is negligible, then a simple profile can be obtained by assuming a balance between turbulence and gravitational settling above the source region (Toba, 1965)

$$\bar{n}_o = \bar{n}_o(\delta)[z/\delta]^{-\beta} \qquad ;z>\delta \qquad (56)$$

where the exponent, β, is defined by

$$\beta = \bar{w}_s/(\kappa u_*) \tag{57}$$

For a step function area source the profile in the source region is

$$\bar{n}_o = \bar{S}_{ni}/\bar{w}_s + (\bar{n}_o(0) - \bar{S}_{ni}/\bar{w}_s)[z/z_o]^{-\beta} \quad ;z<\delta \tag{58}$$

The source function can be estimated from (58) evaluated at $z=\delta$ and using (57) to eliminate $n_o(\delta)$ and solve for S in terms of a concentration measured at some reference height, z_r,

$$\bar{S}_{ni} = \bar{w}_s[\bar{n}_o(z_r)(z_r/\delta)^{\beta} - \bar{n}_o(0)(\delta/z_o)^{-\beta}]/[1-(\delta/z_o)^{-\beta}] \tag{59}$$

Since the (δ/z_o) terms are probably negligible, we find

$$\bar{S}_{ni} = \bar{w}_s\bar{n}_o(z_r)\ (z_r/\delta)^{\beta} \approx w_s\bar{n}_o(\delta) \tag{60}$$

5.3 The constant flux assumption

While (60) appears to be a simple way to estimate the source function from concentration measurements, it has the disadvantage that the non-evaporating assumption is not applicable in our cases of interest. The constant flux assumption can be used to estimate S from measurements at some reference height, z_r, well above the source region. At the reference level

$$\bar{F}_{no}(z_r) = \overline{w'n_o'}(z_r) - \bar{w}_s(z_r)\bar{n}_o(z_r) \tag{61}$$

For particles large enough to be of interest to us, both the eddy diffusion coefficient and the mean concentration gradient will be fairly small below the average ejection height so we can approximate the flux near the interface by

$$\bar{F}_{no}(0) = -\bar{w}_s(0)\bar{n}_o(0) + \bar{S}_{ni} \tag{62}$$

By equating (56) and (57) we find

$$\bar{S}_{ni} = \overline{w'n_o'}(z_r) - \bar{w}_s(z_r)\bar{n}_o(z_r) + \bar{w}_s(0)\bar{n}_o(0) \tag{63}$$

If there is a near balance between the turbulent transport and gravitational settling, then the first two terms cancel and

$$\bar{S}_{ni} = \bar{w}_s(0)\bar{n}_o(0) = \bar{w}_s(\delta)\bar{n}_o(\delta) \tag{64}$$

For smaller particles with relatively small fall velocities, the vertical concentration gradient is small and the last two terms cancel to give

$$\bar{S}_{ni} = \overline{w'n_o'}(z_r) \tag{65}$$

This last expression was used by Fairall et al. (1983) to estimate S for sea salt particles of relevance to optical propagation.

6. IMPACT ON THE FLUXES

6.1 Opening comments

Water can be transferred from the ocean to the atmosphere by direct evaporation or the evaporation of sea spray with subsequent transport to the troposphere by turbulence and large scale convection. Above the droplet evaporation zone, this transfer appears as a water vapor flux. Within the evaporation zone, the flux is partitioned between vapor flux and liquid (i.e., droplet) flux. Within the evaporation zone the evaporation influences the profiles of temperature and moisture. Evidence that this process is important is relatively sparse, primarily because of the difficulty of the measurements. If we assume that the total (liquid plus vapor) flux is roughly constant with altitude, then the appearance of the liquid flux in the evaporation zone would probably have the effect of reducing the vapor flux. Evidence for this has been observed in aircraft vapor flux profiles over the ocean which often indicate a maximum in the vapor flux in the lower boundary layer (LeMone and Pennell, 1976; Nicholls and Readings, 1979).

Another obvious manifestation of sea spray effects on the heat fluxes is expected to appear in the heat transfer coefficients-either the resistances described in the introduction or the bulk transfer coefficients (C_h and C_e) described earlier. Clearly, these different parameters are related [e.g., $C_h = 1/u/(R_a + R_b)$]. It is generally believed that droplet evaporation should lead to some increase in the neutral moisture transfer coefficient at high wind speeds. The anticipated effect on the heat transfer coefficient is not obvious and could be quite sensitive on the reference height used. This belief has led to some investigation of the wind speed dependence on the transfer coefficients (Francey and Garratt, 1979; Anderson and Smith, 1981). The interpretation is also confused by the theoretical predictions that the transfer coefficients should decrease slowly with increasing wind speed (e.g., Liu et al., 1979) in the absence of sea spray. Thus, if the transfer coefficients were constant with wind speed this might be interpreted as evidence for enhancement. In the summaries of transfer coefficient measurements given by Friehe and Schmitt (1976) and Anderson and Smith (1981) there are very few measurements for winds above 10 m/s and most of those are not from the open ocean but are from beach sites where there are probably surf effects. Francey and Garratt (1979) found both transfer coefficients to increase with increasing wind speed; suprisingly, the sensible heat coefficient increased faster than the moisture coefficient. In a recent survey of bulk parameterizations by Blanc (1985), only one of ten schemes projected scalar transfer coefficients that decreased with increasing wind speed.

In general, a number of avenues are available to attack this problem. Historically, the most work has been done using numerical integrations of the budget equations. Recently, a research program (the Humidity Exchange Over the Sea--HEXOS) was begun to study this problem. This program has been described by Katsaros et al. (1987) so we won't go into great detail. The HEXOS program is investigating this problem with a combination of numerical model studies, field measurements, and wind tunnel simulations. The tunnel work has been given the subacronym HEXIST (the ST denoting the Simulation Tunnel at the IMST Laboratoire de Luminy near Marseille, France).

6.2 Eulerian ensemble average numerical models

Meteorology has a rich history of numerical model simulations of

atmospheric boundary layer structure and dynamics. Many different types of models have been used: mixed-layer (zero-order closure), eddy diffusion (first-order closure), second-order closure, and large eddy simulations (LES). Most boundary layer models have a total vertical domain of several km and no attempt is made to resolve surface layer structure. Instead, the lower boundary conditions and the lowest level of the model atmosphere are related to the surface fluxes by Monin-Obukhov similarity as described previously. Such models could be used for our purposes by nesting a high resolution surface layer and solving the equations presented in Section 4.1, but, as yet, this has not been done.

Burk (1984) made a major step in this direction when he simulated sea salt aerosol structure within a second-order closure ABL model, but he did not add a high resolution surface layer. He simplified the computational process by transporting the aerosols with an eddy diffusion coefficient (rather than solving the second-order particle covariance equation). Evaporation was not treated explicitly but the particles were assumed to be in a state of evaporative equilibrium using a function similar to (26). Thus, only the dry concentration budget equation (44a) was used. Since Burk was primarily interested in evaluating aerosol profiles throughout the ABL, near surface evaporation was not looked at and evaporation did not feedback onto the scalar profiles. In his simulations, the mass mode radius was relatively independent of wind speed (from Beaufort Force 3 to BF5) with a typical value of 3 μm (dry). This is not consistent with the measurements of Woodcock (1953) where the mode radius increased from 3 μm to more than 10 μm over the same range but not all subsequent measurements agree with Woodcock. For the larger particles ($r>10\mu m$), both (56) and (64) were valid.

Pioneering work on the effects of droplets on the profiles of the means and fluxes for temperature and humidity has been done using a surface layer first-order closure model developed specifically for this application (Ling and Kao, 1976; Ling et al., 1978; Ling et al., 1980). The budget equations were non-dimensionalized using wave height, wind speed, and air-sea temperature and humidity differences and solved for equilibrium conditions (zero time derivatives). The earlier work use only a single, fixed droplet size but the later papers allowed 5 droplet sizes from (5, 20, 40, 70, and 150 μm radius). The droplets were assumed to be pure water so (44a) was not used and the $t'n'$ covariance term was neglected. The surface source function, based on laboratory measurements, was assumed to have a wind speed independent shape and was scaled relative to the second size bin as

$$\bar{S}_{n1}(r_2)*\Delta r_2 = 1.2*10^{-4}\ \bar{u}_{10}^{2} \qquad ;(\#/cm^2/s) \qquad (66)$$

where $r_2=20\mu m$ and $\Delta r_2=20$ μm. The constant $1.2*10^{-4}$ was obtained empirically by finding a value that a gave reasonable results for the predicted temperature and droplet concentration fields. This appears to be about two orders of magnitude greater than the source strength described in Section 2.3, but given the uncertainty in definitions and the manner in which the surface boundary conditions are applied, the significance of this is not clear. Under force 6 winds, Ling et al. (1980) found the major contributions to the moisture flux due to evaporation at a height corresponding to two waveheights to come from droplets in the 20μm to 100 μm radius range. Substantial numbers of very large droplets were 'observed' up to three waveheights and droplets carried almost all of the total water flux below this height (which would be about 10 m at this wind speed). The latent heat flux was a staggering 700 W/m^2 under conditions where the relative humidity was about 70% at a height of 90 m. Unfortunately, this paper does not show

profiles of the fluxes of sensible heat, water vapor or liquid water. Nonetheless, the implication that droplets are important to the surface energy budget comes through loud and clear.

Stramska (1987) has developed a K-theory model to study sea salt aerosol profiles that falls somewhere between the Burk and Ling models in philosophy. As did Burk, Stramska used the surface source model for particles smaller than 15 μm radius from Monahan et al. (1982) and assumed that these particles are in an evaporative equilibrium state. However, the evaporation necessary to maintain this equilibrium is allowed to feedback onto the moisture and temperature profiles. As it turns out, these particles produce a negligible effect on the mean scalar profiles (this is consistent with conclusions of Ling et al., 1980). The effects of larger droplets at high wind speeds (20 m/s) were examined by introducing an ad hoc droplet profile based on near surface data and an assumed decrease in the vertical based on (56). An evaporation equation similar to (24) was used assuming the droplets were pure water. This led to an increase in temperature of about 2 K and an increase in humidity of about 5%. Stramska did not assume dynamic equilibrium but started with an initial profile and integrated the budget equations in time. This permitted a study of the equilibrium response time of the aerosols as a function of size. The results were very similar to that of Fairall et al. (1983) with 10 μm radius particles requiring a few hours to reach dynamic equilibrium. The larger the particle, the shorter the response time because the removal process (gravitational fallout) increases with size.

6.3 The HEXIST experiment

In this section we will be discussing a recent experiment in the air-sea interaction simulation tunnel at IMST near Marseille, France. There is a long history of work in simulation tunnels (Lai and Shemdin, 1974; Wang and Street, 1978; Wu, 1979; Koga and Toba, 1981) which we will not discuss. We will focus on the HEXIST experiment because it was specifically designed to deal with the topic of interest here. The most significant results to come out of the HEXIST experiment so far are the modeling results presented in the next section. First, we will describe the experiment and describe some preliminary scalar profile results.

The IMST tunnel (Coantic et al., 1981) has a test section of 40 m length with the lower part filled with water to a depth of approximately 1.5 m (Fig. 3). Measurements were made at about 25 m from the tunnel inlet. At this fetch, the constant flux region is about 40 cm deep and wave reflections are minimal. Two series of measurements were made (Mestayer et al., 1987). First, droplets were measured under a variety of conditions with two Particle Measurement Systems (PMS) optical particle spectrometers (model CSASP-100HV, 0.5 to 15 μm radius; OAP-220, 10 to 150 μm radius). Then, the particle systems were removed and the measurements were repeated with a suite of mean and flux measurements systems. While the tunnel is capable of producing whitecaps by wind generated breakers or a single breaker produced by a programable wave generator, the major part of the study concentrated on droplets produced by a continuously simulated whitecap at several different fetchs, wind speeds, and humidities. This whitecap was produced by a spray bubbler constructed of conventional sintered porous ceramic used to aerate tropical fishtanks. The spray bubbler produced a continuous and reproducible whitecap of approximately one square meter corresponding to an upwind whitecap fraction of roughly 2% (the equivalent of a 13 m/s oceanic wind speed). This allowed us to study the impact of droplets simply by comparing measurements of meteorological variables with and without the spray bubbler turned on. The

transport of droplets was studied by maintaining the tunnel at very high relative humidity (i.e., non-evaporating conditions).

Sample droplet spectral produced by the spray bubbler are shown in Fig. 4. These droplet spectra are quite similar to oceanic data (de Leeuw, 1986). Suprisingly, the evaporation of the droplets had only a modest effect on the profiles of temperature and humidity (Fig. 5). However, sample profiles of liquid water and evaporation rate are significant (Fig. 6). The liquid water drops off approximately exponentially with height. This profile implies the evaporative equivalent of an 80 W/m^2 upward turbulent latent heat flux of droplets which is partially canceled by a -50 W/m^2 flux due to the mean fall velocity of 20 cm/s for 40 μm radius droplets. The evaporation rates shown in Fig. 6b are equivalent to very substantial vapor flux divergences. The final word on this aspect of the HEXIST experiment must await the processing of the scalar flux data.

6.4 Lagrangian Model

The Lagrangian model developed by Edson (1987) as part of HEXIST attempts to simulate the turbulent transport of evaporating jet drops with the surface layer. Droplets are created above the simulated whitecap region in numbers determined by the surface source function. As each droplet is carried down the tunnel by the mean wind, its path is followed as it reacts to turbulent fluctuations in the vertical wind. Under non-saturated conditions, the particle is allowed to change size by evaporation. At fixed locations downwind of the source (chosen to coincide with locations of the measurements), particle concentration profiles can be computed by counting the number of particles of a given size that pass through a given height interval.

The droplet trajectories are generated using an approach similar to the Markov chain simulations used by Reid (1979), Legg and Raupach (1982), and Ley and Thomson (1983) to successfully model dispersion of fluid particles within the surface layer. The Markov chain is a finite difference form of the Langevin equation; the Langevin equation being given by

$$\frac{dw}{dt} = -\frac{w}{\tau} + \zeta(t) \qquad (67)$$

where w is the particle's vertical velocity, τ is a time scale for the motion, and $\zeta(t)$ is a random forcing function due to turbulence.

The above authors assume that the motion of the particles is passive, i.e., they assume that the particles are of such size that they follow the turbulent motion of the atmosphere exactly. With this assumption, the time scale in (67) is the Lagrangian integral time scale, and the random forcing function is derived observing the constraints that

$$\overline{w'(t)} = 0 \qquad (68a)$$

and

$$\overline{(w'^2)}^{1/2} = \sigma_w \qquad (68b)$$

where σ_w is the standard deviation of the atmospheric vertical velocities.

This is not the case for the range of particles associated with jet drops (~10-100μm), so that gravitational and inertial effects must be included in order to realistically simulate their trajectories. This is accomplished by assuming that the particle's vertical velocity is composed of a mean fall

velocity plus a velocity fluctuation

$$w_p(t) = -\bar{w}_s + w_p'(t) \tag{69}$$

where the fall velocity is determined from (19) for particles of radii smaller than 30 μm, and from

$$\bar{w}_s = \left(\left(\frac{4\upsilon}{3r}\right)^2 + \frac{16gr}{27}\rho_p/\rho\right)^{1/2} - \frac{4\upsilon}{3r} \tag{70}$$

for particles of radii 30-100 μm. The particle velocity statistics are modeled such that

$$\overline{w_p'(t)}_z = 0 \tag{71a}$$

and

$$\overline{(w_p'^2)}_z^{1/2} = \sigma_p = \eta\sigma_w \tag{71b}$$

where σ_p is the standard deviations of the vertical velocity of the particle, the overbar denotes an ensemble average at height z, and we assume that the turbulence in the tunnel is homogeneous (i.e., $d\sigma_w/dz = 0$). The parameter η^2 is the ratio of the particle and atmospheric variances, and is derived by integrating the ratio of their respective velocity spectra. Its value is always less than one due to inertial effects, so that its function is to insure the conservation of energy.

The particle's vertical velocity is then defined using the appropriate finite difference form of the Langevin equation

$$w_p(t+\Delta t) = (1 - \Delta t/\tau_p)w_p(t) + \mu(t+\Delta t) \tag{72}$$

where τ_p is now the particle integral time scale, and $\mu(t+\Delta t)$ is the random forcing function, which by definition is uncorrelated with $w_p(t)$. As with the Lagrangian integral time scale, we define the particle time scale as

$$\tau_p = \int_0^\infty R_p(t)\, dt \,. \tag{73}$$

where R_p is the particle autocorrelation function. The autocorrelation function used in our formulation is similar to that proposed by Meek and Jones (1973). This function is essentially that derived by Hinze (1975), except that they attempt to account for the effects of nonzero free-fall velocity by deriving the function from a nonzero velocity spectrum. Their function shows that increasing fall velocity tends to decrease correlation, while inertial effects tend to offset this effect by "damping" vertical motion, thereby causing the particle to remain in a more correlated region of space. The relative importance of either effect is dependent on the particle's size.

The initial formulation of the model does not include fluctuations in the streamwise velocity for simplicity ($w_p'u_p' = 0$). With this in mind, the necessary form of the random forcing function is found by taking the mean and then variance of both sides of (72) (remembering that $\mu(t+\Delta t)$ and w(t) are uncorrelated), and then solving for μ. If we consider only those terms of first order Δt, this results in (Thomson, 1984)

$$\bar{\mu} = -\frac{\Delta t}{\tau_p}\bar{w}_s \tag{74a}$$

$$\overline{\mu^2} = \frac{2\Delta t}{\tau_p}\overline{w_p'^2} \tag{74b}$$

so that the above constraints are satisfied by letting

$$\mu = \Gamma\sigma_p\left(\frac{2\Delta t}{\tau_p}\right)^{1/2} - \frac{\Delta t}{\tau_p}\bar{w}_s \tag{75}$$

where Γ is a random number with unit variance, zero mean and Gaussian distribution generated using a technique based on the central limit theory. Here it should be noted that the assumption of a Gaussian distribution is probably an oversimplification. Again, however, in an effort to keep this initial formulation of the model as simple as possible, we will assume that all other moments of $\mu(t+\Delta t)$ are zero. The equation for the particle's vertical velocity can then be written

$$w_p(t+\Delta t) = (1 - \Delta t/\tau_p)w_p(t) + \Gamma\sigma_p\left(\frac{2\Delta t}{\tau_p}\right)^{1/2} - \frac{\Delta t}{\tau_p}\bar{w}_s \ . \tag{76}$$

The droplets are released at an ejection height described above, and then advected along (see Fig. 7) using (76) and

$$w_p(0) = \Gamma\sigma_p - \bar{w}_s \tag{77a}$$

$$z(t+\Delta t) = z(t) + w_p(t+\Delta t)\Delta t \tag{77b}$$

$$x(t+\Delta t) = x(t) + \bar{U}(z(t+\Delta t)\Delta t \tag{77c}$$

where $\bar{U}(z)$ is the horizontal wind speed at height z taken from a logarithmic profile generated from tunnel observations. The height of the viscous sublayer is used as a lower limit, below which the particles are "absorbed" by the water surface. The sublayer thickness is defined as $\nu/\kappa u_*$, where ν is the kinematic viscosity of air, κ is von Karman's constant and u_* is the friction velocity.

The effects of evaporation are modeled using diagnostic equations for the particle's radius (see (28)) and surface temperature, in conjunction with diabatic profiles of temperature and specific humidity (e.g., see Businger, 1973). The droplet surface temperature is derived using an equation from Pruppacher and Klett (1978), which includes the effects of evaporative cooling and conductive heat flux from air to drop. As stated above, this temperature is found to quickly reach the equilibrium value resulting from the two effects, so that the droplet is essentially at the wet-bulb temperature for most of its transit time.

By keeping track of the particle's position and radius, the dynamics of a shrinking particle are simulated. As expected, the equation of the droplet's motion as its radius shrinks to zero reduces to the Langevin equation in discrete form used implicitly by Reid (1979), Legg and Raupach (1982), and Ley and Thomson (1983). Vertical profiles of particle volume spectra, v(r), are then generated (Fig. 8 and 9) at the desired heights and distances downwind of the source (see Edson, 1987). The source function is found by comparing the non-evaporating spectra with their equivalent measured spectra, and adjusting the source function until a reasonable fit is obtained. Once obtained, the

source function is fixed so that true comparisons between the modeled and measured data may be made. The bubble spectra (for the two bubbler rates used in the experiment) are shown in Figure 10. Notice in Figs. 8 and 9 that the greater fetch causes the droplet concentrations to become more well-mixed by the turbulence because of the greater time the mixing process has had to operate. The effects of evaporation are difficult to judge from these figures because they are expressed in terms of spectra. Depending on the slope of the spectrum, evaporation can cause an increase or decrease in concentration at a specific radius. This can be seen by examining (44b).

6.5 The HEXMAX experiment

One major aspect of the HEXOS program has been the planning and execution of a comprehensive field experiment to investigate the various issues concerning the stress and heat transfer from the ocean in strong winds. This experiment has been given the designation HEXMAX. Katsaros et al. (1987) have described the plan for the experiment and the participants (24 groups from 8 countries). HEXMAX was held on the Meetpost Noordwijk (MPN), which is an offshore platform on the Dutch coast in the North Sea, between October 15 and November 21, 1987. Besides a wide variety of meteorological and oceanographic measurements from the platform, a research aircraft, a research ship and several moored masts, buoys, and shore-based measurements were also involved.

The platform provided continuous measurements of high speed (i.e., suitable for flux calculations) and mean meteorological data from two locations. The primary location was a boom which extended 16m horizontally away from the platform on the western face (the predominant wind direction for strong winds at the site). The boom was festooned with four suites of instruments such as sonic anemometers, lyman-α humidiometers, microthermal temperature sensors, fast response propeller anemometers, hot-wire anemometers, cooled mirror dew point temperature sensors, etc (Fig. 11). A very long boom was used for these instruments to reduce the effects of flow distortion by the platform structure. The boom was normally operated at 7m above the water and was raised several times a day (sometimes hourly) for calibrations and servicing of sensors. A second meteorological instrument suite was mounted on a mast on the western edge of the platform, extending 7 m vertically above the helodeck for a total height above the ocean of 25 m. This site was deliberately located in a region of substantial flow distortion in order to evaluate relative sensitivity of the various flux estimation techniques to distortion by a platform or ship. Sea spray droplets, aerosol spectra, whitecaps, wave spectra, currents, water temperature, and radiative fluxes were measured at other points on the platform. Several remote sensing experiments were also done on the platform including lidar and long path scintillometers.

The HEXMAX experiment was quite successful. For once, nature cooperated by providing many days of favorable wind directions with wind speeds in excess of 12 m/s. Several periods with winds in excess of 20 m/s were experienced. The maximum half-hour average wind during the experiment was 31 m/s. Because so many research groups are involved and the measurement tasks were so highly compartmentalized, the analysis is expected to take years. The first step in this process is the compilation of an official time series of the mean properties (wind speed, humidity, air temperature, water temperature, etc.). The mean data from a variety of sensors will be compared and the most credible will be used to construct the official data set. This approach is being taken to avoid future confusion and the possibility, for example, of one eddy

correlation measurement producing three different drag coefficients depending on which water temperature measurement is used. The next step will be the establishment of turbulence standards (variances, covariances, spectra) at selected periods from the most carefully calibrated fast response sensors. This will provide an 'in situ' fluctuation calibration standard for all investigators.

Because the analysis process for HEXMAX is just beginning, it is not possible to give any definitive results at this time. However, we can give some preliminary results that illustrate a few points and demonstrate the quality of the data. In Figure 12 we have plotted three comparisons of simultaneous stress estimates (expressed as the friction velocity) using the eddy covariance method and the inertial-dissipation method from measurements made on the boom (7 m height) and the mast (25 m height). The upper panel shows that the two methods agree quite well, but with some scatter on the order of 10%. By comparing the boom with the mast, we are able to conclude that most of the scatter is due to the covariance method. Notice that the dissipation-dissipation estimates have almost no scatter but the covariance-covariance estimates have considerable scatter. This is consistent with the greater intermittency associated with covariances as opposed to variances. It also proves that the dissipation method is virtually uninfluenced by flow distortion, since the mast data are taken in a region where the average wind vector has a 10 degree upward tilt induced by flow over the platform.

ACKNOWLEDGEMENTS

This work is supported by the Office of Naval Research (contract N00014-85-K-0250). The authors wish to acknowledge collaboration with Soren Larsen of RISO National Laboratory in Roskilde, Denmark; Patrice Mestayer of IMST in Marseille, France; and Ken Davidson and Don Spiel of NPS in Monterey, California, USA.

REFERENCES

Anderson, R.J. and S.D. Smith, 1981: Evaporation coefficient for the sea surface from eddy-flux measurements. J. Geophys. Res., 86, 449-456.

Blanc, T.V., 1985: Variation of bulk-derived surface flux, stability, and roughness results due to the use of different transfer coefficient schemes. J. Phys. Ocean., 15, 650-669.

Blanchard, D.C. and A.H. Woodcock, 1957: Bubble formation and modification in the sea and its meteorological significance, Tellus, 9, 145-158.

Blanchard, D.C., 1971: Whitecaps at sea. J. Atmos. Sci., 28, 645.

Blanchard, D.C., 1975: Bubble scavenging and the water-to-air transfer of organic material in the sea. Adv. in Chem., 145, American Chemical Society, Washington, DC.

Businger, J.A., 1973: Turbulent transfer in the atmospheric surface layer. Workshop on Micrometeorology, Amer. Meteor. Soc.,67-100.

Businger, J.A., 1982: Equations and concepts, in Atmospheric Turbulence and Air Pollution Modeling, edited by F.T.M. Nieuwstadt and H. van Dop, D. Reidel, Hingham, Mass.

Cipriano, R.J. and D.C. Blanchard, 1981: Bubble and aerosol spectra produced by a laboratory breaking wave. J. Geophys. Res., 86, 8085-8092.

Cipriano, R.J., D.C. Blanchard, A.W. Hogan, and G.G. Lala, 1983: On the production of Aitken nuclei from breaking waves and their role in the atmosphere. J. Atmos. Sci., 40, 469-479.

Cipriano, R.J., E.C. Monahan, P.A. Bowyer, and D.K. Woolf, 1987: Marine condensation nucleus generation inferred from whitecap simulation tank results. J. Geophys. Res., to appear.

Clark, Terry L., 1973: Numerical modeling of the dynamics and microphysics of warm cumulus convection. J. Atmos. Sci., 30, 857-878.

Clark, Terry L., 1974: A study in cloud phase parameterization using the gamma distribution. J. Atmos. Sci., 31, 142-155.

Clark, Terry L. and W.E. Hall, 1979: A numerical experiment on stochastic condensation theory. J. Atmos. Sci., 36, 470-483.

Coantic, M., 1980: Mass transfer across the ocean-air interface: small scale hydrodynamics and aerodynamic mechanisms. Phys. Chem. Hydro., 1, 249-279.

Coantic, M., A. Ramamonjiarisoa, P. Mestayer, F. Resch, and A. Favre, 1981: Wind-water tunnel simulation of small-scale ocean-atmosphere interactions. J. Geophys. Res., 86, 6607-6626.

de Leeuw, G. 1986: Vertical profiles of giant particles close above the sea surface. Tellus, 38B, 51-61.

Edson. J.B., 1987: Lagrangian model simulations of the turbulent transport and evaporation of spray droplets in a wind-water tunnel. M.S. thesis, Department of Meteorology, Pennsylvania State University, University Park, PA, 16802, USA.

Fairall, C.W., K.L. Davidson, and G.E. Schacher, 1983: An analysis of the surface production of sea-salt aerosol. Tellus, 35B, 31-39.

Fairall, C.W., 1984: Interpretation of eddy-correlation measurements of particulate deposition and aerosol flux. Atmos. Environ., 18, 1329-1337.

Fairall, C.W. and S.E. Larsen, 1984: Dry deposition, surface production and dynamics of aerosols in the marine boundary layer. Atmos. Environ., 18, 69-77.

Fairall, C.W. and S.E. Larsen, 1986: Inertial dissipation methods and turbulent fluxes at the air ocean interface. Bound.-Layer Meteorol., 34, 287-301.

Fitzgerald, J.W., 1975: Approximation formulas for the equilibrium size of an aerosol particle as a function of its dry size and composition and the ambient relative humidity. J. Appl. Met., 14, 1044-1049.

Francey, R.J. and J.R. Garratt, 1989: Is an observed wind-speed dependence of AMTEX '75 heat transfer coefficients real? Bound.-Layer Meteorol., 16, 249-260.

Friehe, C.A. and K.F. Schmitt, 1976: Parameterization of air-sea interface fluxes of sensible heat and moisture by the bulk aerodynamic formulas. J. Phys. Ocean., 6, 801-809.

Fuchs, N.A., 1959: Evaporation and Droplet Growth in Gaseous Media, Pergamon Press.

Garratt, J.R. and B.B. Hicks, 1973: Momentum, heat and water vapor transfer to and from natural and artificial surfaces. Quart. J. Royal Meteor. Soc., 99, 680-687.

Hall, C.D., 1975: The simulation of particle motion in the atmosphere by a numerical random-walk model. Quart. J. Roy. Meteorol. Soc., 101, 235-244.

Hasse, L., 1980: Gas exchange across the air-sea interface. Tellus, 32, 470-481.

Hicks, B.B., D.D. Baldocchi, R.P. Hosker, B.A. Hutchison, D.R. Matt, R.T. McMillen, and L.C. Satterfield, 1985: On the use of monitored air concentrations to infer dry deposition. NOAA Tech. Memor. Air resources Lab. ERL ARL-141, Silver Spring, MD, 65 pp.

Hinze, J.O., 1975: Turbulence. McGraw-Hill, New York, 460-467.

Joffre, S.M., 1982: Momentum and heat transfers in the surface layer over a frozen sea. Bound.-Layer Meteorol., 24, 211-229.

Katsaros, K.B., S.D. Smith and W.A. Oost, 1987: HEXOS-humidity exchange over the sea. A program for research on water vapor and droplet fluxes from sea to air at moderate and high wind speeds. Bull. Am. Met. Soc., 68, 466-476.

Kientzler, C.F., A.B. Arons, D.C. Blanchard, and A.H. Woodcock, 1954: Photographic investigation of the projection of droplets by bubbles bursting at a water surface. Tellus, 6, 1-7.

Koga M. and Y. Toba, 1981: Droplet distribution and dispersion processes on breaking wind waves. Sci. Rep. Tohoku University Ser. 5, Geophysics, 28, 1-25.

Lai R.J. and O.H. Shemdin, 1974: Laboratory study of the generation of the spray over water. J. Geophys. Res., 70, 3055-3063.

Legg, B.J., and M.R. Raupach, 1982: Markov-chain simulation of particles in inhomogeneous flows: The mean drift velocity induced by a gradient in Eulerian velocity variance. Bound.-Layer Meteorol., 24, 3-13.

LeMone, M.A. and W.T. Pennell, 1976: The relationship of trade wind cumulus distribution to subcloud layer fluxes and structure. Mon. Wea. Rev., 104, 524-539.

Lewellen, W.S., D.A. Oliver, M.E. Teske, H. Segur and O. Cote, 1977: Status report on low-level atmospheric turbulence model for marine environments. ARAP Tech. Report No. 320, Box 2229, Princeton, NJ, 54 pp.

Ley, A.J., and D.J. Thomson, 1983: A random walk model of dispersion in the diabatic surface layer. Quart. J. R. Meteorol. Soc., 109, 867-880.

Ling, S.C. and T.W. Kao, 1976: Parameterization of the moisture and heat transfer process over the ocean under whitecap sea states. J. Phys. Oceanogr., 6, 306-315.

Ling, S.C., A. Saad, and T.W. Kao, 1978: Mechanics of multiphase fluxes over the ocean. Turbulent Fluxes through the Sea Surface, Wave Dynamics and Prediction, edited by A. Favre and K. Hasselmann, Plenum, New York, 185-1987.

Ling, S.C., T.W. Kao, M. Asce and A. Saad, 1980: Microdroplets and transport of moisture from the ocean. J. Eng. Mech. Div., 6, 1327-1339.

Meek, C.C., and B.G. Jones, 1973: Studies of the behavior of heavy particles in a turbulent fluid flow. J. Atmos. Sci., 30, 239-244.

Mestayer, P.G., C.W. Fairall, S.E. Larsen, D.E. Spiel, and J.B. Edson, 1987: Turbulent transport and evaporation of droplets generated at an air-water interface. Proceed. 6th Symposium on Turbulent Shear Flows, Toulouse, Fr.

Miller, M.A., 1987: Modeling the production and transport of sea-salt aerosols. M.S. thesis, Department of Meteorology, Pennsylvania State University, University Park, PA, 16802, USA.

Monahan, E.C. and C.R. Zietlow, 1969: Laboratory comparison of fresh water and salt water whitecaps. J. Geophys. Res., 74, 6961-6966.

Monahan, E.C., K.L. Davidson and D.E. Spiel, 1982: Whitecap aerosol productivity deduced from simulation tank measurements. J. Geophys. Res., 87, 8898-8904.

Monahan, E.C., C.W. Fairall, K.L. Davidson, and P.J. Boyle, 1983: Observed inter-relations between 10 m winds, ocean whitecaps and marine aerosols. Quart. J. R. Met. Soc., 109, 379-392.

Monahan, E.C. and G. Mac Niocaill, 1986: Oceanic Whitecaps, D. Reidel, Dordrecht, Holland.

Monahan, E.C., D.E. Spiel, and K.L. Davidson, 1986: A Model of Marine Aerosol Generation via Whitecaps and Wave Disruption. Oceanic Whitecaps and their Role in Air-Sea Exchange Processes, E.C. Monahan and G. Mac Niocaill, Eds., Galway U. Press.

Nicholls, S. and C.J. Readings, 1979: Aircraft observations of the structure of the lower boundary layer over the sea. Quart. J. R. Met. Soc., 105, 785-802.

Preobrazhenskii, L., 1973: Estimation of the content of spray drops in the near-water layer of the atmosphere. Fluid Mech. Sov. Res., 2, 95-100.

Pruppacher, H.R. and J.D. Klett, 1978: Microphysics of Clouds and Precipitation, Reidel, Dordrecht, Holland.

Reid, J. D., 1979: Markov chain simulations of vertical dispersion in the neutral layer for surface and elevated releases. Bound.-Layer Meteorol., 16, 3-22.

Resch, F.J., 1986: Marine liquid aerosol production from bursting of air bubbles. J. Geophys. Res., 91, 1019-1025.

Slinn, W.G.N., L. Hasse, B.B. Hicks, A.W. Hogan, D. Lal, P.S. Liss, K.O. Munnich, G.A. Sehmel, and O. Vittori, 1978: Some aspects of the transfer of atmospheric trace constituents past the air-sea interface. Atmos. Environ., 12, 2055-2087.

Stramska, M., 1986: Vertical profiles of sea-salt aerosol in the atmosphere surface layer: a numerical model. Acta Geophys. Pol., to appear.

Thomson, D.J., 1984: Random walk modeling of diffusion in inhomogeneous turbulence. Quart. J. R. Met. Soc., 110, 1107-1120.

Toba, Y., 1965: On the giant sea-salt particles in the atmosphere. II-Theory of the vertical distribution in the 10-m layer over the ocean. Tellus, 17, 365-382.

Wang, C.S. and R.L. Street, 1978: Transfer across an air-water interface at high-wind speeds. J. Geophys. Res., 83, 2959-2962.

Woodcock, A.H., 1953: Salt nuclei in marine air as a function of altitude and wind force. J. Met., 10, 362-371.

Wu, J., 1974: Evaporation due to spray. J. Geophys. Res., 79, 4107-4109.

Wu, J., 1979: spray in the atmospheric-surface layer: a review and analysis of laboratory and oceanic results. J. Geophys. Res., 84, 1693-1704.

FIGURE CAPTIONS

Figure 1. Droplet source strength, S_{vi}, as a function of droplet radius for the spray bubblers used in the HEXIST experiment. The source is expressed in units of droplet volume (μm^3) per square centimeter of ocean per second per μm radius increment.

Figure 2. Droplet source strength, S_{vi}, as a function of droplet radius for the ocean. A curve is plotted for each mean wind speed (10 m altitude) as indicated on the figure. This source function represents a consensus of various laboratory and field data.

Figure 3. Schematic diagram of the wind-water tunnel setup at IMST for the HEXIST experiment. The droplet measuring (and later the turbulence measuring) probes were mounted on the chariot left of center of the tunnel; the spray bubblers were positioned 5m or 9m upwind of the probes.

Figure 4. Sample droplet volume spectra vs. droplet radius from HEXIST. The stars are the measurements; the line is a self-similar spectral shape that results from a rate of change of droplet radius due to evaporation that is independent of radius.

Figure 5. Sample mean meteorological variable profiles (wind speed, temperature and water vapor density) from HEXIST. The solid line is without spray droplets, the solid circles are with spray droplets.

Figure 6. Sample liquid water content (upper panel) and evaporation rate (lower panel) profile data from HEXIST. These data were taken at a bubbler fetch of 5m with 9 m/s nominal wind speed. In the upper panel, different lines denote different relative humidities: dotted, 100%; dashed, 80%; and dash-dot, 50%. In the lower panel the designations are: dotted, 80%; and dashed, 50%.

Figure 7. Lagrangian model simulation of 50 droplet trajectories for the HEXIST experiment at 9 m/s nominal wind speed. The vertical axis is the droplet height (cm) and the horizontal axis is the droplet distance (cm) downwind of the source. The upper panel is a family of trajectories for a 50 μm radius droplet, the lower panel is for a 10 μm radius droplet. Both are released from 10 cm for comparison.

Figure 8. Droplet volume concentration spectra vs. height profiles for two selected size droplets from HEXIST. The lines denote smoothed fits to measured data, the symbols denote values simulated with the Lagrangian model averaged over five model runs. The bars indicate the standard deviations from the mean values. The conditions for this example are a relative humidity near 100%, nominal wind speed of 9m/s, and initial radius of 15 and 40 μm for the two droplet sizes.
(a) downwind fetch of 5 m.
(b) downwind fetch of 9 m.

Figure 9. As in Figure 8 but for evaporating (nominal relative humidity near 50%) conditions. The initial radii at time of release are again 15 and 40 μm.

Figure 10. HEXIST spray bubbler number density bubble spectra (assumed) vs. bubble radius for two different air flow rates. The bubble spectra is given in number of bubbles per 10 μm increments so that the equivalent droplet increment (as used in the model) is 1 μm. The actual size distribution in $cm^{-3}\mu m^{-1}$ would equal these values divided by 10.

Figure 11. Photograph of the instrument boom deployed on the Dutch platform, MPN, in the North Sea during the HEXMAX experiment.

Figure 12. Comparison of inertial-dissipation and eddy correlation estimates of the friction velocity, u_*, from the HEXMAX experiment. The boom is at a height of 7 m over the ocean while the mast is at a height of 25 m. The boom is extended 16 m horizontally away from the platform and is considered to be relatively free of flow distortion. (a) Inertial dissipation estimates (boom and mast) versus eddy covariance estimate (boom only), (b) inertial-dissipation estimate, boom versus mast, (c) eddy covariance estimate, boom versus mast.

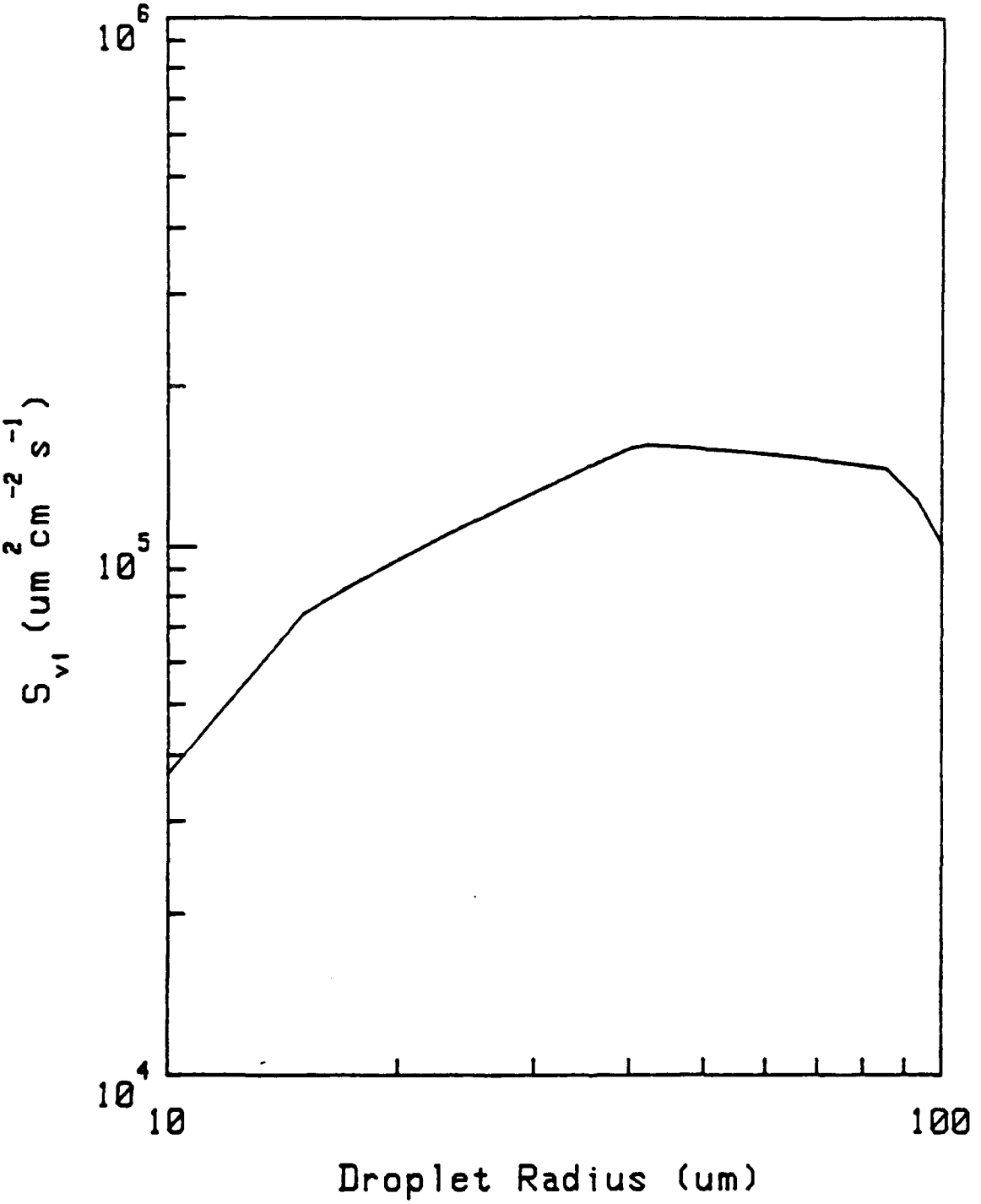

Figure 1. Droplet source strength, S_{vi}, as a function of droplet radius for the spray bubblers used in the HEXIST experiment. The source is expressed in units of droplet volume (μm^3) per square centimeter of foam patch per second per μm radius increment.

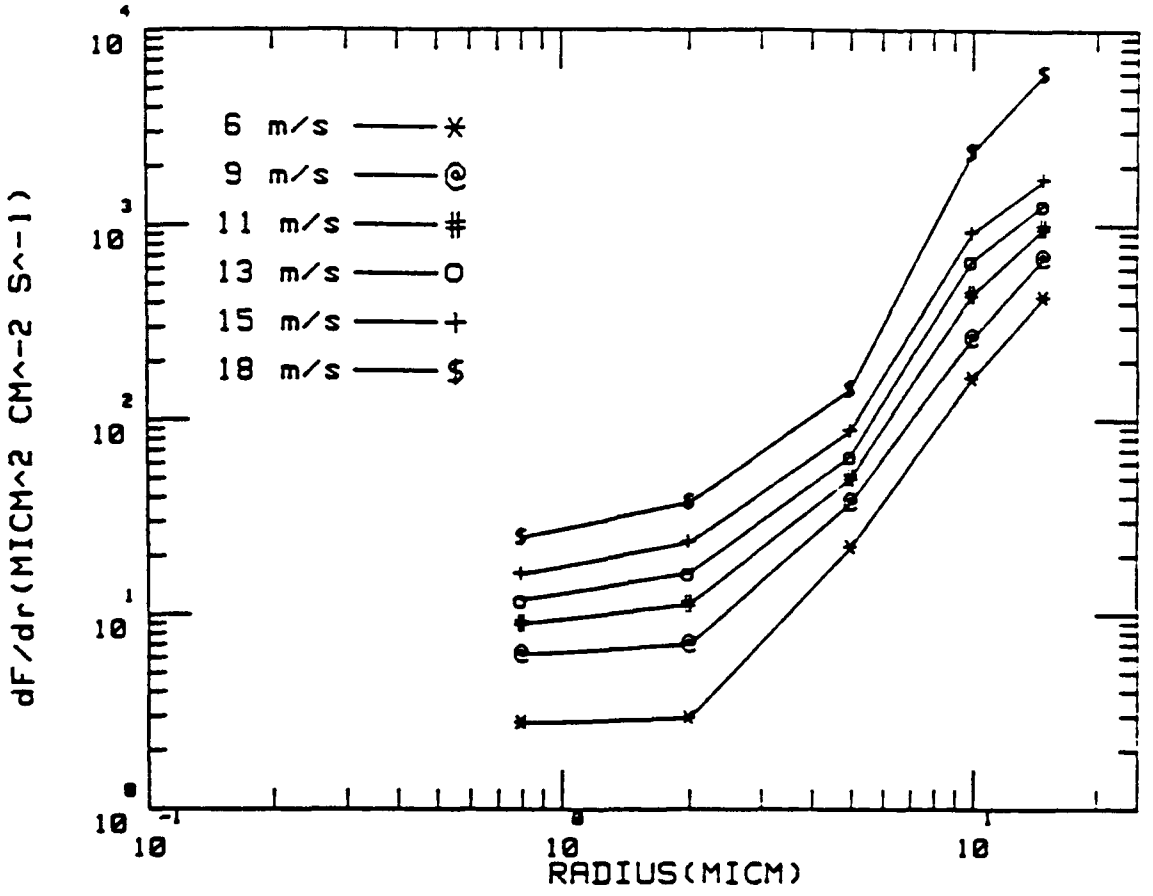

Figure 2. Droplet source strength, S_{vi}, as a function of droplet radius for the ocean. A curve is plotted for each mean wind speed (10 m altitude) as indicated on the figure. This source function represents a consensus of various laboratory and field data.

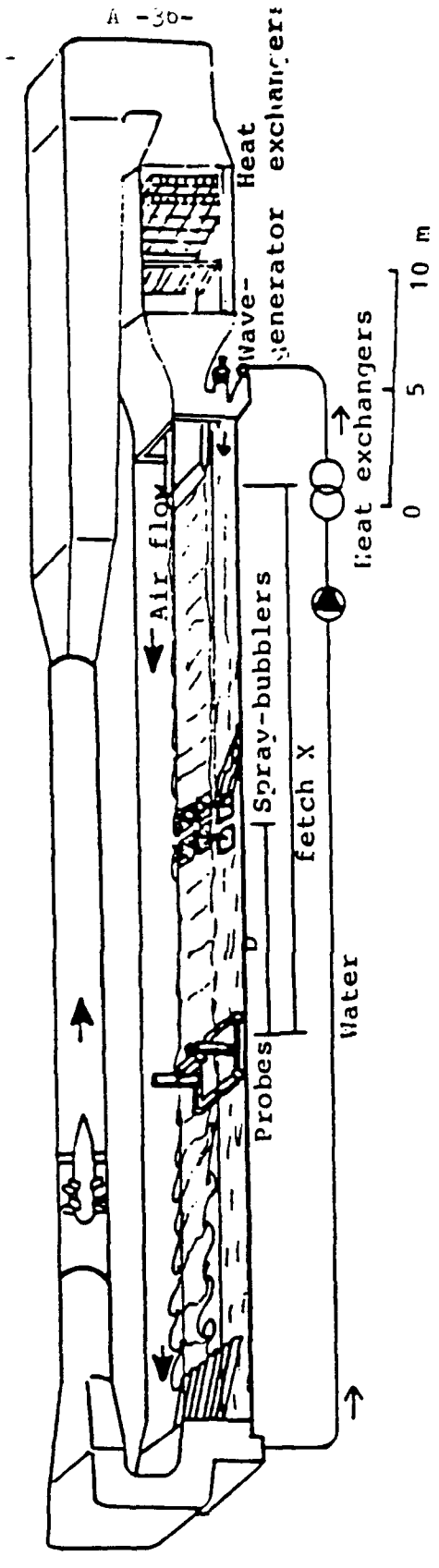

Figure 3. Schematic diagram of the wind-water tunnel setup at IMST for the HEXIST experiment. The droplet measuring (and later the turbulence measuring) probes were mounted on the chariot left of center of the tunnel; the spray bubblers were positioned 5m or 9m upwind of the probes.

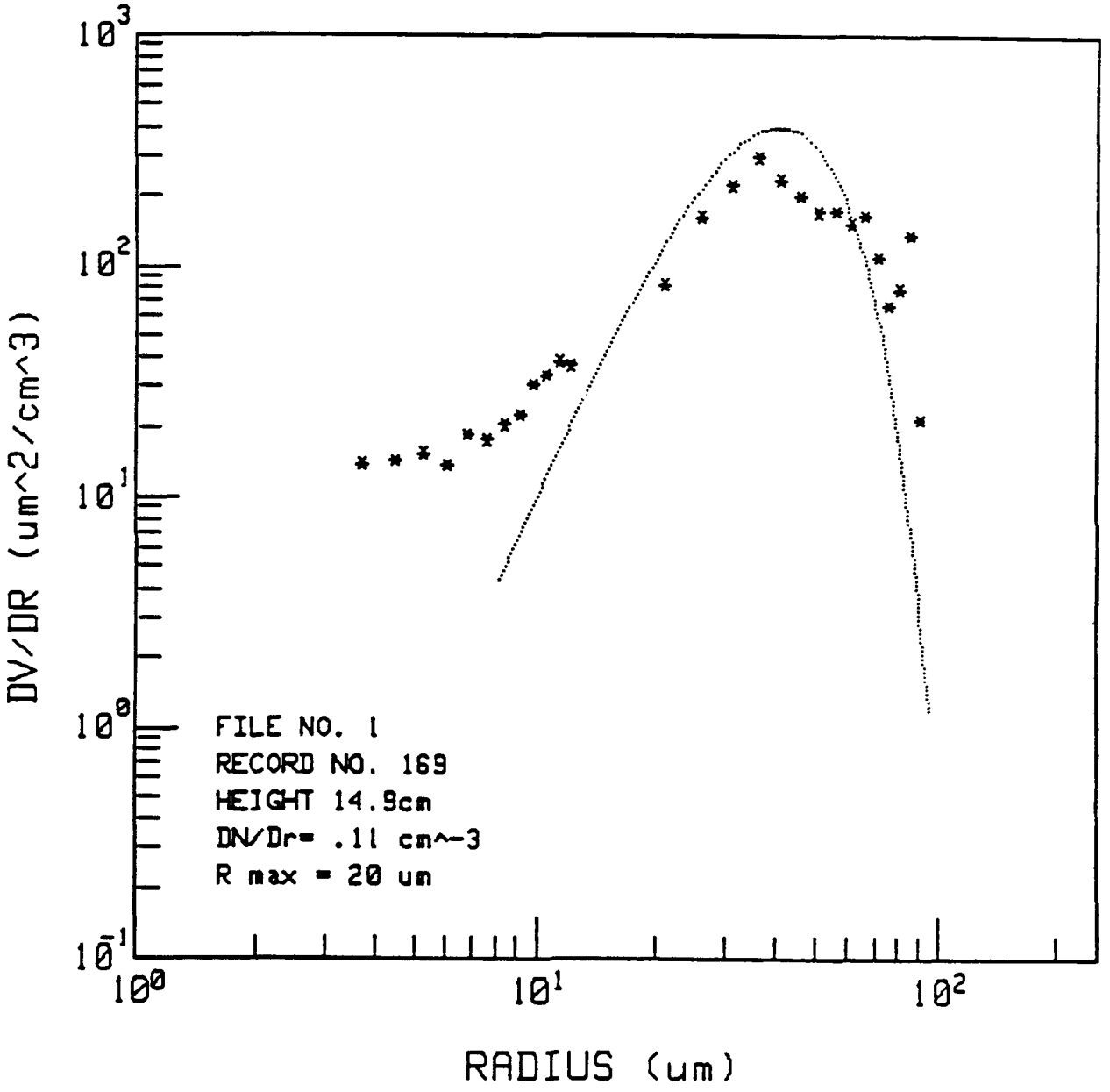

Figure 4. Sample droplet volume spectra vs. droplet radius from HEXIST. The stars are the measurements; the line is a self-similar spectral shape that results from a rate of change of droplet radius due to evaporation that is independent of radius.

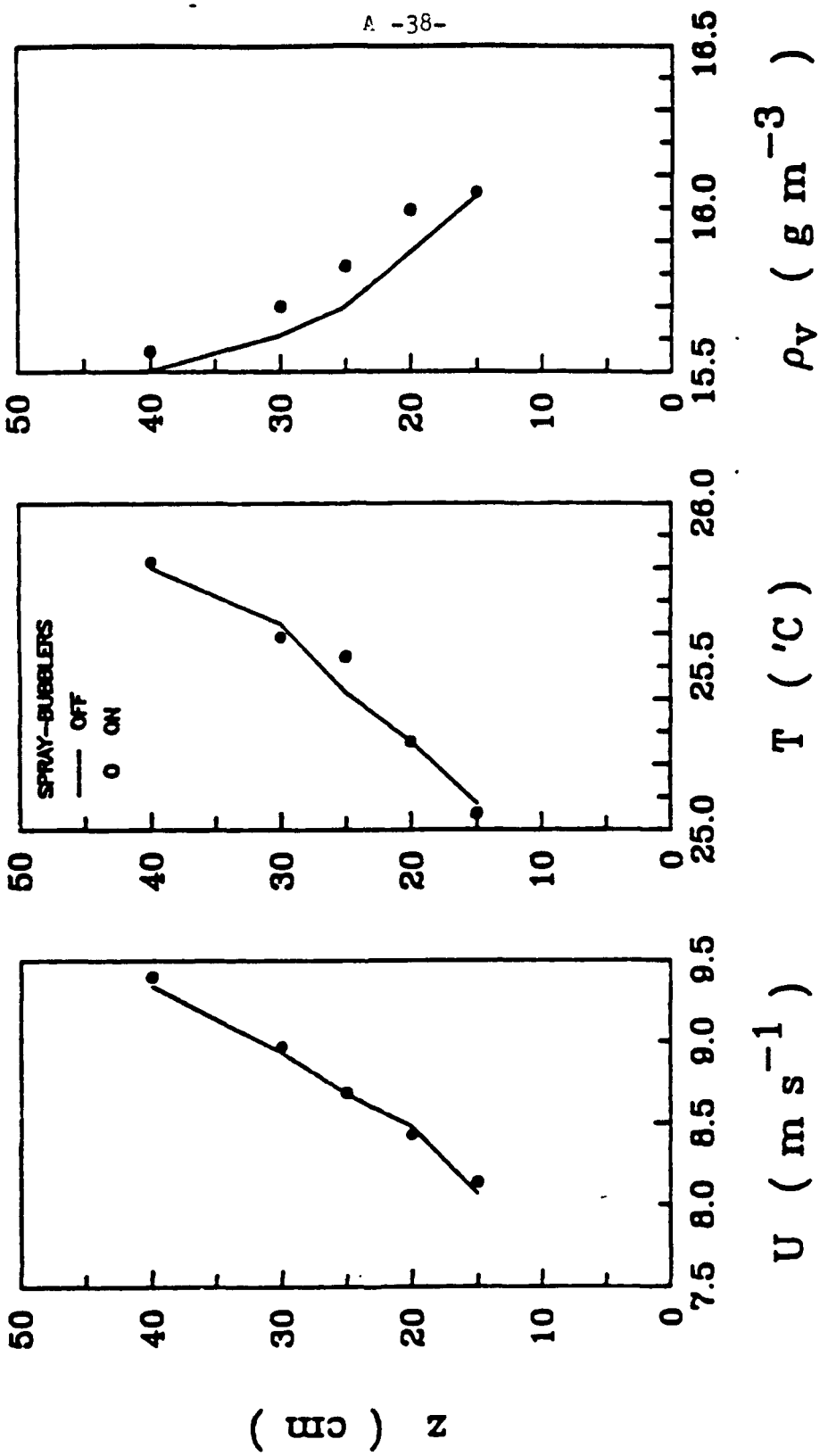

Figure 5. Sample mean meteorological variable profiles (wind speed, temperature and water vapor density) from HEXIST. The solid line is without spray droplets, the solid circles are with spray droplets.

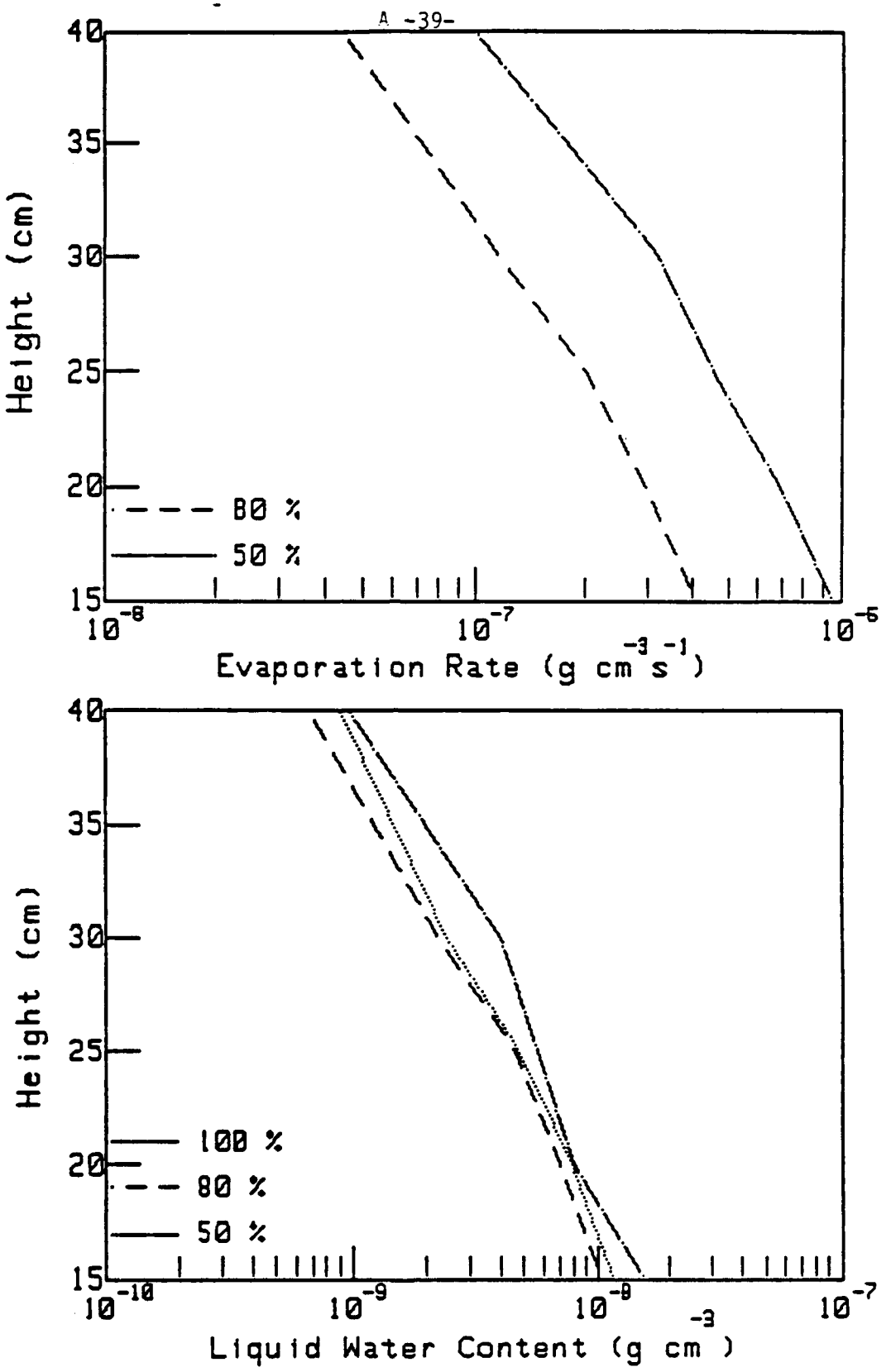

Figure 6. Evaporation rate (upper panel) and sample liquid water content (lower panel) profile data from HEXIST. These data were taken at a bubbler fetch of 5m with 9 m/s nominal wind speed. The different lines denote different relative humidities: dotted, 100%; dashed, 80%; and dash-dot, 50%.

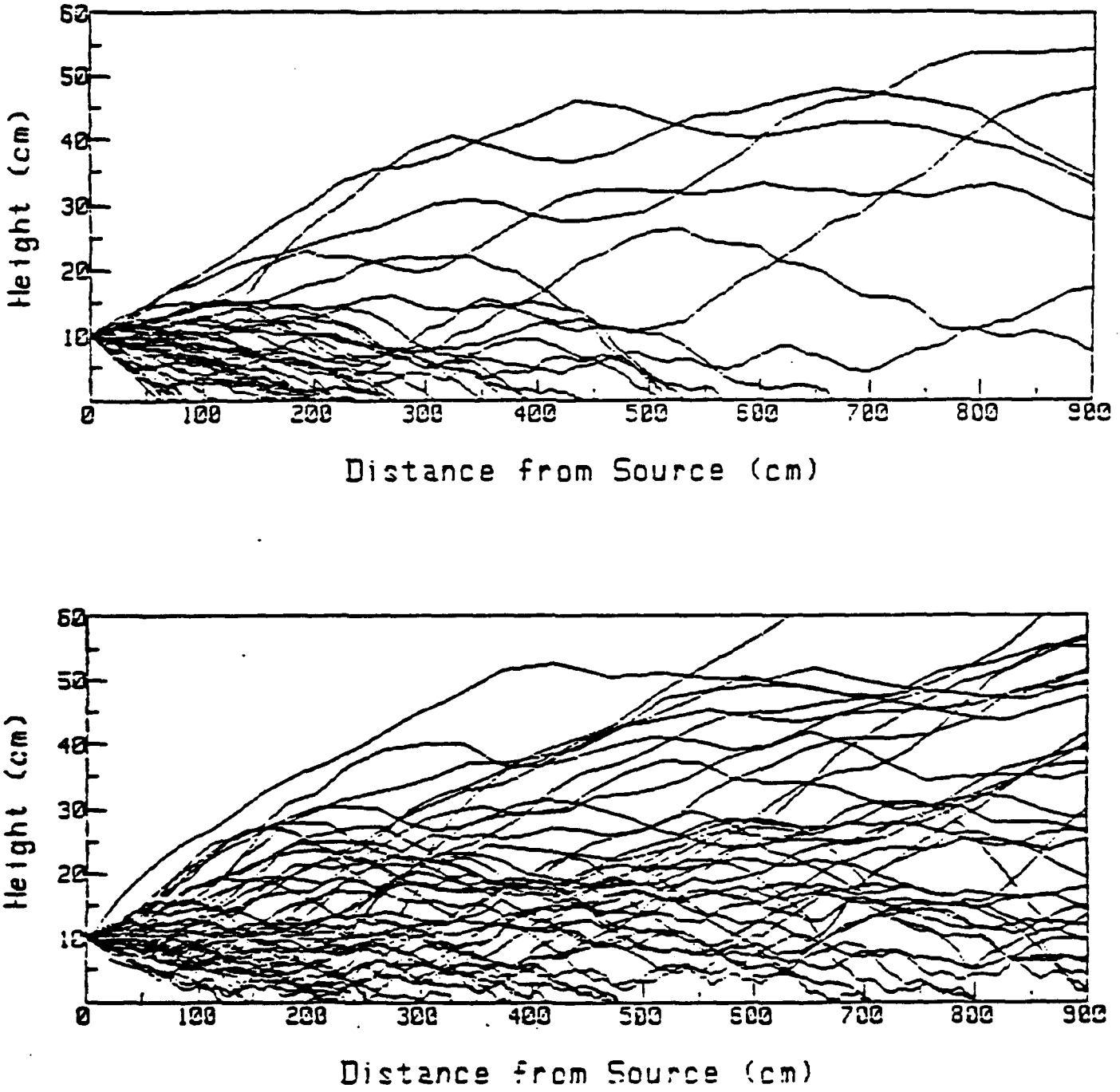

Figure 7. Lagrangian model simulation of 50 droplet trajectories for the HEXIST experiment at 9 m/s nominal wind speed. The vertical axis is the droplet height (cm) and the horizontal axis is the droplet distance (cm) downwind of the source. The upper panel is a family of trajectories for a 50 μm radius droplet, the lower panel is for a 10 μm radius droplet. Both are released from 10 cm for comparison.

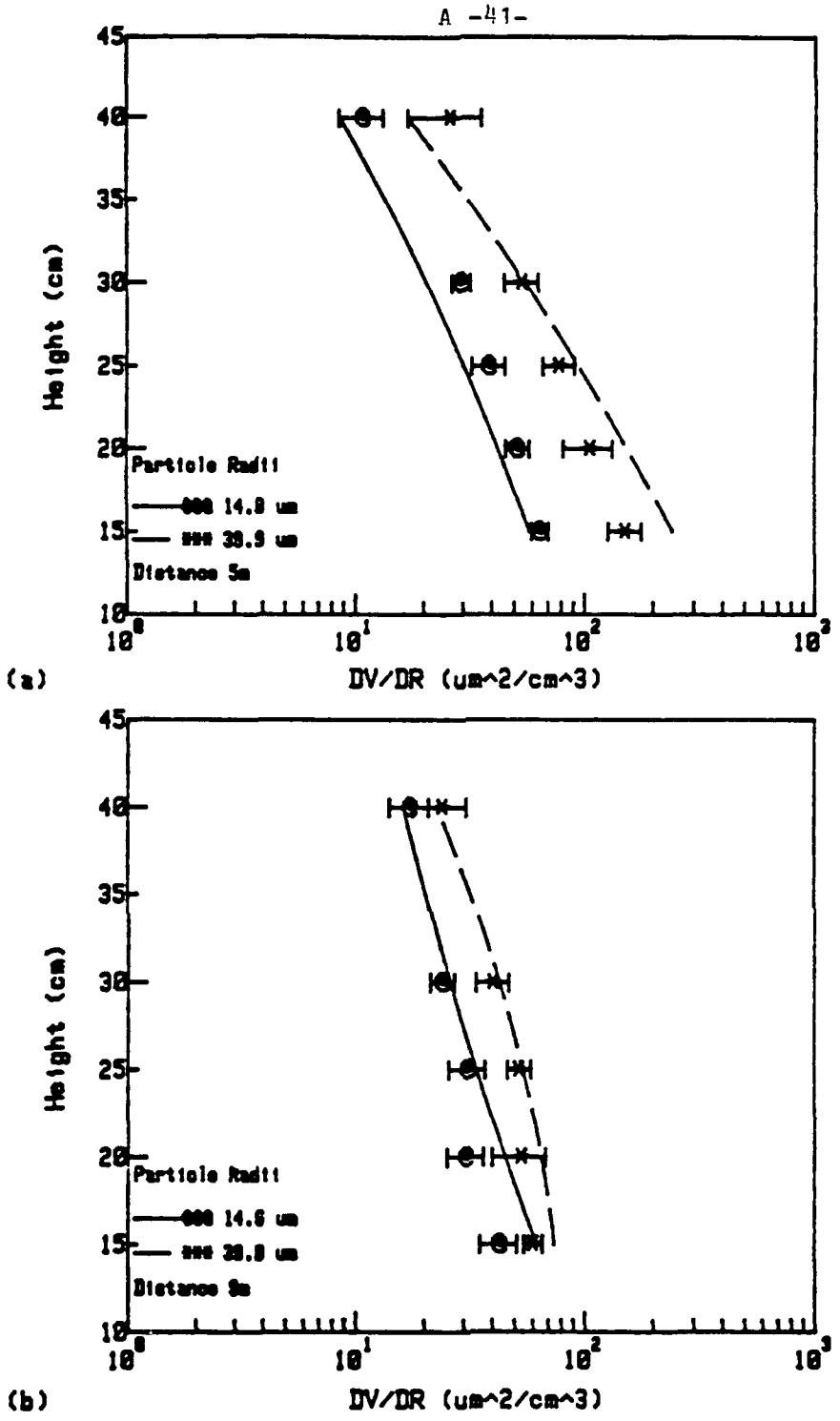

Figure 8. Droplet volume concentration spectra vs. height profiles for two selected size droplets from HEXIST. The lines denote smoothed fits to measured data, the symbols denote values simulated with the Lagrangian model averaged over five model runs. The bars indicate the standard deviations from the mean values. The conditions for this example are a relative humidity near 100%, nominal wind speed of 9m/s, and initial radius of 15 and 40 μm for the two droplet sizes.
(a) downwind fetch of 5 m.
(b) downwind fetch of 9 m.

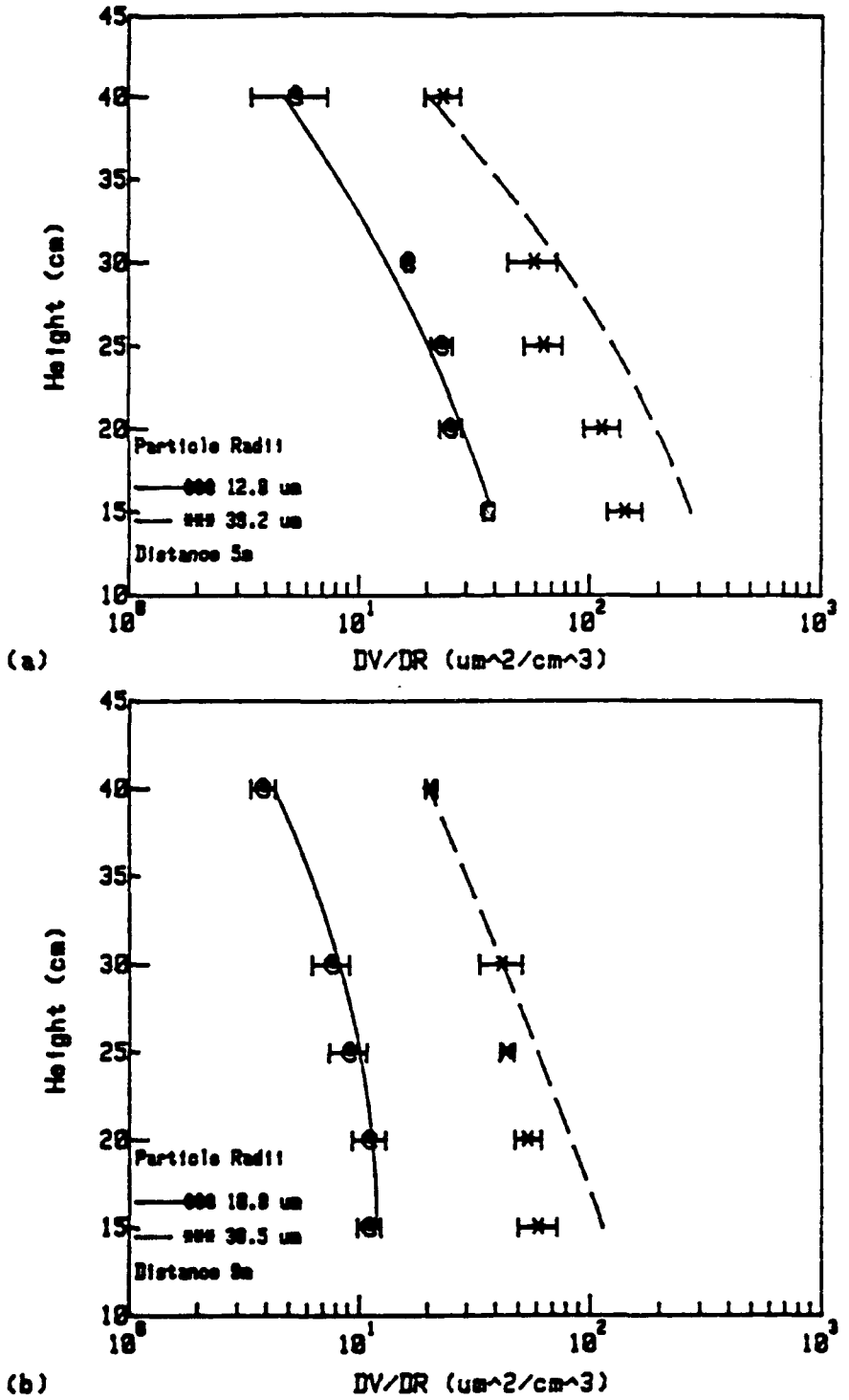

Figure 9. As in Figure 8 but for evaporating (nominal relative humidity near 50%) conditions. The initial radii at time of release are again 15 and 40 μm.

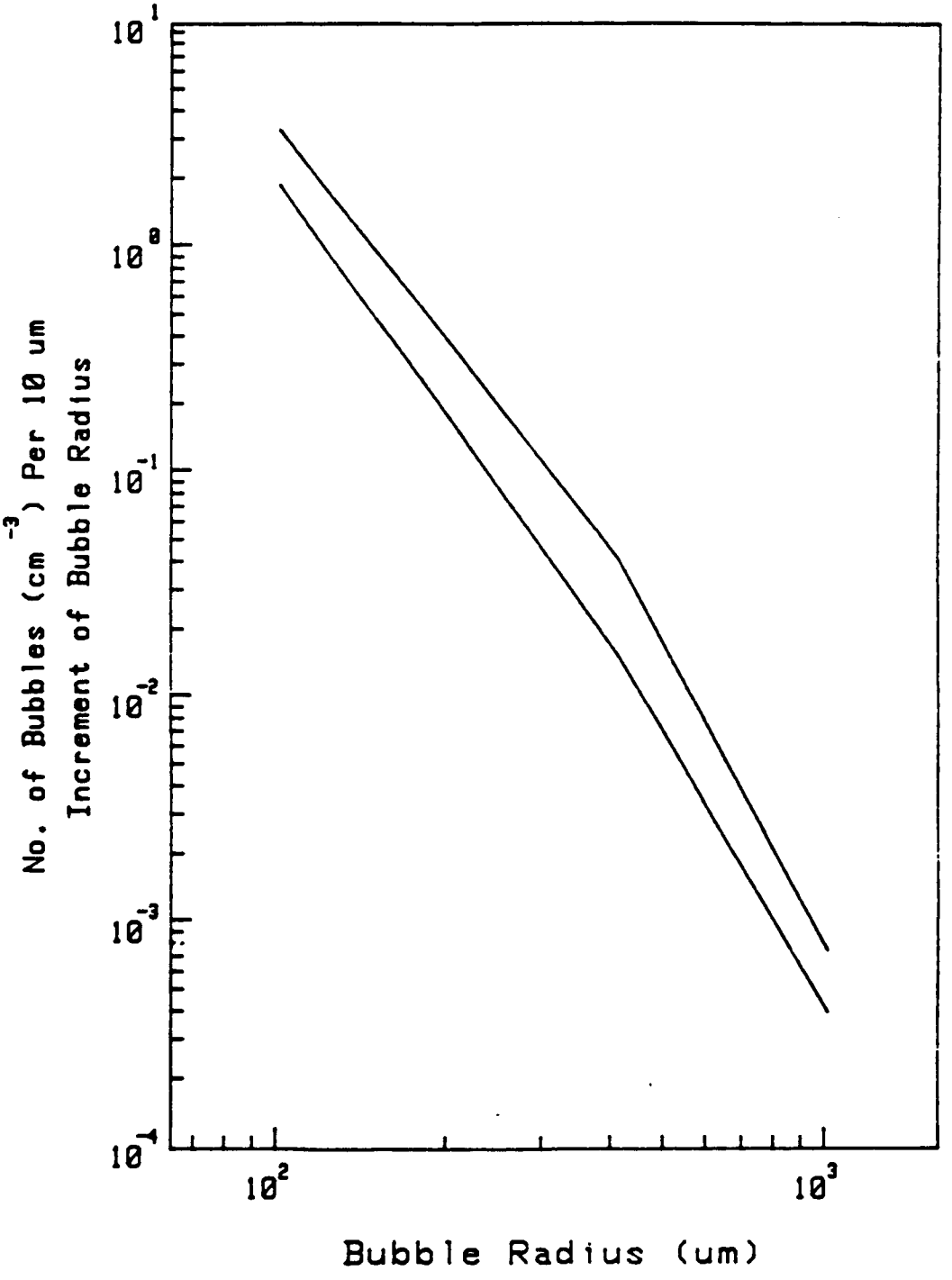

Figure 10. HEXIST spray bubbler number density bubble spectra (assumed) vs. bubble radius for two different air flow rates. The bubble spectra is given in number of bubbles per 10 μm increments so that the equivalent droplet increment (as used in the model) is 1 μm. The actual size distribution in $cm^{-3}\ \mu m^{-1}$ would equal these values divided by 10.

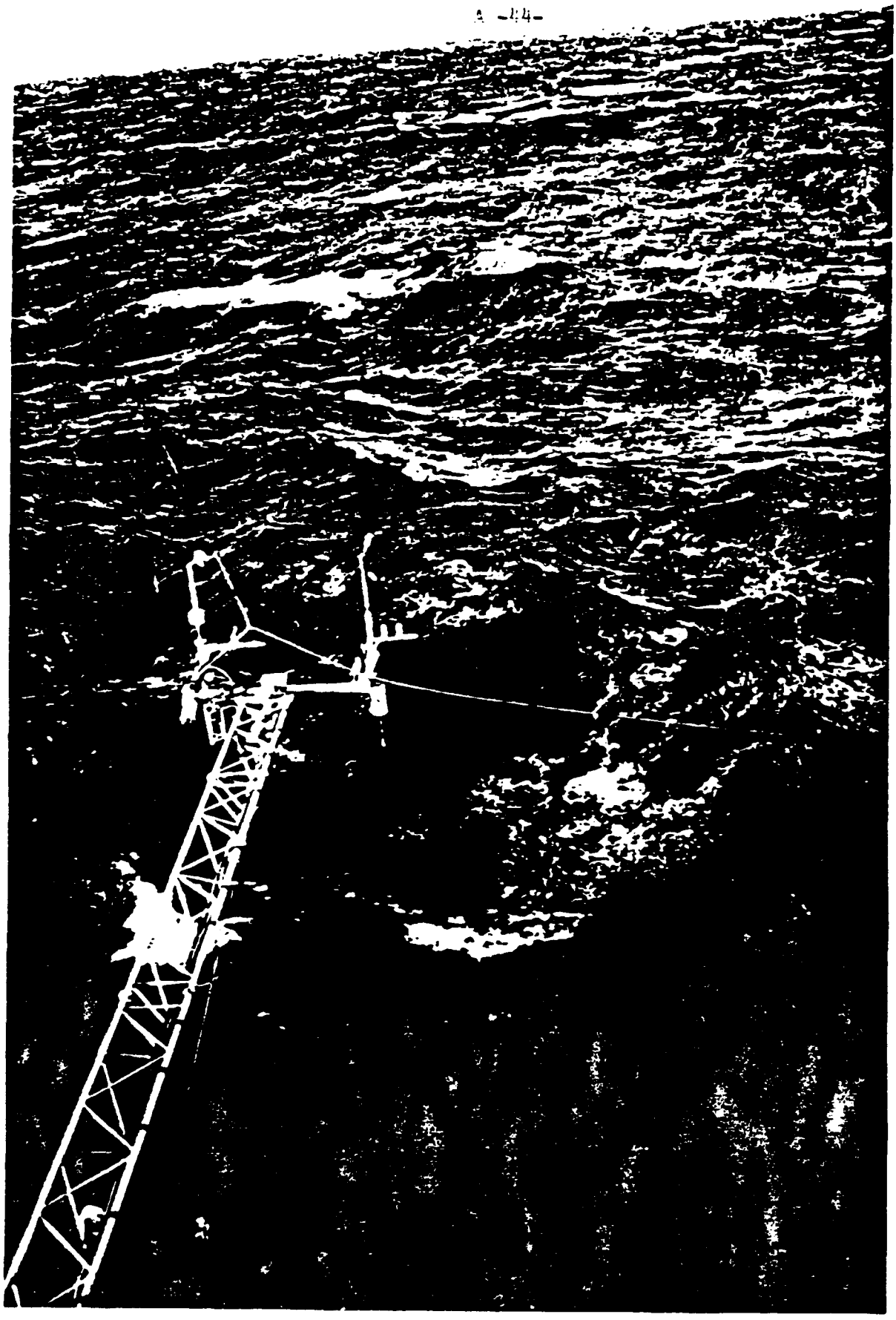

Figure 11. Photograph of the instrument boom deployed on the Dutch platform, MPN, in the North Sea during the HEXMAX experiment.

APPENDIX B

Inertial-Dissipation Air-Sea Flux Measurements I: Evaluation of a Prototype System

C.W. Fairall and J.B. Edson

Department of Meteorology

Pennsylvania State University

University Park, PA 16802

S.E. Larsen

Department of Meteorology and Wind Energy

Riso National Laboratory

DK-4000 Roskilde, Denmark

P.G. Mestayer

IMST Laboratoire de Luminy

12 Avenue du Geneal Leclerc

13003 Marseille, France

25 August 1988

CONTENTS

1. Introduction

The turbulent heat fluxes (sensible and latent) are important components of the total heat budget at the air/sea interface. The momentum flux (surface stress) is the major driver of ocean turbulence and surface currents. The interfacial heat budget is important in numerous areas of oceanography and meteorology (e.g., climate, forecasting, mixed-layer modeling). The total water flux (vapor plus droplet) and the sea-salt aerosol particle flux (droplet) are required for various aspects of meteorology (e.g., cloud processes, electro-optics, remote sensing). There are four standard methods for determining these fluxes from atmospheric information:

a) direct covariance (eddy correlation),

b) inertial subrange dissipation,

c) mean profiles,

d) bulk aerodynamic methods.

The covariance method is a direct computation from the data and yields the flux at the height of the measurement. The other three methods rely on similarity theory and yield only the interfacial value of the flux. The bulk method requires only mean meteorological information and is the obvious choice for climatological studies and numerical models. The covariance method is used extensively overland but, with the notable exception of the R/V Flip (Pond et al., 1971), straightforward application over the ocean is limited to fixed towers. If you wish to apply this method on a moving platform (ship or aircraft), then the orientation and motion of the platform must be accounted for before computing the correlations. This requires an inertial navigation system (INS) which costs about 250 k$. Thus, once you have obtained a suite of turbulence sensors (which could cost as little as 5 k$), you must spend an additional 250 k$ to use it on a ship or aircraft. This expenditure makes

sense for aircraft, which can measure the fluxes as a function of altitude, but on a ship even the covariance method can only give you the surface flux.

The dissipation method, which relies on measurements at high frequencies unaffected by ship motion, does not require an INS. It has been extensively used from research ships (cf Pond et al., 1971; Khalsa and Businger, 1977; Davidson et al., 1978; Fairall et al.,1980; Large and Pond, 1981, 1982; Schacher et al., 1981; Guest and Davidson, 1987) and even from small aircraft (Fairall and Markson, 1987). This method is a good compromise, being insensitive to platform motion (unlike the covariance method) and relatively insensitive to platform distortion of the air flow (unlike the covariance and profile methods). The dissipation method is more direct than the bulk method simply because it is a true turbulence statistic. While the dissipation method does rely on similarity theory, the similarity functions are well known in both stable and unstable conditions and have been verified over the ocean (Fairall and Larsen, 1986). Historically, inertial-dissipation measurements have had the reputation of being exotic because of a reliance on very fragile and cantankerous high speed sensors (hot-wire anemometers, cold-wire microthermal sensors, and Lyman-α hygrometers). Typically, time series were recorded in the field and months were spent in post processing. In this paper we will show that it is now possible to construct a system using much more rugged sensors (a sonic anemometer/thermometer and an IR hygrometer) with very stable calibrations and on-line spectral processing in order to obtain in realtime fluxes with accuracy comparable to covariance measurements. Those also interested in a slightly less 'high-tech' approach are referred to the developments using propeller anemometers (Large and Businger, 1988).

It is clear that oceanic fluxes are important in general and that the drag coefficients have many important uses. Given the practical difficulties

of defeating the flow distortion and motion problems associated with ship operations, the inertial-dissipation method is still the best candidate for obtaining massive amounts of data under a wide variety of atmospheric and oceanic conditions over the open ocean. However, both the practicality and the credibility of this method must be clearly established in the minds of the scientific community. This requires a comprehensive study of the method, development of reliable measurement systems, and comparison with other methods under carefully documented conditions. In recognition of this, a 'dissipation group' was formed as one element of the Humidity Exchange Over the Sea (HEXOS) program (Katsaros et al., 1987). Following a review of the theoretical basis of the dissipation method (Fairall and Larsen, 1986), two prototype second generation systems were assembled and then tested in HEXOS main experiment (HEXMAX), which was held on the Dutch offshore platform MPN in the North Sea in October and November of 1986. One system was deployed on a boom 8 m above the ocean in a region relatively free of flow distortion; the other system was deployed 7 m above the upwind edge of the helicopter deck in a region of considerable flow distortion. Covariance and inertial-dissipation flux estimates were obtained from both systems simultaneously.

In this paper we wish to describe the prototype system, discuss the rationale for the selection of sensors and processing techniques, provide an evaluation of the system from the HEXMAX data, and lay out our conclusions for a final system design. In a companion paper (Edson et al., 1989, which we will hereafter refer to as 'Part II') we will present an evaluation of the inertial-dissipation method including the uncertainty of dissipation flux estimates relative to covariance flux estimates and the comparitive effects of flow distortion. Before plunging into the instrumental details that are the focus of this paper, we will first explain (section 2) why turbulence measurements over the ocean cannot be replaced by bulk flux estimates for all

applications (i.e., the bulk method is necessary but not sufficient) and provide (section 3) a synopsis of similarity theory and the theoretical background involved in flux estimation (more detail is available in Fairall and Larsen, 1986). In section 4 the experimental details are presented (instrumentation and calibration); in section 5 the data acquisition and processing is described. System performance in the HEXMAX experiment is discussed in section 6. Our conclusions are given in section 7.

2. Limitations of the bulk method

The bulk aerodynamic method (drag coefficients) has and will continue to have a special place in flux estimation methods simply because of its extensive use in numerical models and its applicability to historical data sets from weather ships and ships of opportunity. Even the crudest global circulation models must place a lower boundary condition on the atmospheric variables. This is almost universally accomplished through the use of a surface condition and an appropriate 'geostrophic' drag coefficient that relates the surface flux to the difference in the atmospheric variable and the surface. This is a particularly attractive approach because the necessary mean meteorological variables are already computed by the model. As computer power increases, numerical weather models will begin to incorporate fairly realistic atmospheric boundary layer models that use actual surface layer drag coefficients. Thus, the need for realistic drag coefficients is likely to increase in the near future. It is also unlikely that more complex boundary layer model approaches will render drag coefficient obsolete. Even the sophisticated second order closure models, which obtain the fluxes directly from budget equations, still require the drag coefficients in order to establish a lower boundary condition.

Over the ocean, the drag coefficients present some unique problems that have been investigated for years. Historically, the roughness of the ocean has been treated as a unique function of wind speed only. Since the review paper by Garratt (1977), it has become apparent that surface waves (e.g., Geernaert et al., 1986) and sea spray droplets (e.g., Ling et al., 1980) cannot be ignored. Thus, at a given wind speed, the neutral drag coefficient is observed to exhibit considerable scatter. There is still uncertainty in the drag coefficient even under average conditions.

Simultaneous flux and bulk meteorological measurements are used to develop parameterizations and evaluate transfer coefficients. The classic reviews on this subject (Garratt, 1977; Anderson and Smith, 1981) reveal a substantial mid-latitude bias in the field measurements with most of the data obtained in the 4 to 15 m/s wind speed regime. The majority are also from offshore towers, coastal regions and other shallow water regimes. For example, Blanc (1985) evaluated 10 published bulk transfer schemes. One scheme was based on 40 data points from the Caspian Sea (10 m deep water). One scheme was based on six days of data from the East China Sea. Two of the schemes were actually based on wind tunnel measurements. This apparent chaos has led to the perception that the bulk method has a weak foundation. This is not true. A reasonable consensus has developed among the cognescenti in this field: for the average neutral drag coefficient (stress) the results of Smith (1980) or Large and Pond (1981) are solid choices in the wind speed range from 4 to 20 m/s. They don't differ by much, they are basically open ocean data, and future experiments are not likely to improve them by more than 10%. The situation for the sensible heat transfer coefficient (C_H) is not quite as favorable, while that for the latent heat is still worse. It is not clear if C_E is significantly different from C_H and their wind speed dependence, if any, is still controversial. Friehe and Schmitt (1976) obtained a best estimate of C_E from a handful of data points culled from nine sets of measurements from other investigators. When Anderson and Smith (1981) updated the estimate, only a few new measurements were available. Blanc's (1985) study showed considerable variation for the humidity transfer coefficient and it is clear that much more open ocean data is needed.

In computing longterm averages of the surfaces fluxes, one can assume that the atmospheric variability and random instrumentation/measurement errors

tend to average out. For bulk meteorological data of reasonable quality the major source of uncertainty in the long term mean estimates of stress, sensible heat and latent heat is probably due to uncertainties in the air-sea transfer coefficients. However, air-sea flux estimates made in conjunction with studies of atmospheric or ocean boundary-layer and mesoscale processes are usually needed on one hour time scales (to properly resolve details of the diurnal cycle or mesoscale spatial structures). In this case atmospheric sampling variability, sensor errors, and flow distortion may be very important (see the analysis by Blanc, 1987). Transfer coefficients can be made correct on average , but it turns out that one hour bulk estimates of air-sea fluxes are subject to an rms variability on the order of 30%-40%. Furthermore, variations in wave conditions, boundary layer equilibrium, water surface properties, or spray conditions will all increase this uncertainty. These local variations may be quite critical to oceanic and atmospheric boundary layer dynamics and in the dynamics of mesoscale weather phenomena that are strongly influenced by boundary layer interactions. Studies of such phenomena should be supported by more direct forms of air-sea flux measurement.

3. Theory

a. Surface layer scaling

The surface fluxes are defined by the relations

$$\tau = \rho\overline{w'u'} \tag{1a}$$

$$H = \rho c_p\overline{w'T'} \tag{1b}$$

$$E = \rho L_e\overline{w'q'} \tag{1c}$$

where τ is the Reynolds stress, H the sensible heat flux, E the latent heat flux, ρ the density of air, c_p the specific heat of air, and L_e the latent heat of vaporization of water. Primes denote turbulent fluctuations, where T is the temperature, q the specific humidity, u the streamwise velocity, and w the vertical velocity component. The overbar denotes an average over an infinite ensemble. The value of the fluxes at the surface (denoted by the zero subscript) can be related to the Monin-Obukhov (hereafter, MO) scaling parameters for velocity, u_*, temperature, T_*, and humidity, q_*,

$$\tau_o = -\rho u_*^2 \tag{2a}$$

$$H_o = -\rho c_p u_* T_* \tag{2b}$$

$$E_o = -\rho L_e u_* q_* \tag{2c}$$

The surface fluxes or scaling parameters also define the MO stability length

$$L = T/(\kappa g)\ u_*^2/(T_* + 0.61Tq_*) \tag{3}$$

b. Eddy covariance measurements

The fluxes of (1) can, in principle, be determined directly by cross

correlating simultaneous measurements of w' with the appropriate variable (u',T',q') over some finite period of time. The average correlation over this time period produces an estimate of the ensemble average covariance. The accuracy of this estimate is related to various meteorological factors and the length of the record (Wyngaard, 1974). Furthermore, the proper values for the fluctuations may require substantial corrections for platform motion and flow distortion. The velocity covariance is particularly sensitive to these effects.

c. Direct-dissipation method

The dissipation rates for turbulent kinetic energy (ϵ), one half the temperature variance (N_T) and one half the humidity variance (N_q) can be computed from the time derivatives of the fluctuations. For example,

$$\epsilon = 15\upsilon\langle(\partial u'/\partial t)(\partial u'/\partial t)\rangle/\langle u\rangle^2 \tag{4}$$

where the brackets denote the time average. Near the surface, we can estimate the MO scaling parameters from the TKE and variance budget equations near equilibrium

$$\epsilon\kappa z/u_*^3 = \phi_m(\xi) - \xi = \phi_e(\xi) \tag{5a}$$

$$N_T\kappa z/u_*T_*^2 = \phi_h(\xi) \tag{5b}$$

$$N_q\kappa z/u_*q_*^2 = \phi_h(\xi) \tag{5c}$$

where ξ=z/L is the normalized height, κ is von Karman's constant, and ϕ is the dimensionless gradient function for the appropriate variable. Thus, given measurements of each of the dissipations, we can solve (5) simultaneously by iteration to obtain the scaling parameters and, therefore, the fluxes.

d. Inertial-dissipation method

The largest problem with the direct dissipation method is the difficulty of making direct dissipation measurements in the field where the instrumental frequency response must approach 10 kHz. This is possible for very small (and fragile) hot wire anemometers but impossible with present technology with temperature and humidity sensors. This frequency response problem can be side-stepped by examining microturbulence at frequencies well below the dissipation range in the so-called inertial subrange of isotropic turbulence. In this frequency range the one-dimensional variance spectrum, S_x, of the variable x=u,T,q can be expressed as a function of wavenumber magnitude

$$S_x(k) = 0.25\ C_x^2\ k^{-5/3} \tag{6}$$

where the structure function parameter for the variable x is defined as

$$C_x^2 = \langle [X(r) - X(r+d)]^2 \rangle / d^{2/3} \tag{7}$$

where d denotes the separation distance of two measurements of X.

The structure functions are related to the dissipation variables through the Co:sin relations (using Kolmogorov constants of 0.5 for velocity and 0.8 for temperature and humidity)

$$\epsilon = [0.5\ C_u^2\ ]^{3/2} \tag{8a}$$

$$N_x = 0.31\ C_x^2\ \epsilon^{1/3} \tag{8b}$$

Thus, devices with frequency responses in the tens of Hertz can be used either individually (with eq. 6) or in pairs (with eq. 7) to obtain structure function parameters which can be converted dissipation via (8) in order to calculate the fluxes. Alternatively, one can use empirical stability

functions for the structure functions, f_x,

$$C_x^2 = x_*^2 \, z^{-2/3} f_x(\xi) \qquad (9)$$

and solve for the fluxes directly (more detail is given in Appendix A).

The estimation of fluxes from dissipation is not as 'direct' as the covariance method. Assuming that the various corrections can be made, the measured covariance is a reasonably unbiased estimate of the true ensemble averaged covariance (see the discussions of ergodicity in Panofsky and Dutton, 1984). The dissipation method relies on approximations to the variance budgets (as expressed in the empirical functions of stability) that can only be made accurate on average. However, because the dissipation methods are based on autovariance statistics, the time average approaches the ensemble average more rapidly than for the covariance statistics (Wyngaard, 1974; Fairall and Markson, 1987). This is very important because most of the uncertainty in covariance flux estimates under ideal conditions is due to atmospheric variability (20% to 50% for one hour averages).

4. Instrumentation

The goals of the 'inertial dissipation' group for the HEXOS program were to develop, deploy, and test an inertial dissipation flux package and to perform an in depth comparison of covariance and inertial dissipation flux estimates. Because we wanted to look at the flow distortion issue, two similar systems were deployed, one in a location with substantial flow distortion that one might expect to endure with instruments mounted on a ship. In this section we will discuss the sensors, their calibration, and the data acquisition/processing hardware. Except for some issues related to calibration, the data processing will be discussed in section 5.

Before describing the specific sensors used in the prototype system, a few comments on our strategy are in order. In general, we preferred to use commercially available sensors and we wanted to use sensors with which we had substantial experience at sea or at least in hostile environmental conditions. Of the 11 sensors deployed by the dissipation group (providing 17 variables) only the boom Lyman-α was being used in the field for the first time. Mean and turbulence measurements were considered separately. We put less emphasis on the mean meteorological data for the HEXMAX experiment because means were being measured by other investigators on the platform. For the turbulence sensors, function and the ability to stand up to marine conditions were the primary concern. For example, extremely expensive sonic anemometers were chosen because we had confidence in their reliability (two years of continuous measurements in Jutland; see Mortensen et al., 1987) and, more importantly, the particular units chosen provided sonic temperature.

Measurements were made with two instrumented packages: one on a 16 m long boom deployed from the side of the platform at a nominal height of 8 m over the ocean, and one on a 7 m tall mast located on the helicopter deck at a

total height of 26 m above the ocean (see Fig. 1). Each package contained a rugged three-axis sonic anemometer, a cooled mirror dew point temperature sensor, and a Lyman-α fast hygrometer. Precision thermistors were used to measure water temperature and air temperature (at the 26 m mast only). This can be viewed as the basic prototype inertial-dissipation flux system. The mast sensors were deliberately located in a region of severe flow distortion (typical wind vectors were tilted 10 degrees relative to horizontal versus only one degree on the boom). Additionally, standard high speed turbulence sensors (hot-wires, cold-wires, and hot-films) were used to provide reference to traditional turbulence measurements. The fragile sensors (hot-wire anemometers and cold-wire fast temperature sensors) were used on the boom, which was accessible every hour for cleaning or replacement. The hot-film was used on the mast and was replaced about once a week. See Table 1 for a listing and classification of the sensors. The individual experimental packages are shown in Fig. 2. Since some of the measurements were a bit unconventional, additional information is given below.

a. Fast hygrometers

The Lyman-α's used on HEXMAX were the only instruments in the package that were not commercially produced. They were state-of-the-art instruments that reflect the humidity emphasis of the HEXMAX program. The units, which were the products of separate and lengthy development programs, were quite different.

The mast unit uses a traditional hydrogen gas discharge Lyman-α line source, with an NO detector (source and detector tubes obtained from Glass Technologists, Inc., Columbia, MD) that is functionally similar to several commercial available units. The electronics were designed and built at RISO

National Laboratory in Denmark and the physical structure was constructed at Penn State University (PSU). The electronics features the most modern 'electrometer' detector, separate channels for mean and fluctuating signals, 1 kHz frequency response, and very low noise interconnections. The physical structure is made of stainless steel and aluminum and was designed with the tubes and electronics boxes separated by about 50 cm. The source and detector tubes are mounted opposing in a stubby tuning-fork like configuration in a very open structure which, with the electronics boxes well removed, yields a minimum flow distortion.

The boom Lyman-α was developed jointly at the Institut de Mecanique et Statistique de la Turbulence (IMST) and the Service d'Aeronomie du CNRS (SA) in France with additional assistance from RISO. For simplicity we will refer to this device as the IMST/SA Lyman-α. This system employs special gas discharge sources and a photomultiplier detector rather than the NO detector, which gives it superior signal to noise performance. Since this particular device has been described in detail elsewhere (Mestayer et al., 1986, 1987 and 1988), we won't discuss it further here. Both instruments have MgF_2 windows which were left exposed to the elements to maximize ventilation efficiency. Rain and sea spray were periodically wiped off with cotton swabs using a 50% mixture of distilled water and ethyl alcohol. About once a day the windows were polished with 0.05 μm alumina powder.

Lyman-α's are notoriously fickle and obtaining a reliable calibration of their sensitivity to humidity fluctuations is a problem that continues to plague their users. The most common methods are varying the optical path (Buck, 1976), varying the humidity (in the laboratory), and comparing the Lyman-α to another slow response hygrometer (continuously during the experiment) as an absolute standard. The third method is referred to as a 'dynamic calibration' because the sensitivity of the fast sensor is determined

as the ratio of the standard deviation of the slow device to the standard deviation of the fast sensor (appropriately low-pass filtered to match the high frequency response of the slower sensor). In other words, the sensitivity of the Lyman-α is adjusted so that it yields the same variance in the frequency range measured by the slower sensor. For the slower sensor, we used cooled-mirror dew point hygrometers with a 10 s response time (described below).

The dynamic calibration method is excellent if one has a reliable (but slower) standard sensor. This approach was very successful for providing calibrations of hot-wires and hot-films (the sonic anemometers were the slow standard) during HEXMAX, but it was a total failure for humidity because the cooled-mirror dew point devices performed poorly in the marine environment. The two identical cooled mirror dew point devices often gave radically different mean humidity and humidity variances (much different than explainable by their vertical separation). The resulting Lyman-α sensitivities were quite variable and simply not credible.

As a backup to the dynamic calibration, we used a calibration equation developed from measuring the variations of the mean output voltage of the Lyman-α as a function of optical path. Corrections for collimation and oxygen absorption were made as described by Buck (1985). Since the Lyman-α is approximately a Beer's law absorption device, the fluctuations of the natural log of the detector voltage are proportional to fluctuations in the absolute humidity. If V' is a fluctuation of the detector voltage, V the mean detector voltage, and V_1' a fluctuation of the log of the detector output, then we can write

$$V_1' = V'/V = -B\ Q' \qquad (10)$$

where Q' is a fluctuation in absolute humidity and B the Lyman-α sensitivity (the larger B, the more sensitive the Lyman-α). We use the notation V_l to imply the natural log of the detector output is a voltage output by a log amplifier. Buck (1983, 1985) provided polynomial expansions for the mean response of the Lyman-α in the form

$$V_l = \sum_{n=0}^{4} c_n (Qx)^n + f_c + f_o \qquad (11)$$

where Q is in g m^{-3} of water vapor, x the spacing between the source and detector windows, f_c is a collimation correction and f_o is an oxygen absorption correction.

The PSU unit was calibrated in the laboratory by varying the spacing from 0.5 to 5 cm at an ambient humidity of 4.2 g m^{-3}. The polynomial coefficients given by Buck (private communication) were found to fit the data. If x is expressed in cm, we find c_n=(2.23,-0.382,0.0121,-0.00019,1*10^{-6}). The sensitivity of the Lyman-α to fluctuations in humidity is found by taking the derivative of (11). At fixed spacing, the collimation correction does not enter the sensitivity and we will neglect the temperature sensitivity that results from the derivative of the oxygen absorption (Mestayer and Rebattet, 1985). Note that the sensitivity depends on the spacing and the ambient absolute humidity. Subsequent to HEXMAX, this calibration was found to overestimate the Lyman-α sensitivity by about 60%. Side-by-side comparison with an infrared hygrometer at PSU indicated that B should be decreased by a factor of 1.65. This was consistent with comparisons made during HEXMAX with the calibrated Lyman-α used by the Bedford Institute of Oceanography and also consistent with later surface energy budget studies done at PSU. The final result is

$$B = -0.6 \times \sum_{n=1}^{4} n\, c_n (Qx)^{n-1} \qquad (12)$$

For a spacing of 1 cm, a typical value for B is 0.1 $(g\ m^{-3})^{-1}$ or a positive humidity fluctuation of 1 g m^{-3} causes the Lyman-α detector voltage to decrease by about 10%. By comparing the boom and mast Lyman-α humidity variances measured during HEXMAX, we concluded than (12) was also applicable to the IMST/SA unit.

b. Sonic anemometers

Kaijo-Denke model DAT-300 sonic anemometer/thermometers were used in both packages. The mast unit used a TR-61B (strong wind type) probe. When viewed from above, this configuration has 120° rotational symmetry (Fig 3). The standard orthogonal wind components (u,v,w) are computed (internally) from the components measured along the acoustic paths. The boom package used a TR-61A probe (Fig. 3). The TR-61B probe is intended for lengthy, unattended operations and the TR-61A is intended for attended research applications. The TR-61A configuration has one pair of transducers vertically oriented for direct measurement of the vertical velocity component. The TR-61A is designed for minimum flow distortion when maintained at a particular orientation with respect to the wind. During HEXMAX this unit was mounted on a rotor and adjusted every hour to keep it pointed into the wind. The orientation of the mast unit was not changed during the experiment. However, since the TR-61B probe is very ruggedly constructed, considerable flow distortion is caused by the transducer units and the metal frame used to support them. This flow distortion was measured, as a function of orientation, in a wind tunnel in Denmark (Mortensen et al., 1987). Based on this calibration, the measured wind components were corrected at every time step.

The DAT-300 type sonics are fully digital systems. The wind components are computed from the difference of one over the transmission times for opposing transmission directions. The sonic temperature, which is based on the temperature dependence of the speed of sound (Wesely, 1976), is computed from the sum of one over the transmission times. The so-called 'one over t' method requires fewer approximations than the time difference/sum method originally used in analog sonic anemometers (Friehe, 1983). Sonic temperature measurements were considered critical to the HEXMAX experiment because of the known problems with sea salt contamination of microthermal temperature sensors (Schmitt et al., 1978; Fairall et al., 1979). Our intention was to use sonic temperature for covariance and inertial-dissipation heat flux estimates. Because the speed of sound also depends on humidity and because of velocity crosstalk inherent in the sonic, the sonic temperature flux must be corrected (Schotanus et al., 1983)

$$\overline{w'T'} = \overline{w'T_s'} - 0.51\,\bar{T}\,\overline{w'q'} - 2(\bar{T}\,\bar{u}/c^2)u_*^2 \qquad (13)$$

where T_s represents the measured (sonic) temperature and c is the speed of sound. The beauty of this approach is that only a sonic anemometer/thermometer and a fast hygrometer are needed to measure the three primary surface fluxes. Problems with inertial-dissipation measurements with sonic temperature are discussed in section 6.

c. Slow hygrometers

A cooled-mirror dew point sensor (EG&G model 156A) was used at each instrument level. The sensing heads were integrated into the instrument mounts and aspirated through tygon tubes that ran back to the laboratory spaces on the platform. A flowmeter was used to monitor and control the air

flow. We experimented with the flow rate but, within the range examined, did not find any obvious effects on the mean dew point or the response time.

As mentioned earlier, these devices did not perform satisfactorily during the experiment. They often disagreed by 2-3 degrees centigrade and typically read higher than dew points computed from handheld psychrometer readings. We also experimented with the gain and thickness adjustments on the dew point sensor control units, but no miracle cures were found. Since these particular models were originally designed for aircraft applications, it may be that we were simply asking too much of them. In the end we decided not to use the dew point sensor humidity variances (see the discussion concerning Lyman-α calibration); mean humidity values were calculated from the University of Washington wet and dry thermistor system, which was 'in situ' calibrated against the handheld psychrometric data. While we cannot offer any convincing explanations for the dissappointing results with the dew point sensors, it has been our experience with other cooled-mirror devices that they have performed much better in the laboratory than in the marine environment.

d. Microturbulence sensors

While we don't envision hot-wires and cold-wires as a part of a practical inertial-dissipation flux package, they were included on the HEXMAX experiment for several reasons. Firstly, they are the old standbys of turbulence work and their characteristics are very well understood. Secondly, they provided us with frequency response into the kHz. This allows us to establish definitively that the limited frequency response (15 Hz) of the sonic anemometer is adequate to reach the inertial subrange of isotropic turbulence. Thirdly, in the case of velocity turbulence, we could do direct dissipation measurements via (4). This serves as a check on our spectral density computations. And finally, the microthermal sensors allow us to see

if sonic temperature will give more consistent and more realistic sensible heat fluxes when compared to salt contaminated resistance wires.

On the boom standard DISA hot-wire type P11 probes (5 μm diameter platinum, 1mm in length) were used. Several different temperature probes were used but DISA type P31 probes with 1 μm diameter platinum wire, 0.5 mm in length were the preferred choice because they had the longest lifetime in the sea spray environment. Because of their small length to diameter ratio, these sensors have substantial probe support effects that retard their response above the probe support response frequency, which is believed to be a few Hz (Larsen et al., 1980; Larsen and Hojstrup, 1982). Thus their sensitivity for inertial subrange turbulence measurements may be significantly (as much 40%) lower than for covariance measurements. Because we are not sure of the proper frequency for this sensitivity transition for the P31 wires and because we also used other types of wires during the experiment, we have chosen to ignore this effect. Potentially we could be underestimating the temperature variance in the inertial subrange, but this turns out to be more than compensated by salt contamination effects.

5. Data acquisition and processing

The data were acquired and processed by two separate small computers. One computer (an HP217) was assigned all mean meteorological and inertial-dissipation flux estimation tasks for both instrument packages. The second computer (a PC clone) operated completely independently (digitizing many of the same signals in parallel with the first computer) to produce the covariance flux computations. While the first computer was capable of handling both tasks, time constraints (i.e., the need to complete the preparations in time for the HEXMAX field program) and pre-existing covariance software forced us to develop the HEXMAX software in parallel. This approach has the advantage that the inertial-dissipation system (instruments and processor) is self contained and its functions are not polluted with covariance computation tasks. After the experiment, the two data archives were used to produce a single edited and integrated file of one hour averages.

a. Inertial-dissipation

1) HARDWARE

A Hewlett-Packard model HP217 desktop computer was used for the dissipation package. The computer is based on the Motorola MC68010 16-bit (32-bit internal) processor chip. We chose to use the Rocky Mountain BASIC language because it is extremely powerful for I/O intensive tasks and is very convenient for writing and debugging complex programs that will almost certainly require considerable modification and streamlining in the field. The computer has 6 slots in the back: two were occupied with a video driver interface, one with a 2 Mb RAM card, one with a 16 channel 12-bit analog to digital converter card, one with a floating point processor card, and one with a high speed FFT processor card (see Table 2). This computer also has a

built-in serial communications interface (RS-232) and a parallel communications interface (IEEE-488). The parallel interface (referred to by Hewlett-Packard as HP-IB) permits up to 10 individually addressed instruments to be connected to the computer. This interface was used to operate a dual floppy disc unit, a printer, and a voltmeter/scanner unit. The system architecture is shown in Fig. 4.

2) ACQUISITION AND PREPROCESSING

The computer performed two separate data acquisition tasks. Nine mean variables were obtained with a relatively slow but very accurate voltmeter/scanner unit. The standard mean meteorological variables measured were wind speed and dew point at both levels, air temperature at the mast, and sea surface temperature. Also recorded with this system were RMS module outputs for the time derivative of the boom hot wire signal (for direct dissipation) and a bandpass filtered mast hot film signal (for non-spectral inertial subrange ϵ computations). The mean voltage of the mast hot film was also recorded for dynamic calibration (the hot film signal was not spectrally processed). Each slow variable was scanned once for every fast (turbulence) data acquisition cycle.

Each fast acquisition cycle involved scanning and digitizing 8 channels of turbulence (see Table 3) data 128 times in 0.5 seconds in a buffered transfer. Two buffers were used so that the most recent set of data could be processed while the next set was filling the other buffer. This allowed us to acquire and spectrally process 8 channels of data at a Nyquist frequency of 128 Hz and obtain 9 channels of slow data in realtime. This computation speed was made possible by a combination of the FFT card, the floating point accelerator board, heavy use of matrix operations, and a BASIC language compiler.

All eight channels of data were received in a single block of 8 times 128 (i.e., 1024) voltages. After a block of fast data was complete it was processes as follows. For each channel the half second mean value for all 128 points was computed, removed from the time series and stored in RAM, a Hamming window was applied to the time series, a 128 point FFT was computed by subroutine call to the FFT board, and the fourier coefficients were squared and accumulated in RAM. After processing all 8 fast channels, one scan of each of the slow variables was made and the slow data accumulated. The computer then waited for the next buffer of data to be filled. When that data became available, it initiated the transfer of the next block to the other buffer and began the processing cycle again.

3) AVERAGING AND ANALYSIS

At the end of an averaging period, averages, variances, spectra, and meteorological variables were computed and stored on disc. All data are stored as raw voltages along with gains, calibration factors, and a status indicator for each channel. We prefer to store the raw data (rather than final engineering units) because it greatly reduces the reprocessing necessary as calibration factors and postprocessing techniques are changed or coding errors are found during and after the experiment. No linear trend removal was used, so a relatively short average period (10 minutes) was selected. Later, these 10 minute periods would be used to compute one hour block averages.

Means and variances were computed for the 9 slow signals. Ten minute means and variances were also computed from the time series of half second means removed from the fast data blocks (see above). These variances, which are from the same frequency region of the variance spectrum (about 0.0016 to 2 Hz) as the slowly scanned data, are referred to as slow variances. The slow variances were used for the dynamic calibrations (the Lyman-α time series were

low pass filtered to match the 10 s response of the dew point sensors before computing the variance). A fast variance could also be computed by integrating the variance spectra from 2 to 128 Hz. Structure functions, dissipations, stress and drag coefficients were all computed and printed at the end of the 10 minute period.

4) SAMPLE OUTPUT

Since this description is probably indigestibly complicated, a sample printout from HEXMAX is given in Table 4. After the date and time, information and data analyses from the boom and the mast are followed by raw voltage information for the fast and slow data channels. For the fast data, spectral estimates of the structure functions and dissipations are also given. The interpretation of the printout is obvious for some of the data given, but quite a bit of the information is abbreviated or specialized to save space. 'Sonic wind: mean and sigma 'is clearly the mean and standard deviation of the wind speed (ms^{-1}). The line labeled 'EG&G' gives the mean dew point temperature (°C), relative humidity (%), the standard deviation of dew point temperature, the mean specific humidity ($g\ kg^{-1}$), and the standard deviation of specific humidity - all from the cooled mirror dew point sensor. Sensitivities for the hot-wire and the Lyman-α's from the dynamic calibration are given as the ratio of the standard deviation (slow RMS) of the reference device to the standard deviation of the voltage of the fast device

$$\text{Sensitivity} = \sigma_x/\sigma_v \qquad (15)$$

The B coefficients shown for the hot-wire and the hot-film are based on a King's law (Hinze, 1980) wind speed dependence (V^2=constant+B $u^{0.5}$) which we have computed from the slow variances

$$B = 4\,\bar{V}\,\bar{u}^{-0.5}\,\sigma_v/\sigma_u \qquad (16)$$

This coefficient is not explicitly used in the analysis, but is displayed in realtime to diagnose problems (ageing, salt buildup, or noise) with the sensors. Depending of the type of sensor and the overheat, we have nominal values that we expect. Also, the values should be quite consistent from one 10 minute period to the next.

The output of the boom hot-wire is used to compute a direct dissipation value for ϵ (1.3 E-2 m^2s^{-3}) at 8 m height which gives the estimates of friction velocity and 10 m drag coefficient that follow. The anemometer signal is fed to an analog differentiator, then to an analog RMS module which is sampled as a dc voltage on channel 12. Note that this direct estimate of ϵ can be compared to the spectral value computed from the very same hot-wire (1.54 E-2) that appears in the EPS,CHI column for channel 2 and with the spectral value obtained from the boom sonic anemometer (1.37 E-2) that appears in the same column for channel 4. A value for ϵ (3.9 E-3) at 26 m height is obtained from the mast hot-film using the filtered-variance method. The signal is bandpass filtered (10 to 40 Hz) and fed to an analog RMS unit that is sampled as a dc voltage on channel 14. This value can be compared with the spectral estimate from the mast sonic anemometer (3.67 E-3) given in the EPS,CHI column for channel 7.

The 'FAST DATA' and 'SCANNER DATA' tables are fairly self explanatory. A channel is given a status of 1 if it is considered in operation and 0 if not. The mnemonics given in the signal column correspond to the information given in Table 3. The 'MEAN' and 'RMS' columns are given in voltage units. The 'FST_RMS' is the integral of the variance spectrum from 2 to 128 Hz while the 'SLO_RMS' is computed from the ten minute time series of the average of the 128 samples obtained in the half second fast sample. The C_x^2 column

is the structure function computed from the low frequency end of the variance spectrum. The 'EPS/CHI' column gives ϵ for a velocity variable or N_x for a scalar variable (also spectral values). Note that the boom (channel 9) and mast (channel 10) were assigned a status. This was necessary since the boom sensors were not valid when the boom was raised up for servicing. The mast was occasionally taken down for helicopter landings.

b. Covariance

Since comparison of inertial-dissipation and covariance flux estimates was a major objective of the dissipation group, we decided it was necessary to compute covariances from our own sensors rather than rely on covariances computed from other groups on the platform. Therefore, all of the signals required for covariances relevant to the study were simultaneous acquired with a Personal Computer (PC) clone with a relatively slow 16 channel 12-bit analog to digital conversion board. This system scanned a total of 16 variables about once per second. Both sonics (u,v,w,T_s), both Lyman-α's, and both cooled mirror dew pointers were measured. Also, the hot-wire, cold-wire and horizontal wind speed (from an analog u-v vector module) from the boom were measured as well as the hot-film anemometer from the mast.

At each of the two instrument levels, means and variances were computed for each variable. Covariances (correlations) were computed for all combinations of each fast variable at a given level. The fast data (i.e., excluding the dew point systems) were displayed as an 8 x 8 matrix for the boom and a 6 x 6 matrix for the mast (the diagonals being the variances and the off diagonals the covariances).

The effects of flow distortion were handled by rotating the coordinates to correspond to the local flow direction. This is accomplished by rotating

about the original vertical axis to align the x-axis with the mean horizontal wind and then rotating about the y-axis to force the mean vertical velocity to zero in the new coordinate system (Tanner and Thurtell, 1969). The same rotations are performed on the variance-covariance matrix to produce a new matrix that is corrected for the vertical tilt of the flow. This makes u the streamwise wind component direction, v the horizontal transverse wind component (with zero mean) and w the vertical component (also with zero mean). This is equivalent to assuming that the flow distortion just tilts the flow but does not modify the turbulence and is, therefore, indistinguishable from simply tilting the anemometer. This issue is discussed further in Part II.

The approach of summing the variables and their squares and cross products and computing the necessary statistics at the end of an averaging period, and then rotating the axes into the mean flow is very convenient for realtime flux processing with a cheap and slow computer. However, it is not very convenient to use many high-pass filter techniques (linear trend removal, digital filters, etc) that are often executed on the complete time series (which we have not saved). Thus, our high-pass filter function is created by using relatively short (10 minute) time averages which are later averaged together to give a one hour estimate of the flux. Subsequent comparisons with other investigators from HEXMAX have shown excellent agreement with boom covariance stress values (which they computed from the same instruments using the complete time series).

6. Results

The HEXMAX experiment was conducted in the North Sea during a 6 week period in the fall of 1986. Many days of wind speeds in excess of 10 ms^{-1} occurred during the experiment and after the first week the wind direction was predominantly favorable for the measurements. The data from the two computer systems have been merged into 291 individual runs of nominally one hour length. A standard mean humidity (discussed earlier) and tidal information (used to obtain the correct instrument heights above the water) were added later. The Lyman-α data were reprocessed based on the new calibration discussed in section 4. The mean wind speeds at the boom and mast were corrected as a function of wind direction based on MPN platform model wind tunnel studies (Wills, 1985; In der Maur, 1977). The mean wind speed corrections are typically +5% at the boom and -8% at the mast.

In this section we will examine the results of the experiment from a systems and measurements point of view: which sensors gave us problems, the consistency of different dissipation estimates, and a look at flux estimates. An examination of the inertial-dissipation method itself is the subject of Part II.

a. Sample spectra

Previous realtime inertial-dissipation flux systems used analog preprocessing (differentiators or filter variance methods) with analog RMS modules that were sampled at a relatively slow rate. Spectral processing provides much more flexibility than analog processing. Once a measurement problem has been 'RMSed' it can be very difficult to separate it from the real data. Spectral processing has the advantage than many common problems are straightforwardly dealt with at the spectral level. For instance, low signal

to noise conditions can be diagnosed by examining the frequency dependence of the spectrum. For noisy sensors the signal to noise can often be improved by determining the broadband white noise level from the high frequency part of the spectrum and subtracting it from the entire spectrum (Beecher, 1988). Narrow band noise that appears as spikes in the spectrum (60 and 120 Hz are almost ubiquitous) can be trivially removed in software. Correcting for inadequate sensor frequency response is also trivial if one's basic data is the variance spectrum. Since the spectrum provides so much more information than just the RMS, it is more useful for diagnosing problems during the experiment.

Sample spectra in the format of frequency times spectral density versus frequency are shown in Fig. 5 for the data record given in Table 4. These are the 10 minute spectral graphs exactly as they appeared during the experiment. The dotted line indicates the inertial subrange frequency dependence ($f^{-2/3}$ in this format) fit to the value of the spectral density at 2 Hz (this value was somewhat arbitrarily selected; more sophisticated approaches were used for the post experiment analysis). The values of the structure function given in the upper right hand corner of the graph are computed for this line. In the case of the cold-wire temperature sensor (Fig. 5a), this first point was usually low because the temperature bridge was not completely compatible with single-ended input mode used for the fast A/D. This particular spectrum appears to be too flat to be a good inertial subrange spectrum, probably as a result of salt contamination. The slight upturn of the spectrum above 100 Hz (also obvious in the hot-wire spectrum shown in Fig. 5b, the boom Lyman-α spectrum in Fig. 5c, and the mast Lyman-α spectrum in Fig. 5f) is due to aliasing. Our anti-aliasing filters (a bank of 8) were hardwired for a low-pass cutoff of 150 Hz, which was a little too high for a Nyquist frequency

of 128 Hz but not worth the trouble involved in modifying the filter unit.

The boom sonic u spectra (Fig. 5d) and the mast sonic u spectra (Fig. 5g) generally indicated a good inertial subrange up to about 10 Hz. The limited frequency response and the effects of path averaging are clearly seen in the rapid drop of the spectral density above 10 Hz. Notice also the white noise levels of these devices above about 30 Hz. The sonic temperature spectra (Figs. 5e and 5h) bear no resemblance to inertial subrange spectra. This is caused by the sampling approach used in the Kaijo-Denke sonic, which uses one opposing pair of transducers that alternately transmit, then receive sound pulses. While this leads to much smaller transducer drift errors than four transducer sonics which transmit in both directions simultaneously, the time delay (0.008 s) between the alternate propagation direction samples introduces an additional velocity crosstalk component into the temperature sample. Thus, the sonic temperature variance spectrum is contaminated by velocity spectra. This will be looked at more closely below. In the high wind conditions of HEXMAX this contamination usually swamped the real temperature signal in the inertial subrange. Suprisingly, the vertical velocity - sonic temperature covariance is unaffected. Thus, the sonic provided reliable covariance estimates of the sensible heat flux but not inertial-dissipation estimates.

b. Analog ϵ estimates

1) DIRECT DISSIPATION METHOD

Two different analog processing methods were used in computing ϵ for comparison with the spectral results. For the direct method, the output of the boom hot-wire was low-pass filtered, time differentiated, and RMSed by analog electronic devices. The output of the RMS unit was sampled, squared, and averaged for 10 minutes; ϵ was computed from this average via (4). Since the derivative spectrum drops very rapidly above the Kolmogorov frequency

(Champagne et al., 1977), we used a low-pass filter to prevent broadband sensor and bridge noise from reaching the RMS unit. The filter frequency should be on the order of the Kolmogorov frequency, f_k, which we have estimated with the following equation

$$f_k = (\bar{u}/(2\pi))\ [(c_d^{1/2}\ \bar{u}/\upsilon)^3/(\kappa z)]^{1/4} \qquad (16)$$

Using a value of 0.035 for the square root of the drag coefficient over the ocean, (16) gives a frequency cutoff of 2.3 kHz at a wind speed of 10 ms^{-1} and 5.2 kHz at 15 ms^{-1}. We usually left the filter at 5 kHz unless the wind speed exceeded 15 ms^{-1}.

A sample velocity derivacive spectrum (Fig. 6) shows that the hot-wire data were of very high quality. A comparison of spectral and derivative estimates of ϵ is given in Fig. 7a. Recall that the hot-wire calibration is determined by low frequency comparison with the sonic anemometer. Because it is a high frequency measurement, the direct method is much more sensitive to loss of frequency response due to salt buildup on the wire. There were also a few problems with spikes due to the impact of sea spray and the occasional radio transmission. A straight log average implies a velocity Kolmogorov constant, α_u, of 0.62 +/- 0.02. This is a bit larger than typical values from high quality overland measurements (0.52 from Champagne et al, 1976; 0.59 from Dyer and Hicks, 1982), but we don't attach any significance to this result because it was not our intention to attempt a new determination of the Kolmogorov constant. The effect of using a value of 0.5 for α_u is that the direct dissipation estimates of ϵ are quite a bit lower than the inertial subrange values. Since the goal of this work is to estimate flux parameters, friction velocity estimates are compared in Fig. 7b. In our opinion, this does not imply a problem with the spectral analysis because, as we will see in

the next section, the filter-variance method yielded ϵ (or u_*) estimates slightly larger than the spectral method.

2) FILTER-VARIANCE METHOD

The filter-variance method is functionally equivalent to integrating the variance spectrum between lower (f_l) and upper (f_u) frequency limits (Khalsa and Businger, 1977). With analog processing, an RMS module produces this integral in the form of a band limited velocity variance, $\langle u'^2 \rangle_{l,u}$, which is used to compute ϵ

$$\epsilon^{2/3} = 2/3\ \alpha_u\ (2\pi/\bar{u})^{2/3} [f_l^{-2/3} - f_u^{-2/3}]^{-1} \langle u'^2 \rangle_{l,u} \qquad (17)$$

If the variance spectrum is digitally integrated between the same limits, then exactly the same value should be obtained for the spectral estimate of ϵ, except for errors in analog gains, A/D converters, filter cutoff frequencies, and the effects of the window used in the spectral computations. However, there are several ways to obtain ϵ from the spectrum. By summing the spectral components between the frequency limits (to digitally produce $\langle u'^2 \rangle_{l,u}$) we are heavily weighting the lowest frequency end of the spectrum. For a nice clean spectrum, it makes more statistical sense to weight equally all spectral values in the interval of interest. This is equivalent to computing a value of $\epsilon^{2/3}$ at each frequency and averaging or integrating the spectrum multiplied by $f^{5/3}$. In some cases (e.g., the sonic anemometers), we must be satisfied with only a narrow range of frequencies or even a single frequency interval. Since these 10 minute spectral are in fact the average of 120 half second spectra, they are very smooth and a single frequency bin is a highly representative (statistically) sample of the entire spectrum. A comparison of filter-variance (mast hot-film) and spectral (mast sonic anemometer) friction velocity estimates is shown in Fig. 8. In this case, the values are computed

from different instruments and from different parts of the frequency spectrum.

c. Sonic anemometer

The sonic anemometer offers a number of advantages for air-sea flux measurements. It has a very stable absolute velocity calibration and is an excellent sensor for mean wind speed, covariance, and inertial-dissipation measurements. The frequency response is significantly better than propeller anemometers, it has no overspeeding errors, and no moving parts that degrade during the experiment. Sonic temperature is still our best hope for avoiding sea-salt contamination problems.

In using sonic velocity for inertial-dissipation estimates of friction velocity, the major issue is the frequency response necessary to resolve the inertial subrange. We can easily examine this issue by comparing sonic spectral estimates of ϵ (or equivalently, u_*) with those obtained from hot-wire anemometers. We could carefully determine the sonic velocity transfer function and correct the variance spectra in order to extend the frequency range above 10 Hz. For this analysis we have simply used the spectral values in the 4 Hz to 8 Hz band (which corresponds to fz/u between 2 and 3 for most of the experiment) of the sonic spectrum. We have chosen to present this comparison in a different form than those presented earlier. In Fig. 9 we have shown the dimensionless velocity structure function parameter from the boom as a function of stability for the sonic and hot-wire spectral estimates. The normalized values of C_u^2 have been computed via (9) using covariance estimates of u_* obtained form the sonic. Notice the cluster of points is much tighter for the sonic (Fig. 9a) than for the hot-wire (Fig. 9b) and there is no obvious bias.

As we discussed earlier, we don't have a reliable standard to compare with the sonic temperature because sea-salt contamination of the cold-wires.

The nature of the temperature contamination by salt particles residing on small temperature sensors has been discussed by Schmitt et al. (1976), who suggested the 'cold spikes' that they observed on their temperature signal were due to the latent heat associated with the salt's response to ambient humidity fluctuations. Since humidity fluctuations are highly correlated with temperature correlations near the sea surface, this leads to an error in the velocity - temperature covariance that is not reduced by averaging. In unstable conditions, the contamination tends to amplify the temperature fluctuations. We have done a comparison of the sonic temperature with the cold-wire temperature in terms of the temperature scaling parameter (Fig. 10a), which is the vertical velocity - temperature covariance divided by u_*. Note, sonic temperature covariance has been corrected as per (14). Fig. 10b shows that the contamination effects are clearly worse using the inertial-dissipation method with the cold-wire.

We indicated earlier that the inertial-dissipation method could not be used with the sonic temperature because the temperature variance spectrum was contaminated by velocity fluctuations associated with the time delay between sampling the opposing acoustic propagation paths. A detailed study of this problem is the subject of another paper (Larsen et al., 1989), but we will briefly sketch it here. Consider a pair of opposing, vertically oriented transducers separated a distance x with a mean flow u normal to the acoustic path. Suppose at time $t-\tau$ we measure the time of flight of an acoustic pulse in one direction and at time $t+\tau$ we measure the time of flight in the opposite direction. Following Schotanus et al., (1983) we can write the measured speed of sound, c_m, as

$$c_m = [c(t+\tau)+c(t-\tau)]/2 + [w(t+\tau)-w(t-\tau)]/(2\cos(\alpha)) \qquad (18)$$

where w is the true vertical velocity, $\cos(\alpha)=[1-(u/c)^2]^{1/2}$,

$$c^2 = \gamma RT(1+0.51q) = \gamma RT_s \tag{19}$$

and γR is 403 $m^2 s^{-2} K^{-1}$. The $\cos(\alpha)$ factor is a source of velocity crosstalk that leads to the third term in (14). In order to simplify this illustration we will set $\cos(\alpha)$ to 1 and ignore its contribution. Using (19) we can relate fluctuations in sound speed to temperature and humidity fluctuations, which we will simply combine as the 'sonic temperature' fluctuation, T_s' as

$$T'_{sm} = [T'_s(t+\tau)+T'_s(t-\tau)]/2 + [w'(t+\tau)-w'(t-\tau)]*(a/2) \tag{20}$$

where $a=2T_s/c$.

The fourier transform of (20) gives us an equation for the measured sonic temperature variance frequency spectrum in terms of the true spectrum plus errors due to the velocity - temperature quadrature, Q_{wT}, and the vertical velocity variance spectrum, S_w,

$$S_{Tm} = S_T \cos^2(y) - a \sin(2y)Q_{wT} + a^2\sin^2(y)\, S_w \tag{21}$$

where $y=2\pi f\tau$, and T is meant to imply the sonic temperature.

The importance of the contamination terms in (21) depends on the design of the sonic and the atmospheric conditions. The conditions during HEXMAX (high winds and modest air sea temperature difference) led to a particularly unfavorable ratio of the real signal to the error terms. Under light wind, convective conditions the sonic temperature spectra appear normal. A few low frequency sonic temperature spectra from HEXMAX are available; an example is given in Fig. 11. We have included a humdity spectrum (normalized to agree

with the temperature spectrum at 0.1 Hz). We believe that the actual temperature spectrum should closely resemble the shape of the humidity spectrum. Notice that the cold-wire spectrum shows considerably more high frequency variance relative to the humidity spectrum, presumably the effects of salt contamination.

d. Sample fluxes

An evaluation of the inertial-dissipation flux estimates must include a comparison against covariance estimates, which are considered to be the measurement standard. It is also of interest to compare with bulk aerodynamic estimates. We will use the boom sensors for the comparisons shown here because flow distortion is not a serious consideration. For the bulk computations we will use the neutral drag coefficient of Smith (1980) and a constant neutral transfer coefficient of $1.15*10^{-3}$ for both sensible and latent heat (a slight variation of the S/F scheme from Blanc, 1985). The inertial-dissipation estimates present a slight problem because we were unable to produce a good high frequency temperature measurement (as discussed above). Since sensible heat is important in the hydrostatic stability corrections, this also influences our estimates of stress and latent heat. We could use the covariance sensible heat for this purpose, but that would be cheating. Therefore, we will use a modified Bowen ratio method to estimate sensible heat flux as proportional to the latent heat flux (inertial-dissipation value) scaled by the ratio of the air-sea potential temperature difference to the air-sea specific humidity difference.

Time series for a two week period are shown for stress (Fig. 12a), and latent heat (Fig.12b). Gaps in the time series are due to sensor maintainence, rain storms, the boom in the undeployed (maintainence) position, unfavorable wind directions, and stand-down periods for human factors (e.g.,

sleep). Under high wind speed conditions, the bulk stress estimates are significantly lower than the other two methods because the tower is located in rather shallow water (30 m depth). This leads to some steepening of the waves and a systematically greater drag coefficient. This serves to illustrate our point that the inertial-dissipation method yields much more reliable flux estimates than the bulk method when the surface wave conditions vary from the average expected for that wind speed.

Point-by-point comparisons of covariance versus inertial-dissipation estimates of u_* and q_* for the entire experimental period is shown in Fig. 13 (a similar comparison for T_* was discussed in regard to Fig. 10). We have done this comparison in terms of the scaling parameters (rather than the fluxes) in order to separate the uncertainties associated with the variables (velocity and humidity) and the instruments that measure them. The uncertainty in u_* is less than 10% and in q_* is about 15%. This translates to an inertial-dissipation uncertainties of about 20% for stress and 25% for latent heat flux. Recall that about half of the variance of the random disagreement of the two estimates should be associated with the sampling uncertainty of the covariance method. This is made quite clear in Part II, where a comparison of covariance estimates from the two measurement levels shows even greater scatter. One possible interpretation is that both the covariance and the inertial-dissipation values are estimates of the true ensemble average flux that are uncertain by these measured standard deviations divided by the square root of 2. This interpretation ignores the fact that the inertial-dissipation and covariance values are not independent but are in fact different computations schemes applied to the same sample. This issue is explored further in Part ...

7. Conclusions

The prototype inertial-dissipation flux measurement system deployed and tested on the HEXMAX experiment represents a clear step forward in developing a completely automated, low maintainence system suitable for deployment on ships. The inertial-dissipation estimates for stress and latent heat flux were comparable to covariance estimates (within about 20% to 30% for one hour averages, which is roughly the uncertainty of the covariance measurements). Inertial-dissipation sensible heat flux estimates were unsatisfactory because of various contamination problems. The use of realtime spectral analysis provided much greater flexibility in data processing and quality control.

The sonic anemometer proved ideal for stress measurements with either method. For sensible heat flux measurements the sonic temperature is excellent when the covariance method is used. It represents the only fast temperature sensor that we are aware of that is unaffected by sea salt contamination. The sampling mode used by the particular sonic anemometer model we used is subject to an additional source of velocity crosstalk in the temperature signal that contaminates the variance spectrum and causes problems with the inertial-dissipation sensible heat flux method. We are investigating the feasibility of correcting the temperature spectrum using the measured velocity spectra via (21). Incidently, this problem is not inherent to all sonic anemometers, but is a result of the alternating pulse design of the Kaijo Denke. A frequency swept design (a so-called 'chirp' sonic) is presently being developed at the National Center for Atmospheric Research (Onkley and Businger, private communication). About the only problem we experienced with the sonic anemometers was loss of data during periods of rain (presumably rain drop impact noise).

The Lyman-α fast hygrometers provided usable data but they require too

much maintainence. On the platform we could service the Lyman-α's when necessary (as often as hourly). However, on a ship it is impractical and even dangerous to climb masts and service equipment in rough weather. We recommend the Lyman-α be replaced by the dual wavelength infrared absorption hygrometer (commercially available from at least two manufacturers: OPHIR Corp. in the U.S. and Oktahki Corp. in Japan). We are presently testing an OPHIR unit at an instrumented site in central Pennsylvania where a sonic anemometer and a variety of other instruments are operated around the clock. The IR hygrometer is being used to continuously measure mean humidity and latent heat flux (by the covariance method). The hygrometer was operated unattended (without even being cleaned) from February, 1988 to July, 1988. A comparison of Lyman-α and IR hygrometer latent heat fluxes for more than two days in early March, 1988, is shown in Fig. 14. The only substantial disagreement occurred around sunup on day one, which was a period of light rain and sleet.

A complete flux measurement package can be assembled with a relatively small collection of devices. A sonic anemometer/thermometer and an IR hygrometer can provide the three basic turbulent fluxes, the mean wind speed and direction, and the mean humidity. Additional sensors are necessary for the sea surface temperature and the air temperature. The complete surface energy budget can be obtained by adding a net radiometer. Since it is difficult to keep a ship or platform superstructure out of the field of view of a net radiometer, downward solar and longwave radiometers can be combined with water temperature and an assumption of the sea surface albedo to compute the net radiative flux. Using a computer system comparable to the one described in this paper, the fluxes can be computed in realtime with the inertial-dissipation method, the covariance method, or both simultaneously. Because of the path lengths of the sonic and the IR hygrometer (25 cm) and an

upper frequency limit on the order of 10 Hz, the system described here should probably not be used much closer to the surface than about 5m. Above 50 m the constant flux assumption and the extrapolation of MO similarity become increasingly risky.

For operations from a tower overland or a fixed platform (such as the HEXMAX experiment) over the ocean, we favor using the covariance method with inertial-dissipation computations performed as a quality checking mechanism. The errors caused by flow distortion with the covariance method can be partially compensated by coordinate rotation, the use of long instrument booms, and empirical (e.g., wind tunnel studies with a scale model) or theoretical corrections (Wyngaard, 1981). It is not clear (see Part II) that, once these steps have been taken, that the inertial-dissipation method offers any significant advantages over the covariance method in flow distorted regimes. For operations from ships and buoys, we favor the inertial-dissipation method.

Acknowledgements . The technical contributions of Finn Hansen, Bertrand Zuchinni, and Richard Thompson are acknowledged. The authors wish to express their gratitude to the staff of the Metpost Noordwijk and to the scientists of the Royal Dutch Meteorological Institute (KNMI) for hosting a beautifully orchestrated field program. We also wish to thank Wiebe Oost, Stuart Smith, and Kristina Katsaros for bearing the administrative burdens of the HEXMAX experiment. This work was supported by the Marine Meteorology division of the Office of Naval Research (grants N00014-85-K-0250 and N00014-85-K-0123).

APPENDICES

Inertial-Dissipation Similarity Functions

The Monin-Obukhov similarity functions used to compute scaling parameters in the inertial-dissipation flux method are available in a bewildering variety in the literature. Recall that one also has the option of using the dissipation forms of the equations (5) or the structure function forms (9). There is also debate about the values of the Kolmogorov constants and the precise mathematical forms of the similarity functions. For simplicity and brevity, we will present only one approach and one set of similarity functions. Following recent developments in the literature (Andreas, 1987; Hill, 1988), we will assume that the scalar Kolmogorov constants and similarity functions are identical. The fluxes can be computed using (2) once we have obtained the scaling parameters.

Following Fairall and Larsen (1986), the dimensionless stability is found by iteratively solving the equation

$$\xi/\xi_o = F(\xi) \tag{A1}$$

where ξ_o is computed from the measured structure functions

$$\xi_o = +/- \; 4\kappa g z^{2/3} (T/5) \; [(C_T^2)^{1/2} + 0.61T(C_q^2)^{1/2}]/C_u^2 \tag{A2}$$

In this expression z represents the height of the structure function measurements and the sign of ξ_o must be independently determined (usually from the air-sea temperature difference). The function $F(\xi)$ is obtained from the dimensionless structure functions

$$F(\xi) = (1 + 0.5|\xi|^{2/3})*(1 - 7\xi)^{1/3} \quad ; \xi<0 \qquad (A3a)$$

$$F(\xi) = (1 + 2.5\xi^{2/3})^{1/2} \quad ; \xi>0 \qquad (A3b)$$

The scaling parameters are computed using (9)

$$u_* = [z^{2/3}C_u^2/f_u(\xi)]^{1/2} \qquad (A4a)$$

$$T_* = +/- [z^{2/3}C_T^2/f_T(\xi)]^{1/2} \qquad (A4b)$$

$$q_* = +/- [z^{2/3}C_q^2/f_T(\xi)]^{1/2} \qquad (A4c)$$

The sign of T_* is determined from the air-sea temperature difference and the sign of q_* is determined from the air-sea specific humidity difference (usually negative). The dimensionless structure functions are

$$f_u(\xi) = 4.0(1 + 0.5|\xi|^{2/3}),\ f_T(\xi) = 5.0(1 - 7\xi)^{-2/3} \quad ; \xi<0 \qquad (A5a)$$

$$f_u(\xi) = 4.0(1 + 2.5\xi^{2/3}),\ f_T(\xi) = 5.0(1 + 2.5\xi^{2/3}) \quad ; \xi>0 \qquad (A5b)$$

In the error analysis, we will use logarithmic derivatives of the similarity functions

$$\gamma_x(\xi) = (\xi/f_x(\xi))\ \partial f_x(\xi)/\partial\xi \qquad (A6)$$

From (A5) we obtain

$$\gamma_u(\xi) = 1/3|\xi|^{2/3}/(1 + 0.5|\xi|^{2/3}),\ \gamma_T(\xi) = 14/3\ \xi/(1 - 7\xi) \quad ; \xi<0 \qquad (A7a)$$

$$\gamma_u(\xi) = \gamma_T(\xi) = 2/3\ 2.5\ \xi^{2/3}/(1+2.5\xi^{2/3}) \quad ; \xi>0 \qquad (A7b)$$

Error Analysis

In this section we will examine the uncertainty of inertial-dissipation

fluxes in terms of the uncertainty in the measured variables. We use the standard error analysis approach (Fritschen and Gay, 1979) where the error is in some unspecified property G(x,y) is expressed in terms of errors δx and δy

$$\delta G = \partial G(x,y)/\partial x \; \delta x + \partial G(x,y) \; \delta y \tag{B1}$$

If x and y are independent variables and the errors in x and y are uncorrelated, then we express the most probable error as the sum of the squares of the individual terms

$$\delta G = [(\partial G/\partial x)^2 \delta x^2 + (\partial G/\partial y)^2 \delta y^2]^{1/2} \tag{B2}$$

Using (2) we express the fractional errors in the stress and sensible heat flux as

$$\delta \tau_o/\tau_o = 2 \; \delta u_*/u_* \tag{B3a}$$

$$\delta H_o/H_o = \delta u_*/u_* + \delta T_*/T_* \tag{B3b}$$

We cannot combine the terms as in (B2) because they are not independent. In order to evaluate (B3), we must do a similar expansion using (A4)

$$\delta x_*/x_* = 1/2 \; \delta C_x^2/C_x^2 - 1/2 \; \partial f_x/\partial \xi \; \delta \xi/f_x - 1/2 \; \delta f_x/f_x \tag{B4}$$

The second term on the right hand side of (B4) represents the error in x_* due to errors in estimating the stability parameter. The third term represents error due to uncertainty in the determination of the empirical similarity function. For the present analysis, we shall neglect the third term, which we believe to be quite small compared to the others. Using (A6) we can express (B4) as

$$\delta x_*/x_* = 1/2\ \delta C_x^2/C_x^2 - 1/2\ \gamma_x \delta\xi/\xi \qquad \text{(B5)}$$

where x=u,T, or q, as before. We now must evaluate $\delta\xi/\xi$ by expanding (3)

$$\delta\xi/\xi = (\delta T_* + 0.61\ T\ \delta q_*)/(T_* + 0.61\ T\ q_*) \ - 2\ \delta u_*/u_* \qquad \text{(B6)}$$

In (B6) we have assumed that the height of the measurement, the acceleration of gravity, the von Karman constant, and the mean air temperature are so well known that they do not contribute to the uncertainty. Substituting (B5) into (B6) and assuming that humidity flux makes a small contribution to the buoyancy flux (compared to the contribution of the temperature flux), we obtain

$$\delta\xi/\xi = [1/2\ \delta C_T^2/C_T^2 - \delta C_u^2/C_u^2\ ]/(1 - \gamma_u + 1/2\ \gamma_T\ ) \qquad \text{(B7)}$$

Since the errors in the measurements of the different structure functions are essentially uncorrelated, the most probable estimate of the uncertainty in the stability parameter is obtained using (B2)

$$\delta\xi/\xi = [1/4\ (\delta C_T^2/C_T^2)^2 + (\delta C_u^2/C_u^2)^2\ ]^{1/2}/(1 - \gamma_u + 1/2\ \gamma_T) \qquad \text{(B8)}$$

The uncertainty in the scaling parameters is found by using (B7) in (B5). Note that we use (B7) rather than (B8) because we must algebraically combine all common dependences before squaring the independent terms. The results for the scaling parameters are (where $\beta = 1-\gamma_u+1/2\gamma_T$)

$$\delta u_*/u_* = 1/2\ [(1 + 1/2\ \gamma_T)\delta C_u^2/C_u^2 - 1/2\ \gamma_u \delta C_T^2/C_T^2]/\beta \qquad \text{(B9a)}$$

$$\delta T_*/T_* = 1/2\ [\gamma_T \delta C_u^2/C_u^2 + (1 - \gamma_u)\delta C_T^2/C_T^2]/\beta \qquad \text{(B9b)}$$

$$\delta q_*/q_* = 1/2\ [\beta\delta C_q^2/C_q^2 + \gamma_T\delta C_u^2/C_u^2 - 1/2\ \gamma_T\delta C_T^2/C_T^2\ ]/\beta \qquad (B9c)$$

The uncertainty in the flux parameters is given by

$$\delta\tau_o/\tau_o = [(1 + 1/2\ \gamma_T)\delta C_u^2/C_u^2 - 1/2\ \gamma_u\delta C_T^2/C_T^2]/\beta \qquad (B10a)$$

$$\delta H_o/H_o = 1/2\ [(1 + 3/2\ \gamma_T)\delta C_u^2/C_u^2 + (1 - 3/2\ \gamma_u)\delta C_T^2/C_T^2]/\beta \qquad (B10b)$$

$$\delta E_o/E_o = 1/2\ [\beta\delta C_q^2/C_q^2 + (1 + 3/2\ \gamma_T)\delta C_u^2/C_u^2 - 1/2\ (\gamma_T + \gamma_u)\delta C_T^2/C_T^2]/\beta \qquad (B10c)$$

The most probable error is obtained by summing the squares of the individual terms in (B9) and (B10) as was done in (B8).

We can use (A7) to examine these results in the three stability limits. In near neutral conditions ($\xi \approx 0$), $\gamma_x \approx 0$ and $\beta \approx 1$, so the uncertainty in the stress is simply the uncertainty in C_u^2 while the uncertainty in the scalar heat fluxes is one half the combined uncertainty of C_u^2 and the appropriate scalar structure function parameter. In the limit of extreme stability ($\xi \approx \infty$), $\gamma_x \approx 2/3$ and $\beta \approx 2/3$. Under these conditions, the fractional uncertainty for stress more than doubles

$$\delta\tau_o/\tau_o = 2\ [\delta C_u^2/C_u^2 - 1/4\ \delta C_T^2/C_T^2] \qquad (B11a)$$

$$\delta H_o/H_o = 3/2\ \delta C_u^2/C_u^2 \qquad (B11b)$$

$$\delta E_o/E_o = 1/2\ [\delta C_q^2/C_q^2 + 3\ \delta C_u^2/C_u^2 - \delta C_T^2/C_T^2] \qquad (B11c)$$

Note that (B11b) implies that the accuracy of C_T^2 is of no relevance to the uncertainty of the sensible heat flux. This is a consequence of the extreme stable limit form of (B10), where the virtual temperature flux can be computed directly from the velocity structure function

$$\overline{w'T_o'} + 0.61\ T\ \overline{w'q_o'} \simeq (T/\kappa g)\ (C_u^2/10)^{3/2} \qquad (B12)$$

Individually the heat fluxes can be computed as

$$\overline{w'T'_o} = (C_u^2/10)^{3/2}(T/\kappa g)/[1 + 0.61\ T\ (C_q^2/C_T^2)^{1/2}] \qquad \text{(B13a)}$$

$$\overline{w'q'_o} = (C_u^2/10)^{3/2}(T/\kappa g)/[(C_T^2/C_q^2)^{1/2} + 0.61\ T\ ] \qquad \text{(B13b)}$$

Since we have neglected the second term (the humidity contribution to the surface buoyancy flux, which is about 20%) in the right most denominator in our error analysis, we obtained the results of (B11).

The convective limit ($\xi \simeq -\infty$, $\gamma_u \simeq 2/3$, and $\gamma_T \simeq -2/3$) is somewhat more tricky because the parameter β, which is the denominator in (B9), approaches zero. For stress this implies that the fractional uncertainty approaches infinity. This is a consequence of the convective limit of Monin-Obukhov similarity, where u_* becomes irrelevant. Therefore, u_* cannot be estimated using similarity theory from measurements made in this limit. Since the convective limit is normally associated with very light winds, u_* will be small and a large fractional error in a small parameter is to be expected. For the scalar fluxes, both the denominator and the numerator approach zero. Here the results will depend on the particular method used to compute the heat flux and ξ. In the convective limit, the scalar fluxes can be represented by (again neglecting the humidity contribution to the buoyancy flux)

$$\overline{w'T'_o} = z\ (C_T^2/5)^{3/4}\ (7\kappa g/T)^{1/2} \qquad \text{(B14a)}$$

$$\overline{w'q'_o} = z\ (C_q^2/5)^{1/2}(C_T^2/5)^{1/4}(7\kappa g/T)^{1/2} \qquad \text{(B14b)}$$

The errors in the heat fluxes become

$$\delta H_o/H_o = 3/4\ \delta C_T^2/C_T^2 \qquad \text{(B15a)}$$

$$\delta E_o/E_o = 1/2\ \delta C_q^2/C_q^2 + 1/4\ \delta C_T^2/C_T^2 \qquad \text{(B15b)}$$

These limiting forms of the errors (B15) can be obtained from (B10) by noting that γ_T approaches its convective limit value of -2/3 much faster than γ_u reaches its limit.

From the preceding analysis, it is clear that the uncertainties in the fluxes computed by the inertial-dissipation method are on the order of the uncertainties in the measured structure function parameters. The uncertainties are largest in very stable regimes, except for stress, which becomes small but fractionally more uncertain in convective conditions. Of course we can always examine the uncertainty in inertial-dissipation flux estimates by comparing them with covariance estimates, but the preceding analysis has the advantage that it spells out the stability dependence of the errors and is not confused by uncertainty in the covariance estimates.

In order to apply the analysis, we must know the uncertainties in the measured structure functions. For example, consider the velocity structure function determined from spectral analysis

$$C_u^2 = 4\ (2\pi/u)^{2/3}\ f^{5/3} s^2\ S_V(f) \qquad \text{(B16)}$$

where $s=(\partial u/\partial V)$ is the inverse voltage sensitivity of the velocity sensor and S_V is the voltage variance spectrum. We could then estimate the error in C_u^2 by subjecting (B16) to the same error analysis process as before. From the HEXMAX experiment we also have considerable empirical evidence about the uncertainties in the measurements. For example, the spectral estimates of C_u^2 were about 20% higher than the direct dissipation estimates but they were about 20% lower than the filter-variance estimates. From that we conclude that our spectral measurements of C_u^2 are probably uncertain by

no more than 20%, which is consistent with the comparison with the covariance measurements. By comparing q_* values from the boom and the mast, we conclude that out C_q^2 measurements are uncertain by about 30%. This greater inaccuracy is due to the sensitivity variations of the Lyman-α.

The uncertainties in the fluxes are graphically illustrated in Fig. B1 for (B10) using the above estimates of the fractional errors in the structure functions such that

$$\delta C_u^2/C_u^2 = 0.2 \tag{B17a}$$

$$\delta C_T^2/C_T^2 = 0.3 \tag{B17b}$$

$$\delta C_q^2/C_q^2 = 0.3 \tag{B17c}$$

This figure is consistent with the analysis of (A7), where the uncertainties in the scalar fluxes are shown to be largest in the stable regime. The uncertainty in stress also behaves as expected in this figure, demonstrating that under very stable conditions (ξ=20) the fractional error in C_u^2 of approximately 0.4 is double the neutral value of 0.2. Under very unstable conditions the fractional error in C_u^2 quickly becomes very large. This is again due to the fact that u_* is small and highly variable in this convective regime, causing it to become irrelevant as a velocity scale under these conditions.

REFERENCES

Andreas, Edgar L., 1987: On the Kolmogorov constants for the temperature-humidity cospectrum and the refractive index spectrum. J. Atmos. Sci., 44, 2399-2406.

Anderson, R.J. and S.D. Smith, 1981: Evaporation coefficient for the sea surface from eddy-flux measurements. J. Geophys. Res., 86, 449-456.

Beecher, E.A., 1988: Analysis of temperature and velocity microturbulence parameters from aircraft data and relationship to atmospheric refractive index. M.S. Thesis, Department of Meteorology, Pennsylvania State University, University Park, PA, 16802, 167 pp.

Blanc, T.V., 1985: Variation of bulk-derived surface flux, stability, and roughness results due to the use of different transfer coefficient schemes. J. Phys. Ocean., 15, 650-669.

Blanc, T.V., 1987: Accuracy of bulk-method-determined flux, stability, and sea surface roughness. J. Geophys. Res., 92, 3867-3876.

Buck, Arden L., 1976: The variable path Lyman-alpha hygrometer and its operating characteristics. Bull. Am. Met. Soc., 57, 1113-1118.

Buck, Arden L., 1983: The Lyman-alpha absorption technique for fast humidity measurement. Proc. 5th AMS Symposium on Meteorological Observations and Instruments. April 11-15, Toronto, Canada, 16-20.

Buck, Arden L., 1985: The Lyman-alpha absorption hygrometer. Moisture and Humidity, 1985. Instrument Society of America, Research Triangle Park, NC, 411-436.

Champagne, F.H., C.A. Friehe, J.C. LaRue, and J.C. Wyngaard, 1977: Flux

measurements, flux estimation techniques and fine-scale turbulence measurements in the unstable surface layer over land. J. Atmos. Sci., 34, 515-530.

Davidson, K.L, T. Houlihan, C.W. Fairall, and G.E. Schacher, 1978: Observations of C_T^2 over the ocean. Bound.-Layer Meteor., 15, 507-523.

Dyer, A.J., and B.B. Hicks, 1982: Kolmogorov constants at the 1976 ITCE. Bound.-Layer Meteorol., 22, 137-150.

Edson, J.B., C.W. Fairall, P.G. Mestayer, and S.E. Larsen, 1989: Inertial-dissipation air-sea flux measuremnents II: Evaluation of the method from HEXMAX. J. Atmos. Ocean. Tech., this issue.

Fairall, C.W., K.L. Davidson, and G.E. Schacher, 1979: Humidity effects and sea salt contamination of atmospheric temperature sensors. J. Appl. Meteor., 18, 1237-1239.

Fairall, C.W., G.E. Schacher, and K.L. Davidson, 1980: Measurements of the humidity structure function parameters C_T^2 and C_{Tq} over the ocean. Bound.-Layer Meteor., 19, 81-92.

Fairall, C.W., and S.E. Larsen, 1986: Inertial dissipation methods and turbulent fluxes at the air ocean interface. Bound.-Layer Meteorol., 34, 287-301.

Fairall, C.W., and R.M. Markson, 1987: Mesoscale variations in surface stress, heat fluxes, and drag coefficient in the marginal ice zone during the 1983 Marginal Ice Zone Experiment. J. Geophys. Res., 92, 6921-6932.

Friehe, C.A., and K.F. Schmitt, 1976: Parameterization of air-sea interface fluxes of sensible heat and moisture by the bulk aerodynamic formulas. J. Phys. Oceanogr., 6, 801-809.

Fritschen, L.J., and L.W. Gay, 1979: Environemental Instrumentation,

Springer-Verlag, New York.

Garratt, J.R., 1977: Review of drag coefficients over oceans and continents. Mon. Wea. Rev., 105, 915-929.

Geernaert, G.L., K.B. Katsaros, and K. Richter, 1986: Variation of the drag coefficient and its dependence on sea state. J. Geophys. Res., 91, 7667-7679.

Guest, P.S., and K.L. Davidson, 1987: The effect of observed ice conditions on the drag coefficient in the summer East Greenland Sea marginal ice zone. J. Geophys. Res., 92, 6943-6954.

Hill, Reginald J., 1988: Implications of Monin-Obukhov similarity theory for scalar quantities. J. Atmos. Sci., to appear.

In de Maur, G., 1977: Stromingsonderzoek in een windtunnel ten hehoeve van de installatie van windmeetinstrumenten op de Meetpost Noordwijk. Royal Ducth Meteorological Institute (KNMI) technical report NLR TR 76140 L, De Bilt, the Netherlands, 29 pp.

Katsaros, K.B., S.D. Smith and W.A. Oost, 1987: HEXOS-Humidity Exchange Over the Sea. A program for research on water vapor and droplet fluxes from sea to air at moderate and high wind speeds. Bull. Am. Met. Soc., 68, 466-476.

Khalsa, S.J.S., and J.A. Businger, 1977: The drag coefficient as determined by the dissipation method and its relation to intermittent convection in the surface layer. Bound.-Layer Meteor., 12, 273-297.

Large, W.G., and S. Pond, 1981: Open ocean momentum flux measurements in moderate to strong winds. J. Phys. Oceanogr., 11, 324-336.

Large, W.G., and S. Pond, 1982: Sensible and latent heat flux measurements over the ocean. J. Phys. Oceanogr., 12, 464-482.

Large, W.G., and J.A. Businger, 1988: A system for remote measurements of wind

stress over the ocean. J. Atmos. Oceanic Tech., 5, 274-285.

Larsen, S.E., J. Hojstrup, and C.H. Gibson, 1980: Fast-response temperature sensors. Air-Sea Interaction, F. Dobson and R. Davis, Eds., Plenum, 269-291.

Larsen, S.E., and J. Hojstrup, 1982: Spatial and temporal resolution of a thin wire resistance thermometer. J. Phys. E: Sci. Intrum., 15, 471-477.

Larsen, S.E., C.W. Fairall, J.B. Edson, and P.G. Mestayer, 1989: The correction of sonic anemometer temperature variance spectra for velocity structure function crosstalk. J. Atmos. Oceanic Tech., submitted.

Ling, S.C., T.W. Kao, M. Asce, and A. Saad, 1980:Microdroplets and transport of moisture from the ocean. J. Eng. Mech. Div., 6, 1327-1339.

Mestayer, P.G., and C. Rebattet, 1985: Temperature sensitivity of Lyman-alpha hygrometers. J. Atmos. Oceanic Tech., 2, 656-664.

Mestayer, P.G., C. Rebattet, and F. Goutail, 1986: An improved Lyman-alpha hygrometer. Part I: Miniturizing the sample volume. Rev. Sci. Instrum., 57, 20- .

Mestayer, P.G., F. Goutail and C. Rebattet, 1987: An improved Lyman-alpha hygrometer. Part II: Playing with ourself at government expense. Rev. Sci. Instrum., 58, 2165- .

Mestayer, P.G., F. Goutail, and S.E. Larsen, 1988: An improved Lyman-alpha hygrometer. Part III: Performance of the 'platform' model for small scale atmospheric measurements in the open sea. Rev. Sci. Instrum., to appear.

Mortensen, N.G., S.E. Larsen, I. Troen, and T Mikkelsen, 1987: Two years worth of turbulence data recorded by a sonic anemometer based data acquistion system. Proc. 6th AMS Symposium on Meteorological Observations and Measurements. June 12-16, New Orleans, LA, 393-397.

Panofsky, H.A. and J.A. Dutton, 1984: Atmospheric Turbulence, Wiley-Interscience, New York, 397 pp.

Pond, S., G.T. Phelps, J.E. Paquin, G. McBean, and R.W. Stewart, 1971: Measurements of the turbulent fluxes of momentum, moisture, and sensible heat over the ocean. J. Atmos. Sci., 28, 901-917.

Schacher, G.E., K.L., Davidson, T.M. Houlihan, and C.W. Fairall, 1981: Measurements of the rate of dissipation of turbulent kinetic energy over the ocean. Bound.-Layer Meteor., 20, 321-330.

Schmitt, K.F., C.A. Friehe, and C.H. Gibson, 1978: Humidity sensitivity of atmospheric temperature sensors by salt contamination. J. Phys. Oceanogr., 8, 141-161.

Schotanus, P., F.T.M. Nieuwstadt, and H.A.R. Bruin, 1983: Temperature measurement with a sonic anemometer and its application to heat and moisture fluxes. Bound.-Layer Meteorol., 26, 81-93.

Smith, S.D., 1980: Wind stress and heat flux over the ocean in gale force winds. J. Phys. Oceanogr., 10, 709-726.

Tanner, C.B., and G.W. Thurtell, 1969: Anemoclinometer measurements of Reynolds stress and heat transport in the atmospheric surface layer. University of Wisconsin Technical report ECOM-66-G22-F, 82 pp

Wesely, M.A., 1976: The combined effects of temperature and humidity fluctuations on refractive index. J. Appl. Meteor., 15, 43-49.

Wills, J.A.B., 1984: HEXOS Model Tests on the Noordwijk Tower. Report R184, British Maritime Technology, Teddington, Middlesesx TW11 OJJ, U.K., 53 pp.

Wyngaard, J.C., 1974: On surface-layer turbulence. Workshop on Micrometeorology, edited by D. Haugen, AMS, Science Press, 101-149.

Wyngaard, J.C., 1981: The effects of probe-induced flow distortion on

atmospheric turbulence measurements. J. Appl. Meteorol., 20, 784-794.

Table 1. Listing and classification of HEXMAX Inertial-dissipation group sensors.

Boom Sensors

Classification	Measured Signal	Manufacturer (Model)
1. Sonic Anemometer	u, v, w, T	Kaijo-Denke (DAT-300)
4. Hot Wire	u'	DISA (P11)
5. Cold Wire	T'	DISA (P31)
2. Fast Hygrometer	ρ_{vapor}	IMST/SA
3. Slow Hygrometer	T_{dew}	EG&G (156A)

Mast Sensors

Classification	Measured Signal	Manufacturer (Model)
6. Sonic Anemometer	u, v, w, T	Kaijo-Denke (DAT-300)
9. Hot Film	u'	TSI (1210)
7. Fast Hygrometer	ρ_{vapor}	PSU/RISØ
8. Slow Hygrometer	T_{dew}	EG&G (156A)

Additional Sensors

Classification	Measured Signal
10. Thermistor	T_{air} (Mast Level)
11. Thermistor	T_{water}

Table 2. Component listing of Hewlett Packard (HP) computer system.

Description	Model Number
Computer	HP 217
Video	HP 35721A
Dual Disc Drive	HP 9122D
Keyboard	HP 46010A
Video Card	HP 98204B
2mb Memory Card	Infotek AM220
Processor Card	Infotek FP210
A/D Card	Infotek AD200
FFT Card	Ariel 523
Basic 3.0	HP 98611,98612
Printer	HP 2934A

Table 3. Data aquisition listing of 8 fast and 9 slow data channels.

Fast Channels

Signal	Instrument
1. T	Boom cold-wire
2. u	Boom hot-wire
3. ρ_v	Boom IMST/SA lyman-alpha
4. u vector	Boom sonic $\sqrt{(u^2+ v^2)}$
5. T	Boom sonic temperature
6. ρ_v	Mast PSU/RISØ lyman-alpha
7. u vector	Mast sonic $\sqrt{(u^2+ v^2)}$
8. T	Mast sonic temperature

Slow Channels

Signal	Instrument
1. $\partial u/\partial t$	Boom hot-wire
2. T_d	Boom EG&G dewpointer
3. u_{rms}	Mast hot-film RMS
4. V mean	Mast hot-film mean voltage
5. T_d	Mast EG&G dewpointer
6. u mean	Boom sonic $\sqrt{(u^2+ v^2)}$
7. u mean	Mast sonic $\sqrt{(u^2+ v^2)}$
8. T mast	Mast thermistor
9. T sea	Submerged thermistor

Table 4. Printout of the HEXMAX data record corresponding to the spectra shown in Figures 5a through 5h.

HEXMAX EXPERIMENT HEXIST GROUP
29 Oct 1986 START GMT: 20:53:29 END GMT: 21:03:03 LENGTH: 10.0(min) REC# 370

**********BOOM**********
SONIC WIND: MEAN= 7.20 SIGMA= .75
EG&G#1: Td MN= 6.16 RH= 69 Td SIG= .416 Q MN= 5.88 Q SIG= .155
HW SENS= 11.0 B COEF= 4.9
EPSILON HOT WIRE= 1.3E-02 NEUT U*= .33 Cd(10)= 1.93E-03
LYMAN SENS: MEAS= 3.4

**********MAST**********
SEA TEMP= 11.98 AIR TEMP= 11.59 Q SEA= 8.71
SONIC WIND: MEAN= 9.22 SIGMA= .63
HOT FILM VOLT: MEAN= 9.24 SIGMA= .120 FILT RMS= .014 B COEF= 21.4
EPSILON HOT FILM= 3.9E-03 NEUT U*= .34 Cd(10)= 1.61E-03
EG&G#2: Td MN= 4.76 RH= 63 Td SIG= .498 Q MN= 5.34 Q SIG= .186
LYMAN SENS: CALC= 3.3 MEAS= 2.3

**********FAST DATA**********

CH	STATUS	GAIN	SIGNAL	MEAN	FST_RMS	SLO_RMS	Cx^2	EPS,CHI
1	1	2.0	Tdeat_bm	-.58	.0870	.081	1.48E-02	2.16E-03
2	1	2.0	Uhw_bm	-.31	.0202	.068	1.24E-01	1.54E-02
3	1	3.0	Lym_bm	.43	.0127	.046	5.50E-03	8.04E-04
4	1	.2	Uson_bm	-1.59	.1932	.703	1.15E-01	1.37E-02
5	1	1.0	Tson_bm	.90	.0624	.070	4.90E-03	7.16E-04
6	1	2.0	Lym_ms	1.22	.0118	.081	3.99E-03	3.92E-04
7	1	1.0	Uson_ms	.29	.1276	.615	4.76E-02	3.67E-03
8	1	1.0	Tson_ms	1.34	.1401	.078	1.84E-02	1.80E-03
9	1	1.0	BOOM DOWN					
10	1	1.0	MAST UP					

**********SCANNER DATA**********

CH	STATUS	GAIN	SIGNAL	MEAN	RMS
11	0	1.0	Tder_bm	.002	.00001
12	1	1.0	Uder_bm	.046	.00096
13	1	1.0	Td_bm	2.834	.02067
14	1	5.0	Urms_ms	.014	.00056
15	1	.3	Vhf_ms	9.237	.12021
16	1	1.0	Td_ms	2.765	.02473
17	1	.2	Umean_bm	7.203	.74687
18	1	.1	Umean_ms	9.219	.63024
19	1	1.0	Tsea	.544	.00111
20	1	1.0	Tmast	.555	.00073

FIGURE CAPTIONS

Fig. 1. The instrumental setup on the Meetpost Noordwijk (MPN) for the HEXOS Main Experiment (HEXMAX) showing the boom and mast locations.

Fig. 2. The experimental packages located on the boom (top photo) and mast (bottom photo) during HEXMAX. Sensors are described in the text.

Fig. 3. On the left, the configuration for the boom mounted Kaijo-Denke model DAT-300 sonic anemometer/thermometer, consisting of an asymmetrical TR-61A type probe. On the right, the configuration for the mast mounted Kaijo-Denke model DAT-300 sonic anemometer/thermometer, consisting of a symmetrical TR-61B strong wind type probe.

Fig. 4. System architecture of the inertial-dissipation data acquisition system used during HEMAX. Subscripts: hw hot-wire, cw cold-wire, s sonic, hf hot-film.

Fig. 5a. Boom cold-wire temperature variance spectrum, where the label Tdeat_bm indicates the use of a Deaton temperature bridge. The spectral density (for Figs. 5a-5h) is in physical units (e.g., K^2Hz^{-1} for temperature). The dashed line indicates an inertial subrange form ($f^{-2/3}$) with the value of the structure function indicated in the upper right hand corner.

Fig. 5b. As in Fig. 5a but for the boom hot-wire velocity variance spectrum, using the boom sonic anemometer velocity variance for calibration.

Fig. 5c. As in Fig. 5a but for the boom Lyman-α specific humidity variance spectrum, using an EG&G dew point device variance for calibration. An improved calibration technique was used in post-processing.

Fig. 5d. As in Fig 5a but for the boom sonic anemometer velocity variance spectrum. The velocity signal is taken from a vector box which outputs $\sqrt{(u^2+ v^2)}$ from the sonic u and v components.

Fig. 5e. As in Fig. 5a but for the boom sonic temperature variance spectrum.

Fig. 5f. As in Fig. 5a but for the mast Lyman-α specific humidity variance spectrum, using a laboratory determined calibration equation to convert to physical units.

Fig. 5g. As in Fig. 5a but for the mast sonic anemometer velocity variance spectrum. The velocity signal is taken from a vector box which outputs $\sqrt{(u^2+ v^2)}$ from the sonic u and v components.

Fig. 5h. As in Fig. 5a but for the mast sonic temperature variance spectrum.

Fig. 6. Variance spectrum of fluctuations in the velocity derivative, $\partial u/\partial t$, using the boom hot-wire signal and a Nyquist frequency of 5000 Hz. Since we are using an f*S(f) plotting format, this graph is equivalent to f^3 times the velocity variance spectrum (a factor of f^2 comes from the derivative process). The inertial subrange appears as the $f^{4/3}$ slope on the left portion of the curve.

Fig. 7a. Comparison of the spectral and derivative estimates of $\log(\epsilon)$. The derivative value is computed using (4), while the spectral estimate is the average value of ϵ calculated between 10 and 20 Hz using (6) and (8a). The tendency for relatively smaller derivative estimates as ϵ increases is probably due to loss of frequency response of the hot-wire sensor due to salt contamination.

Fig. 7b. Comparison of friction velocity estimates from the inertial-dissipation (spectral) and direct dissipation (derivative) techniques using the boom hot-wire.

Fig. 8. Comparison of friction velocity estimates from the inertial-dissipation and filtered-variance techniques using the mast sonic anemometer and mast hot-film, respectively.

Fig. 9a. The dimensionless velocity structure function parameter as a function of stability. f_u is determined from the boom sonic spectral values of C_u^2 and sonic covariance estimates of u_* and z/L.

Fig. 9b. As in 9a but f_u is determined from the boom hot-wire spectral values of C_u^2 and sonic covariance estimates of u_* and z/L.

Fig. 10a. Comparison of estimates of the temperature scaling parameter, $T_*=-\langle w'T'\rangle/u_*$, using the sonic temperature, sonic vertical velocity covariance (vertical axis) versus using the cold-wire temperature, sonic vertical velocity covariance (horizontal axis).

Fig. 10b. As in Fig. 10a but the horizontal axis is T_* computed using the cold-wire inertial-dissipation value.

Fig. 11. Sample low frequency variance spectra taken during HEXMAX: Sonic temperature spectrum (solid line), cold-wire temperature spectrum (dashed line) and specific humidity spectrum (dotted line). The humidity spectrum has been renormalized to match the sonic temperature spectrum at 0.1 Hz.

Fig. 12a. A time series of stress estimates using the bulk (asterisks), inertial-dissipation (circles), and covariance (solid line) methods for a two week period during the 1986 HEXMAX experiment. The covariance and inertial-dissipation estimates are from the boom sensors.

Fig. 12b. A time series of latent heat estimates using the bulk (asterisks), inertial-dissipation (circles), and covariance (solid line) techniques for a two week period during the 1986 HEXMAX experiment.

Fig. 13a. Comparison of estimates of the velocity scaling parameter, u_*, using the sonic u'w' covariance versus the sonic anemometer inertial-

dissipation value.

Fig. 13b. Comparison of estimates of the specific humidity scaling parameter, q_*, using the sonic anemometer, Lyman-α $\langle w'q' \rangle$ covariance versus the Lyman-α inertial-dissipation value.

Fig. 14. Comparison of Lyman-α (broken line) and Infrared (solid line) hygrometer latent heat flux calculations for a two day period during March 1988 at the Rock Springs experimental site in central Pennsylvania. The covariance technique is used where both hygrometers are paired with the same sonic anemometer.

Fig. B1. The fractional error as a function of stability using the square of the sum of the squares of the individual terms in (10) for stress (solid line), sensible heat flux (broken line), and latent heat flux (dashed line). These curves are computed assuming fractional measurement errors in the structure functions of 20% for velocity and 30% for temperature and humidity.

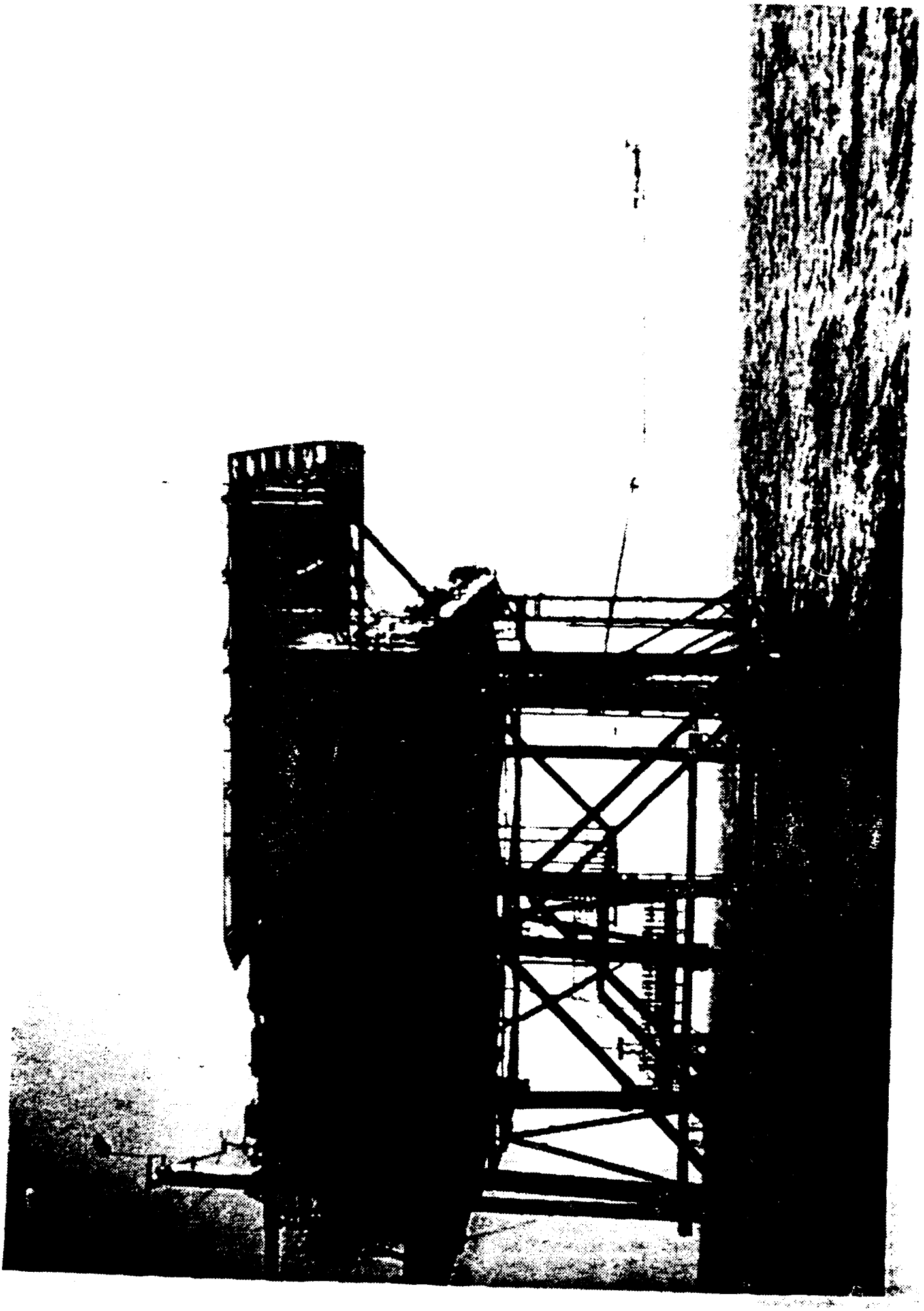

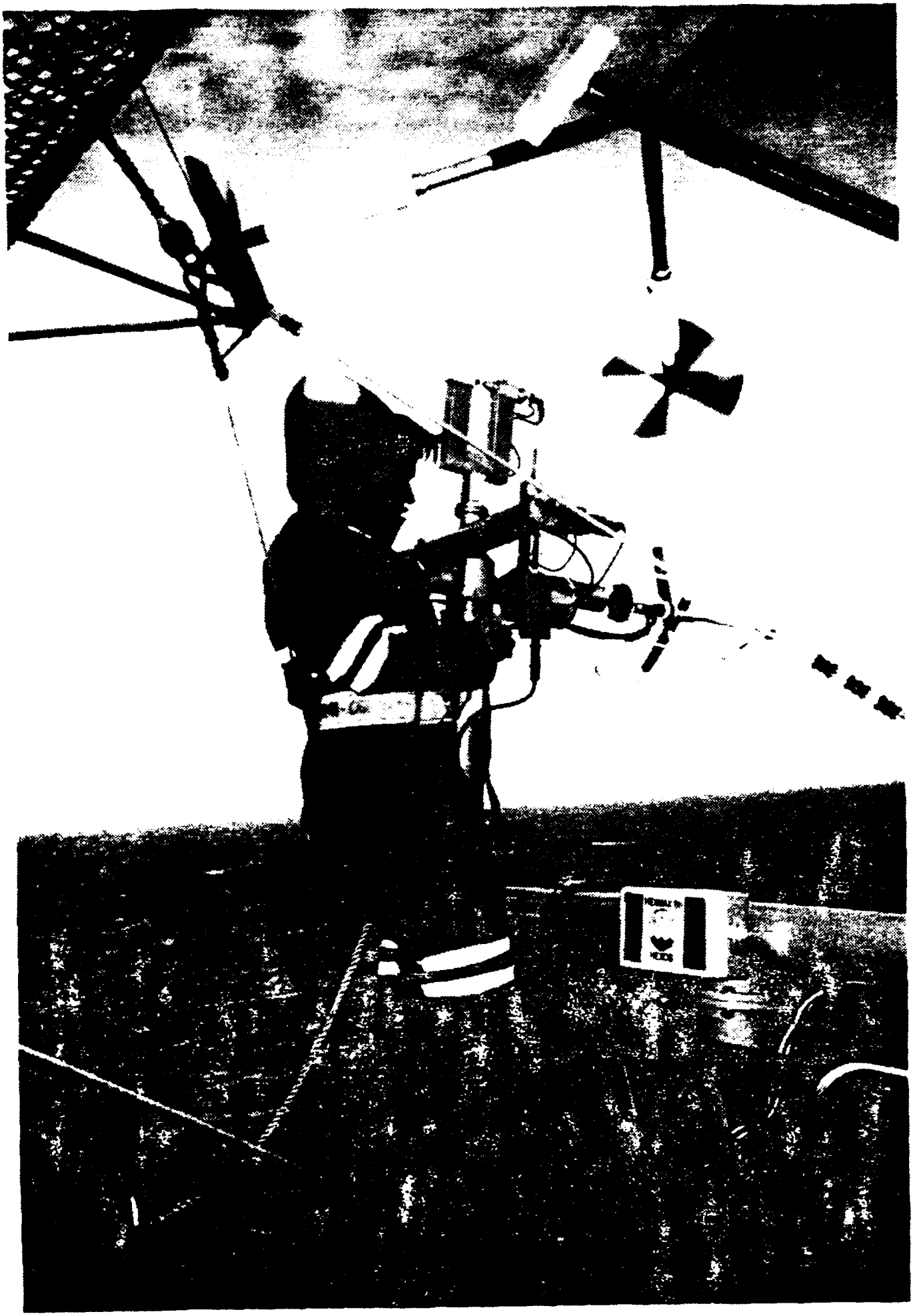

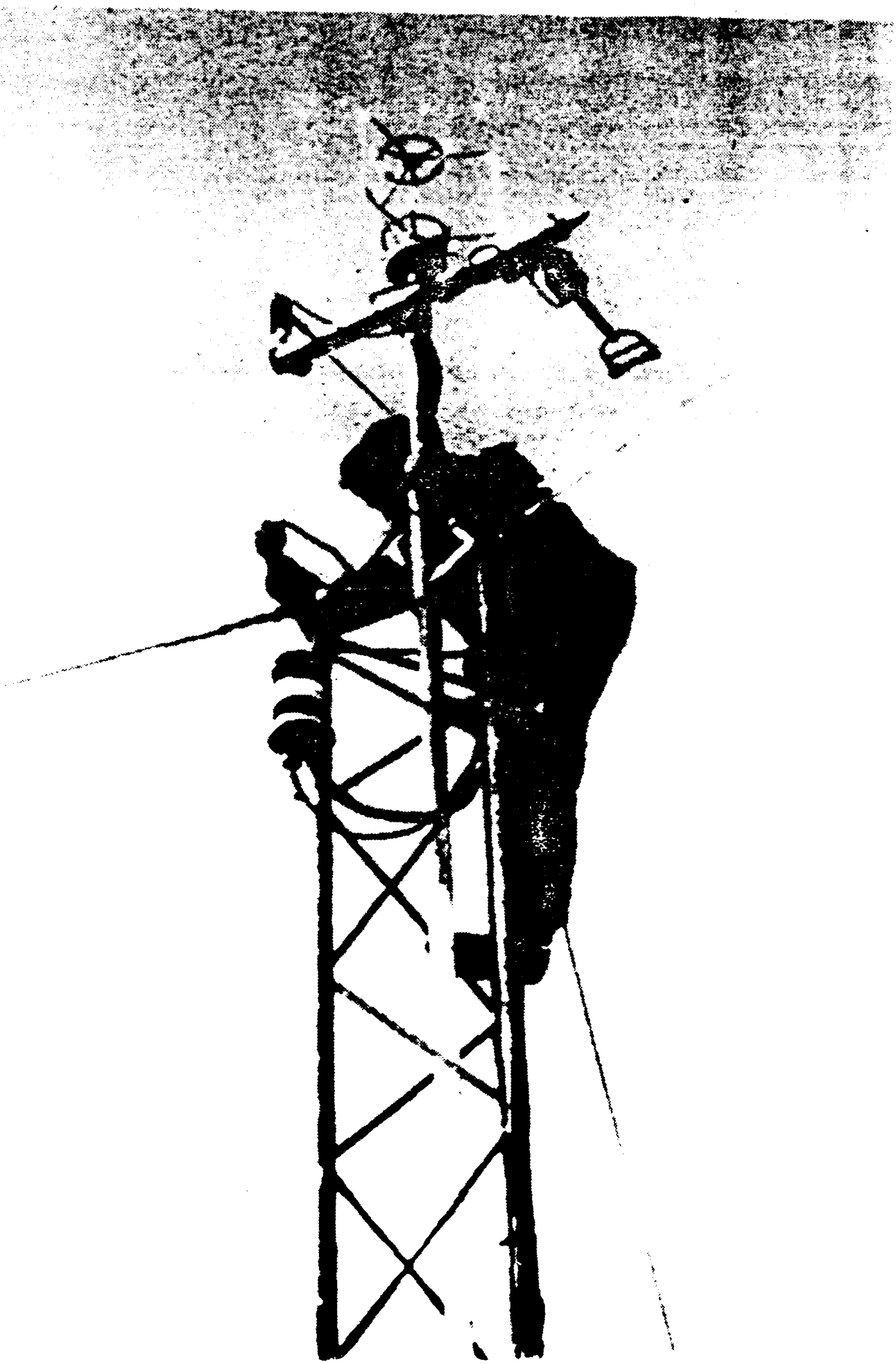

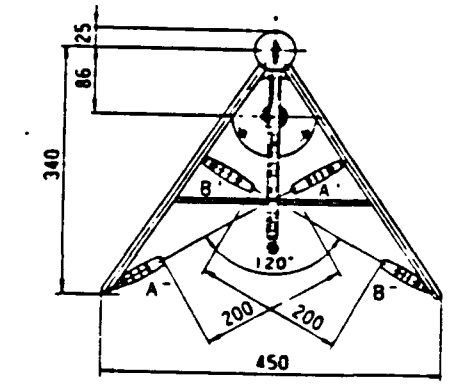
25
86
340
B
A
120°
A
200
200
B
450

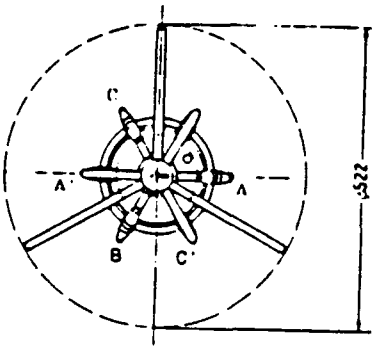
C
A
B
C
A
322

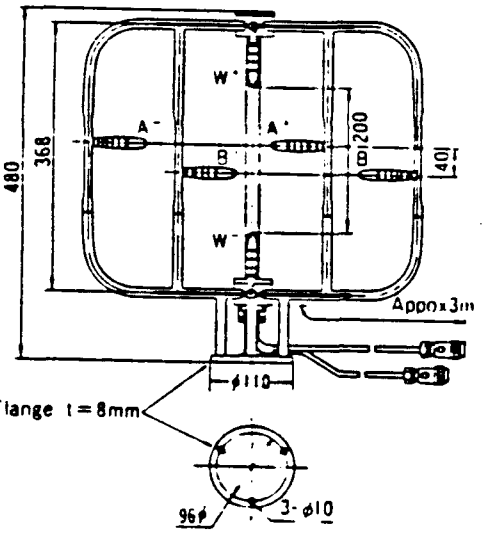
W
A
A
B
W
200
40
480
368
Approx 3m
φ110
Flange t = 8mm
96φ
3-φ10

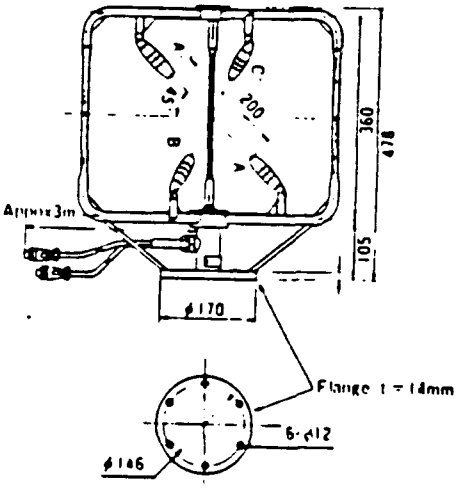
C
B
A
200
360
418
105
Approx 3m
φ170
Flange t = 14mm
6-φ12
φ146

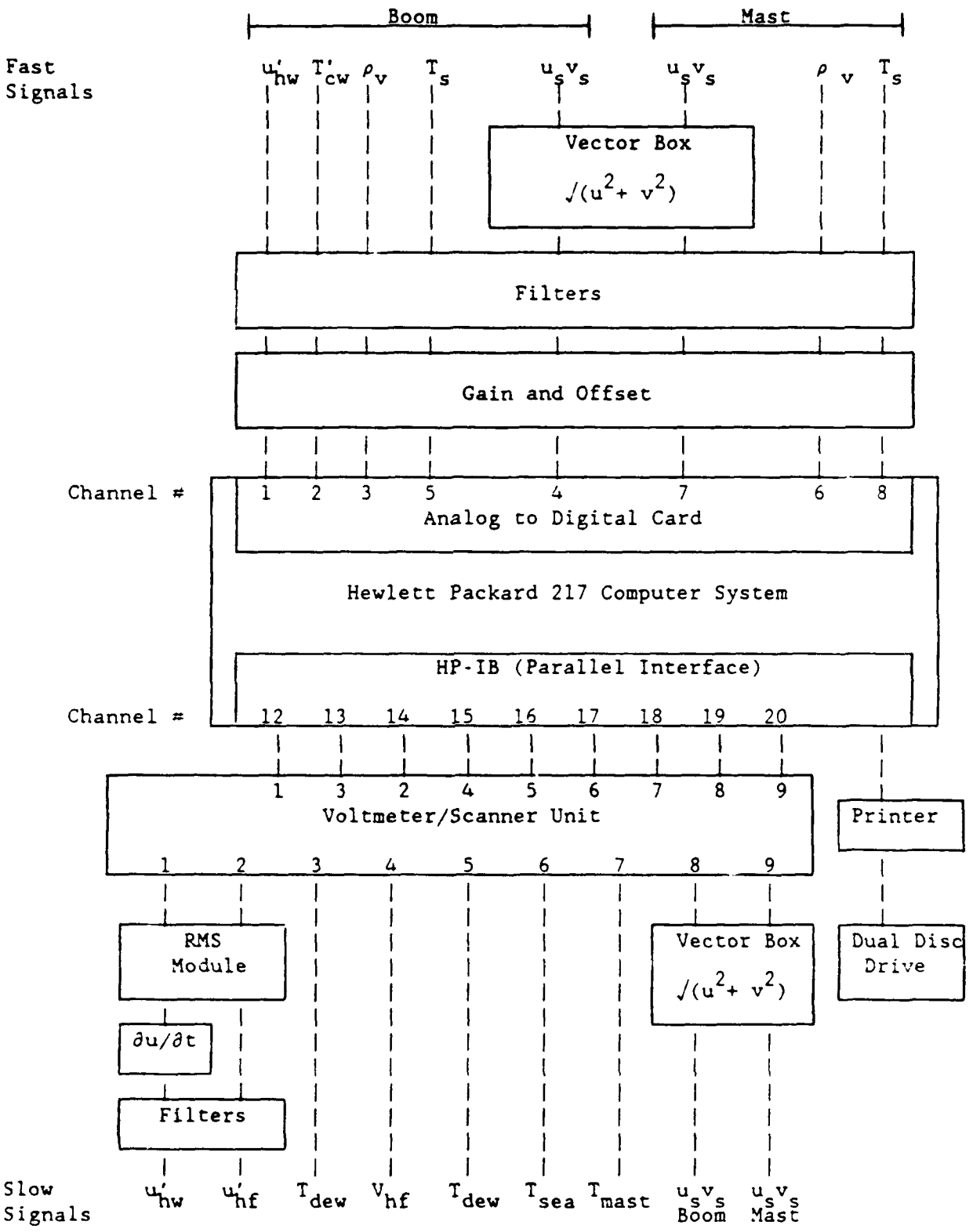
Boom
Mast
Fast Signals
u'_{hw} T'_{cw} ρ_v T_s $u_s v_s$ $u_s v_s$ ρ_v T_s
Vector Box
$\sqrt{(u^2+v^2)}$
Filters
Gain and Offset
Channel #
1 2 3 5 4 7 6 8
Analog to Digital Card
Hewlett Packard 217 Computer System
HP-IB (Parallel Interface)
Channel #
12 13 14 15 16 17 18 19 20
1 3 2 4 5 6 7 8 9
Voltmeter/Scanner Unit
Printer
1 2 3 4 5 6 7 8 9
RMS Module
Vector Box
$\sqrt{(u^2+v^2)}$
Dual Disc Drive
$\partial u/\partial t$
Filters
Slow Signals
u'_{hw} u'_{hf} T_{dew} V_{hf} T_{dew} T_{sea} T_{mast} $u_s v_s$ Boom $u_s v_s$ Mast

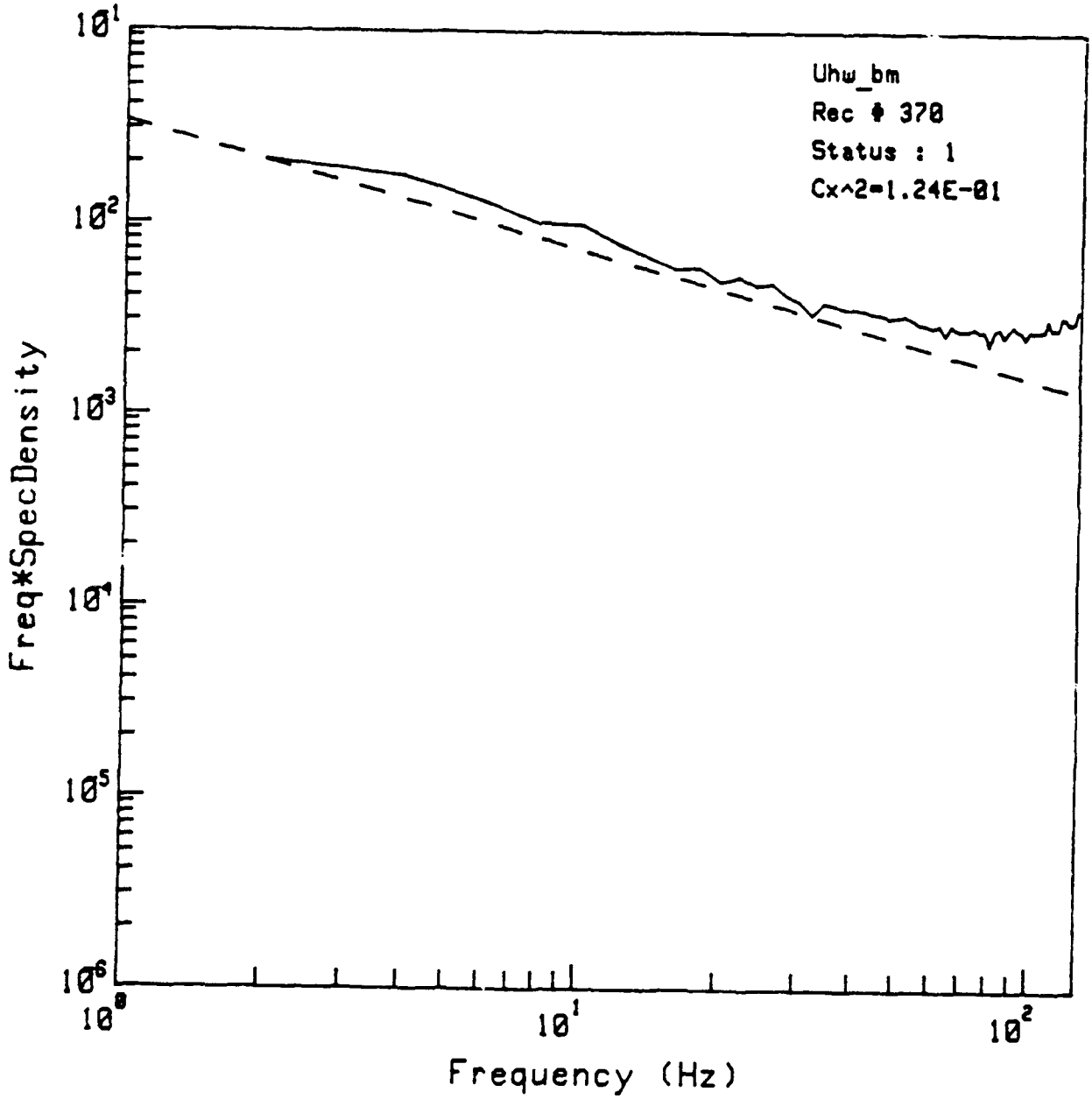
Uhw_bm
Rec # 370
Status : 1
Cx^2=1.24E-01
Freq*SpecDensity
Frequency (Hz)
10^1
10^2
10^3
10^4
10^5
10^6
10^0
10^1
10^2

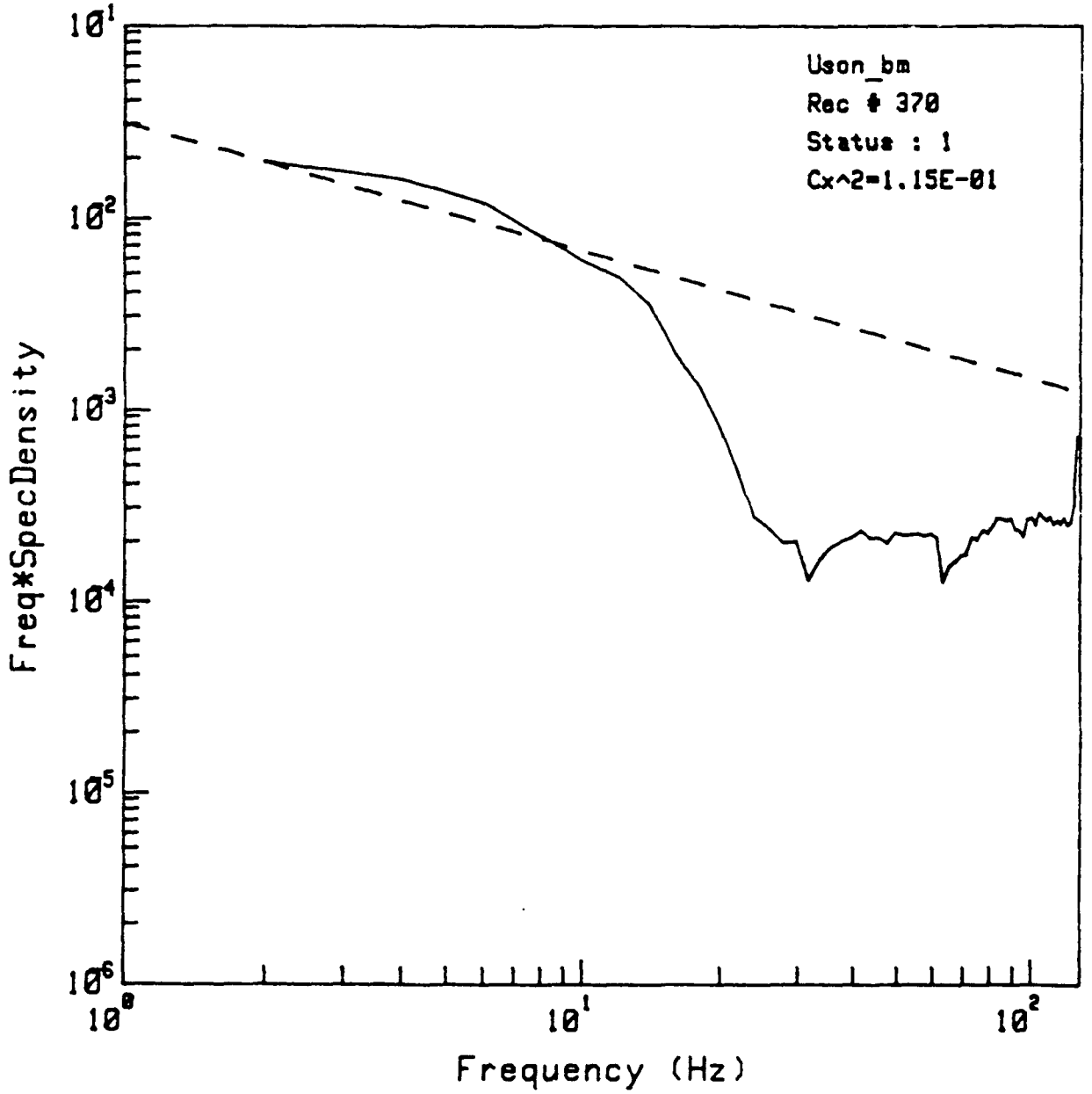
Uson_bm
Rec # 370
Status : 1
Cx^2=1.15E-01
Freq*SpecDensity
Frequency (Hz)
10^1
10^2
10^3
10^4
10^5
10^6
10^0
10^1
10^2

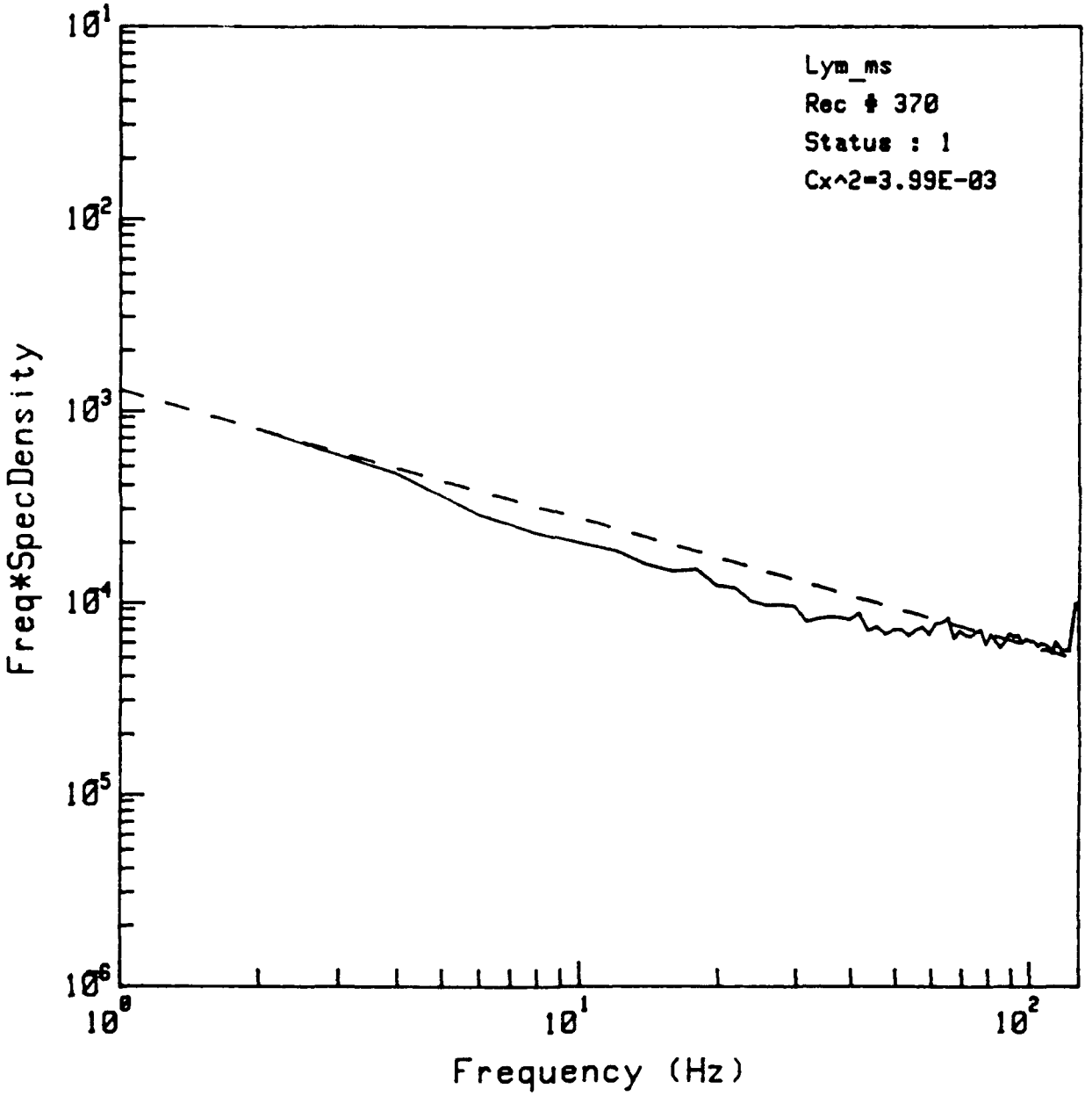
Lym_ms
Rec # 370
Status : 1
Cx^2=3.99E-03
Freq*SpecDensity
Frequency (Hz)
10^1
10^2
10^3
10^4
10^5
10^6
10^0
10^1
10^2

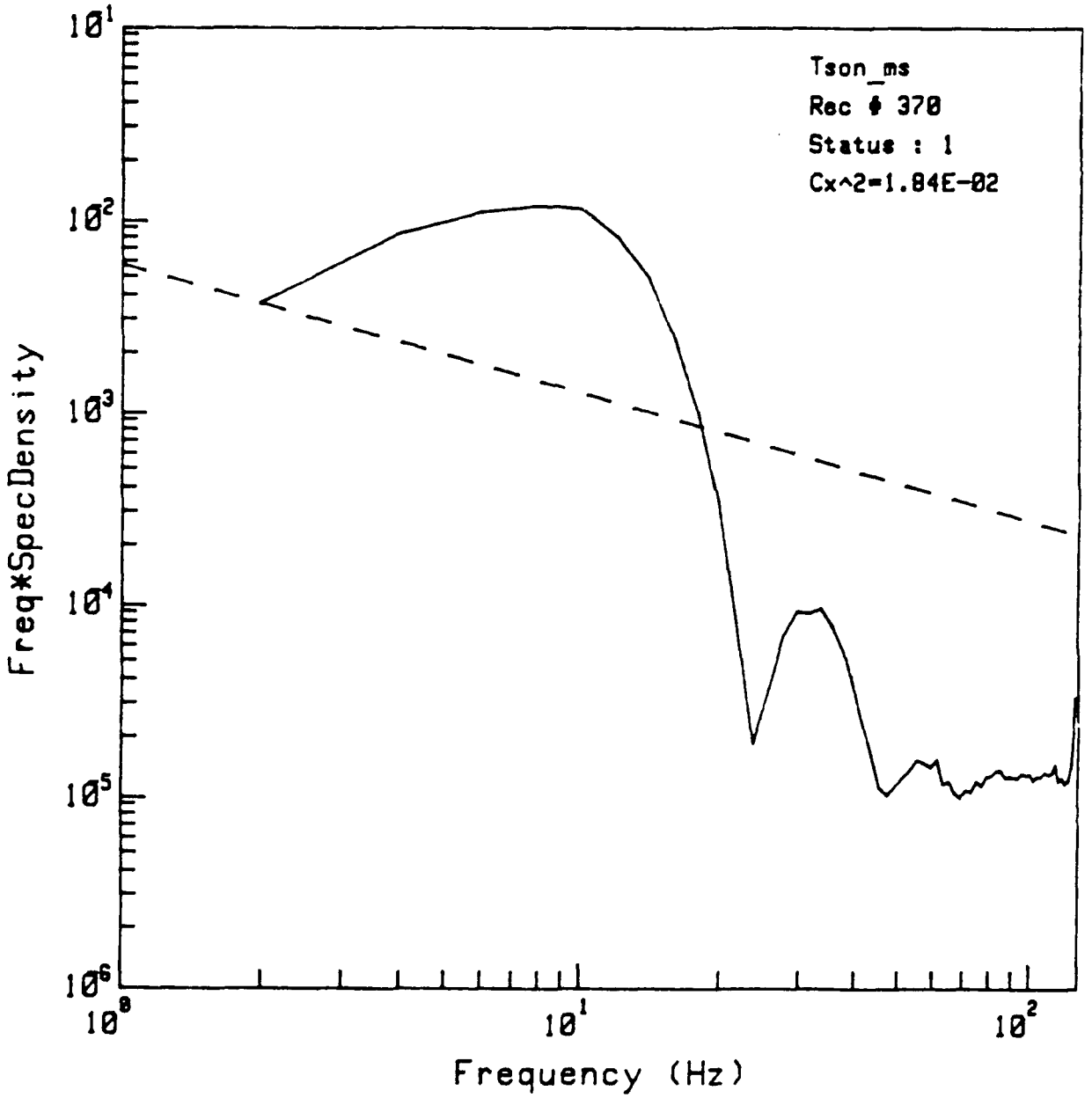
Tson_ms
Rec # 370
Status : 1
Cx^2=1.84E-02
Freq*SpecDensity
Frequency (Hz)
10^1
10^2
10^3
10^4
10^5
10^6
10^0
10^1
10^2

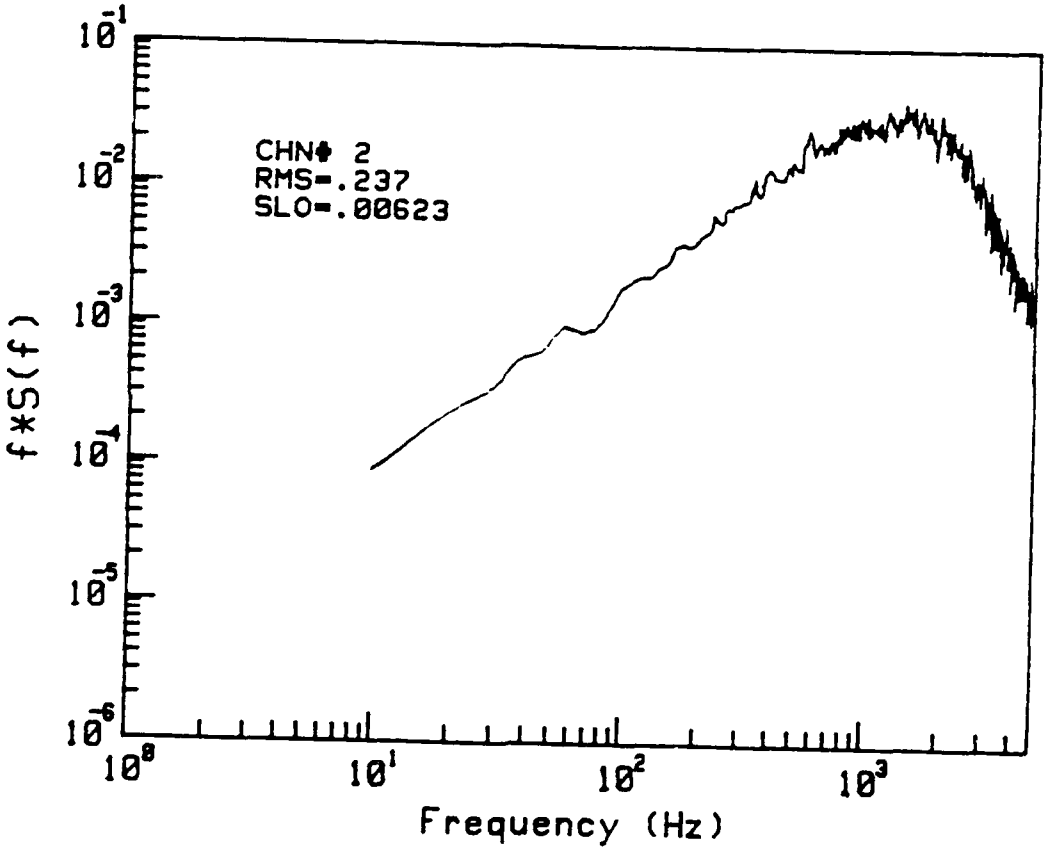
CHN# 2
RMS=.237
SLO=.00623
f*S(f)
Frequency (Hz)

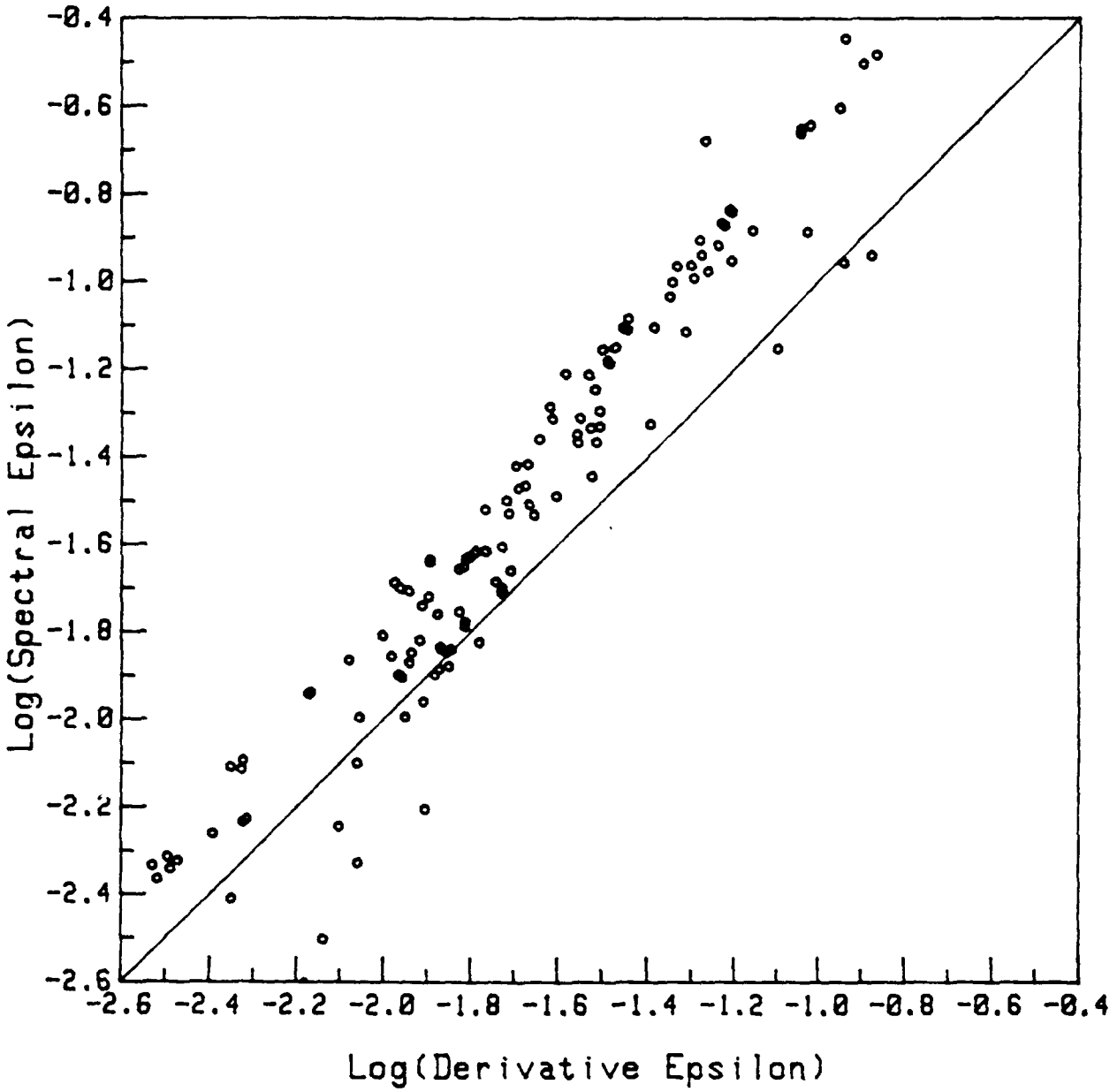
-0.4
-0.6
-0.8
-1.0
-1.2
-1.4
-1.6
-1.8
-2.0
-2.2
-2.4
-2.6
Log(Spectral Epsilon)
-2.6 -2.4 -2.2 -2.0 -1.8 -1.6 -1.4 -1.2 -1.0 -0.8 -0.6 -0.4
Log(Derivative Epsilon)

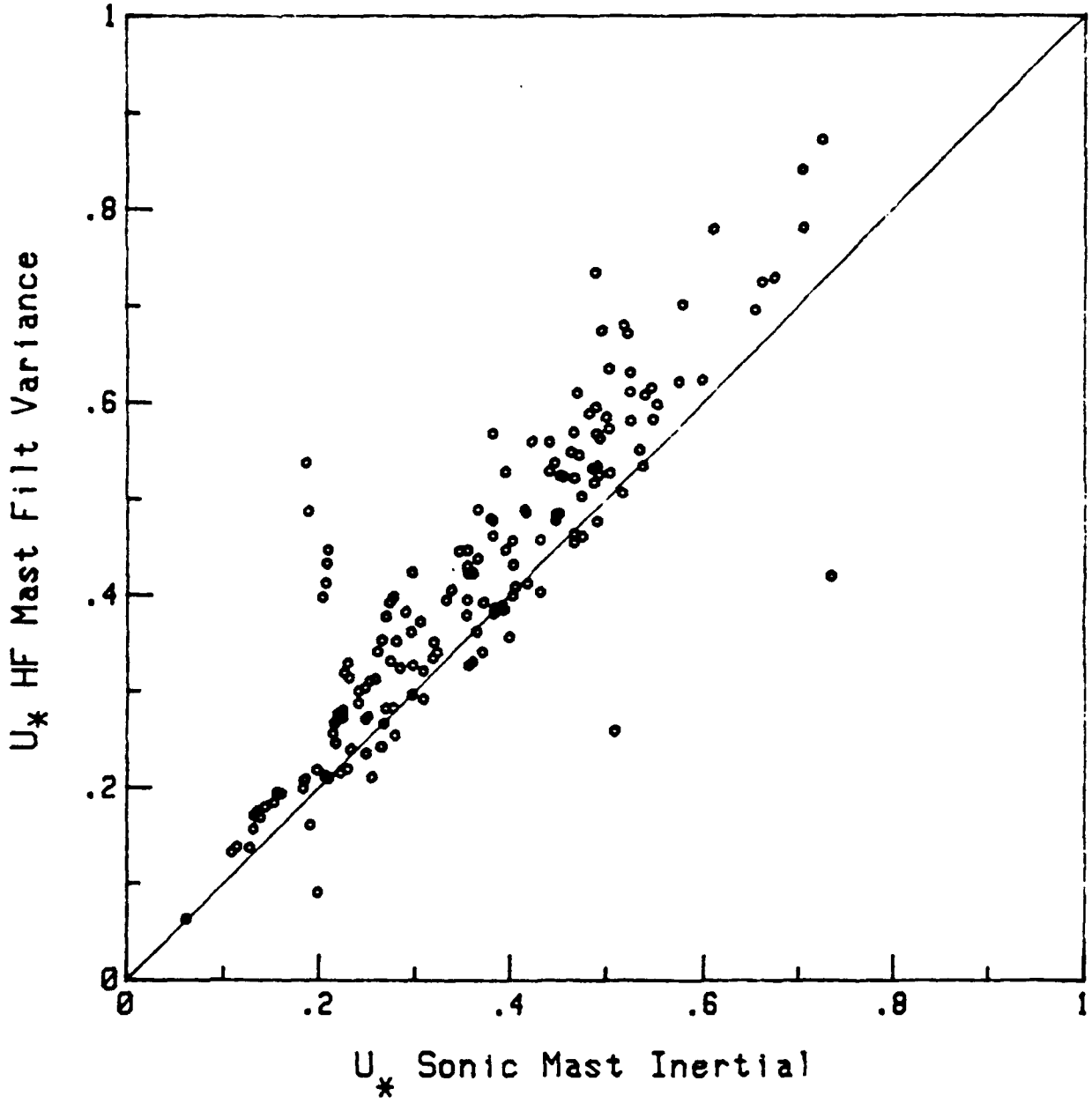
1
.8
.6
.4
.2
0
0
.2
.4
.6
.8
1
U* HF Mast Filt Variance
U* Sonic Mast Inertial

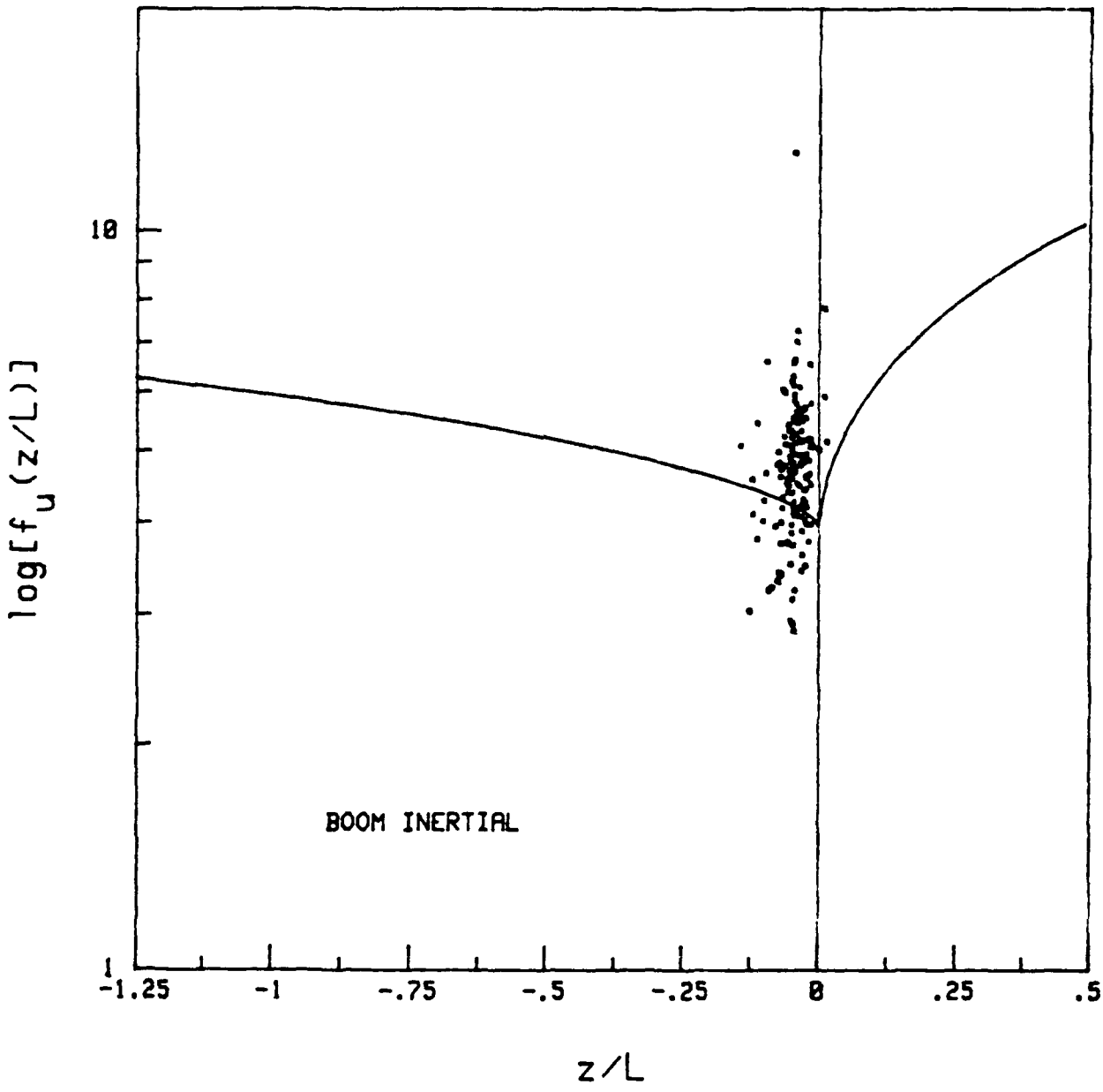
10
1
log[f_u(z/L)]
BOOM INERTIAL
-1.25
-1
-.75
-.5
-.25
0
.25
.5
z/L

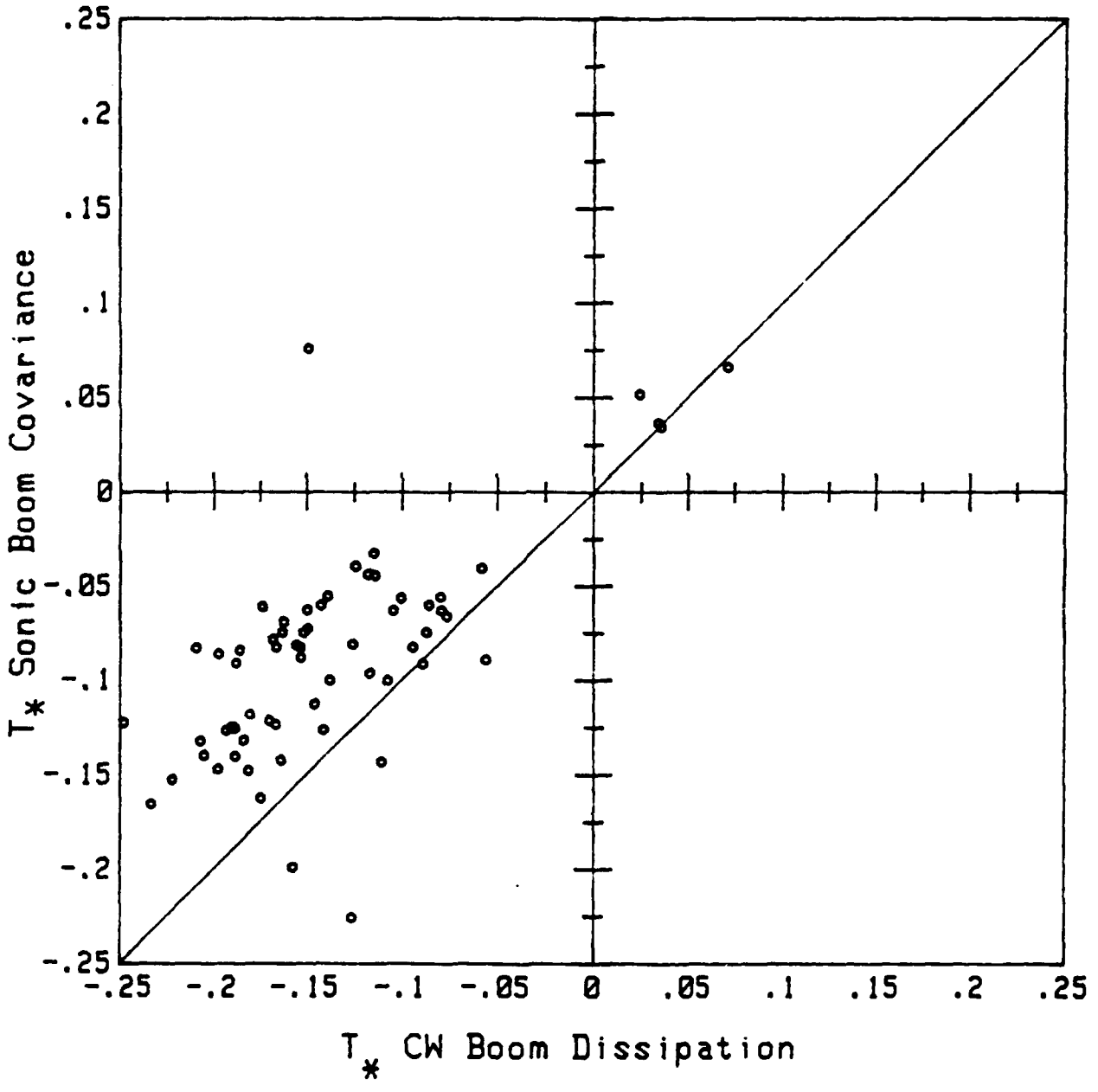
.25
.2
.15
.1
.05
0
-.05
-.1
-.15
-.2
-.25
T* Sonic Boom Covariance
-.25 -.2 -.15 -.1 -.05 0 .05 .1 .15 .2 .25
T* CW Boom Dissipation

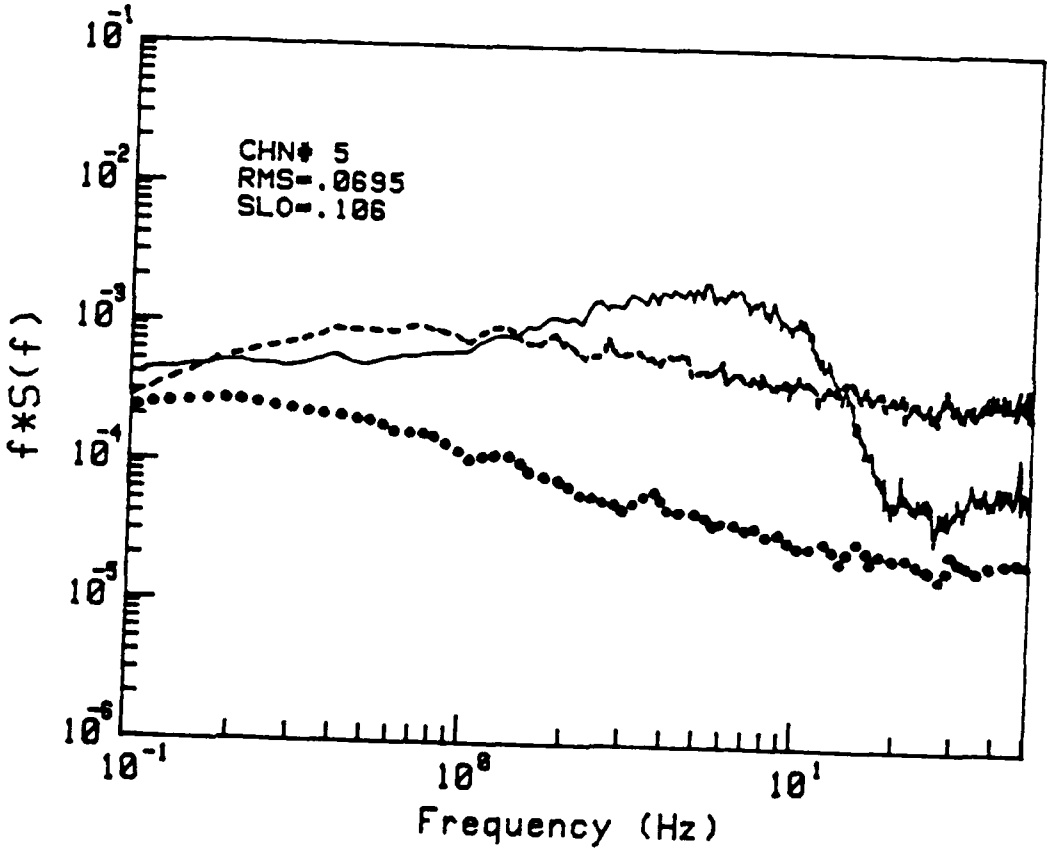
CHN# 5
RMS=.0695
SLO=.106
f*S(f)
Frequency (Hz)

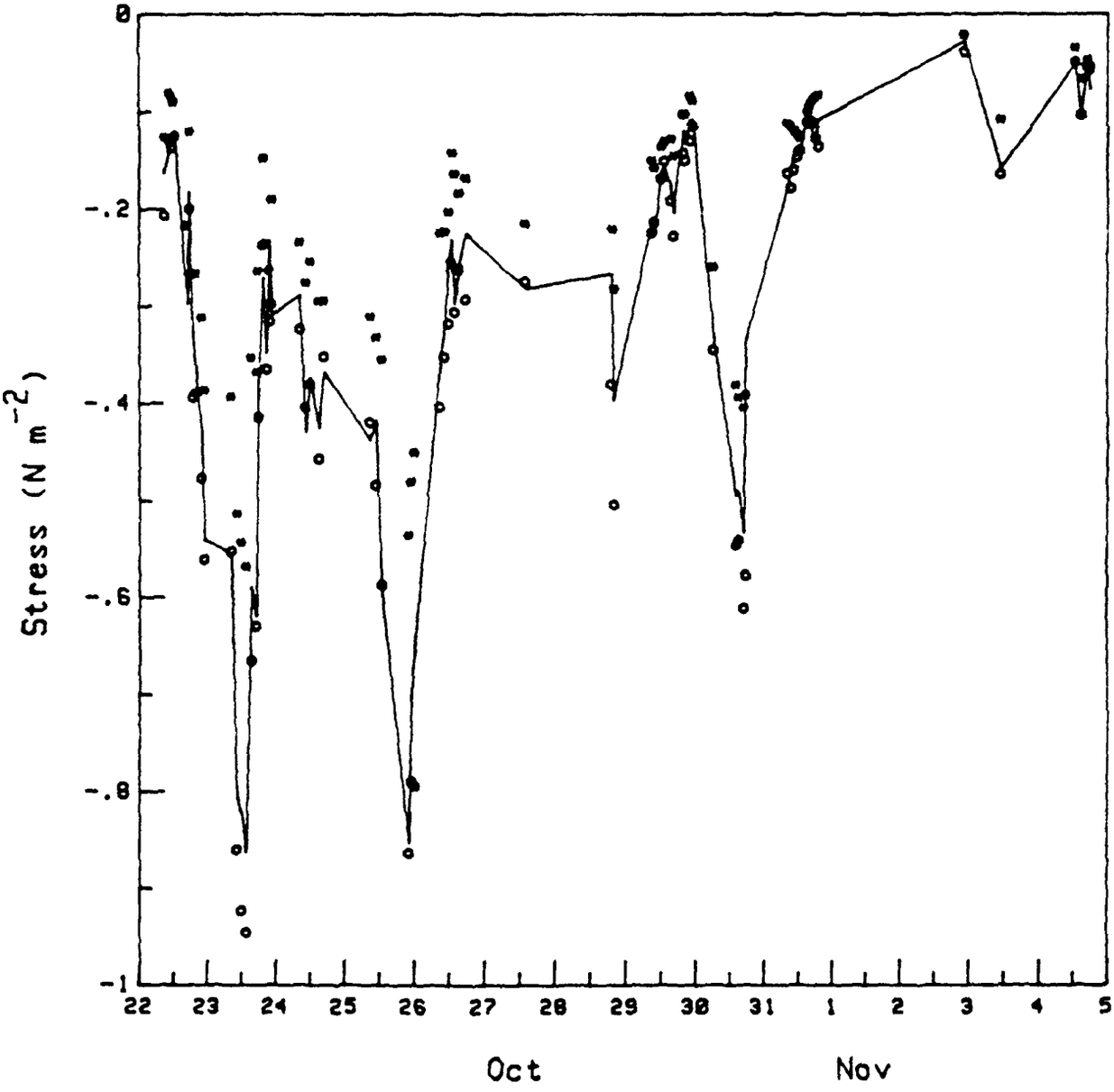

12a

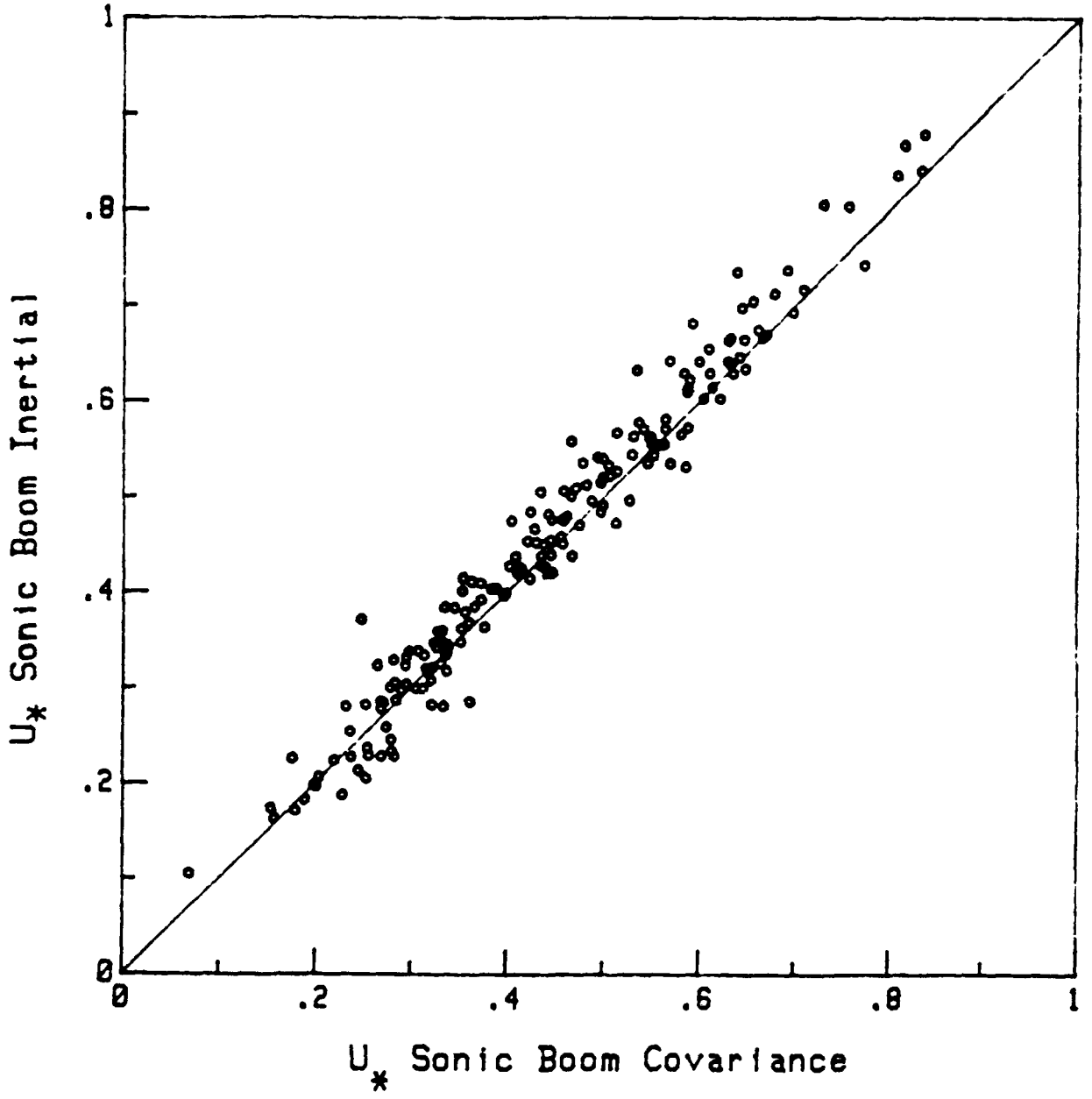
1
.8
.6
.4
.2
0
0
.2
.4
.6
.8
1
U* Sonic Boom Inertial
U* Sonic Boom Covariance

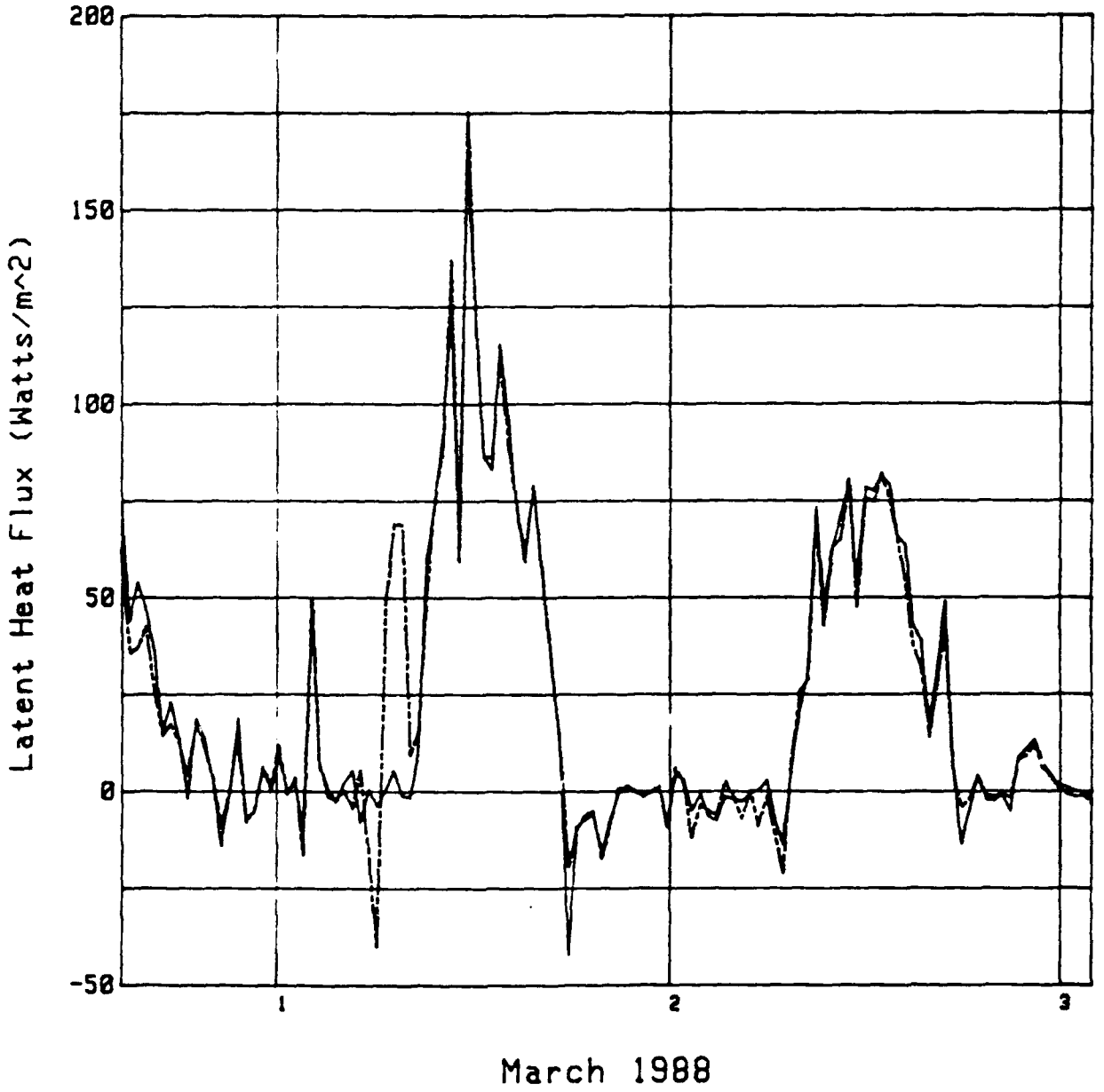
200
150
100
50
0
-50
1
2
3
Latent Heat Flux (Watts/m^2)
March 1988